The energy spectrum of cosmic rays measured with the HEAT extension at the Pierre Auger Observatory

Von der Fakultät für Mathematik, Informatik und Naturwissenschaften der RWTH Aachen University zur Erlangung des akademischen Grades eines Doktors der Naturwissenschaften genehmigte Dissertation

vorgelegt von

Diplomphysiker
Nils Sven Sebastian Scharf

aus Lüdenscheid

Berichter:
Universitätsprofessor Dr. rer. nat. Thomas Hebbeker
Universitätsprofessor Dr. rer. nat. Martin Erdmann

Tag der mündlichen Prüfung: 28.11.2013

Betreuer

Prof. Dr. Thomas Hebbeker
III. Physikalisches Institut A
RWTH Aachen

Contents

1 Introduction **1**

2 Cosmic rays **5**

2.1 The nature of cosmic rays 5

2.2 The origin of cosmic rays 7

2.2.1 Top - down models 7

2.2.2 Bottom - up models 8

2.2.2.1 Acceleration 8

2.2.2.2 Astronomical source candidates 9

2.3 Propagation 9

2.4 Summary 11

3 Extensive Air Showers **13**

3.1 Phenomenology 13

3.1.1 Electromagnetic showers 13

3.1.2 Hadronic showers 15

3.2 Detection techniques 17

3.2.1 Detection of charged secondary particles at ground level . . . 17

3.2.2 Measurement of Cherenkov light 18

3.2.3 Detection of fluorescence light 19

3.2.4 Detection of radio signals 20

3.3 Summary 21

4 The Pierre Auger Observatory **23**

4.1 The Surface Detector 23

4.2 The Fluorescence Detector 24

4.2.1 FD trigger description 28

4.2.2 Energy calibration and energy scale . . . 30
4.2.3 Monitoring . . . 31
4.2.3.1 Detector Monitoring . . . 31
4.2.3.2 Atmospheric Monitoring . . . 32
4.3 Hybrid Detection . . . 33
4.4 Extensions of the Pierre Auger Observatory . . . 33
4.4.1 The High Elevation Auger Telescopes - HEAT . . . 33
4.4.1.1 Comparison between HEAT and standard FD hardware . . . 39
4.4.1.2 HEAT Rate limiting . . . 39
4.4.1.3 Tilt Monitoring for HEAT . . . 41
4.4.2 AMIGA - Auger Muons and Infill for the Ground Array . . . 43
4.4.3 HEATLET . . . 44
4.4.4 Auger Engineering Radio Array - AERA . . . 44
4.4.5 Microwave-detection of extensive air showers . . . 46
4.5 Summary . . . 46

5 Air Shower Reconstruction 47
5.1 SD Reconstruction . . . 47
5.2 FD Reconstruction . . . 48
5.2.1 Shower geometry reconstruction . . . 48
5.2.1.1 FD mono reconstruction . . . 48
5.2.1.2 Hybrid Reconstruction . . . 50
5.2.2 Reconstruction of the longitudinal energy deposit profile . . . 55
5.3 Offline Software Reconstruction Framework . . . 56
5.4 Modifications for HEAT Reconstruction . . . 59
5.4.1 Physical and virtual eyes in the detector description . . . 59
5.4.2 Cross Calibration for HEAT . . . 60
5.4.3 HEAT telescope pointing . . . 60
5.5 Summary . . . 61

6 Air Shower Simulation 63

6.1 The air shower simulation software Conex 63
6.2 Hadronic Interaction Models 64
6.3 Simulation Input 64
6.4 The Offline Simulation Software Framework 66
6.5 Summary 69

7 Data Selection 71

7.1 Description of used cuts 72
7.2 Selection efficiencies: Single and combined 77
7.3 Limits of the air shower simulation 81
7.4 Comparison of measured and simulated data 84
7.5 Results 89

8 Exposure Calculation 93

8.1 The exposure 93
8.2 Aperture Calculation 94
8.2.1 The generation area 94
8.2.2 Calculation of the reconstruction efficiencies 95
8.2.3 The effective area 96
8.2.4 Calculation of the space angle dependence 97
8.2.5 Results of the aperture calculation 99
8.3 Uptime calculation 100
8.4 Calculation of the exposure 103
8.5 Discussion 105

9 Energy spectrum of cosmic rays detected with HEAT 107

9.1 Energy distribution in data 107
9.2 Results 107
9.2.1 Spectral index fit 112
9.2.2 Unfolding of the detector resolution on the calculated spectrum 112
9.2.3 Spectral index fit on unfolded spectrum 114
9.3 Comparison to other published cosmic ray energy spectra 116
9.4 Discussion 117

10 Conclusions **119**

10.1 Summary 119

10.2 Outlook 120

A Appendix **121**

A.1 List of abbreviations 121

A.2 List of conventions 122

A.3 Offline Module sequences 123

A.3.1 Air shower simulation - Offline Module sequence 123

A.3.2 Air shower reconstruction - Offline Module sequence 124

A.4 Shower selection - Cut steering files 125

A.5 Energy bin borders 126

References **136**

Acknowledgements - Danksagung **137**

List of Figures

2.1 All particle energy spectrum of cosmic rays 6

2.2 Cosmic ray energy spectrum 7

2.3 Hillas plot 10

3.1 Simulated longitudinal shower profiles 17

3.2 Fluorescence light spectrum of air 19

4.1 Picture of a Surface Detector station and a Fluorescence Detector building 24

4.2 Map of the southern site of the Pierre Auger observatory 25

4.3 Schematic of an Auger SD station 26

4.4 Picture of a surface detector station 27

4.5 Layout of a standard FD building 27

4.6 MUG-6 Transmission profile 28

4.7 Layout of a standard FD building 29

4.8 Data flow for the FD 30

4.9 Second level trigger patterns 30

4.10 AMIGA infill status 34

4.11 HEAT technical drawing 34

4.12 Geometric FOV bias 35

4.13 Picture of tilted HEAT telescopes 36

4.14 Picture of HEAT and Coihueco 36

4.15 Reduction of Geometric FOV bias 37

4.16 Azimuth angle distribution 38

4.17 Detector - shower distance distribution 39

4.18 Tilt Monitoring Setup 42

4.19 Tilt Monitoring Sensor types 42

4.20 Tilt Monitoring - Example Measurement 43
4.21 The AMIGA detection concept 45
4.22 AERA 45
4.23 Microwave detection of UHECR 46

5.1 Pixel pattern of an FD event 49
5.2 Illustration of the SDP 49
5.3 Shower axis reconstruction - FD mono case 51
5.4 Time - angle correlation. FD mono case. 51
5.5 Shower axis reconstruction - Hybrid case 52
5.6 Pixel pattern for the hybrid case. 53
5.7 Time - angle correlation for the hybrid case. 53
5.8 Advantages of hybrid reconstruction 54
5.9 Measured Light Profile 55
5.10 Energy deposit profile 56
5.11 Pixel pattern - COHE event 59
5.12 Cross calibration of HEAT and Coihueco 61

6.1 Zenith and azimuth angle distributions in Conex 65
6.2 Distances Detector - Shower Core 66
6.3 Distribution of shower cores in the SD array 67

7.1 Energy error distribution 74
7.2 Direct Cherenkov fraction 74
7.3 Core - station distance distribution 75
7.4 Zenith angle distribution 76
7.5 Distance of $X_{\max}$ to field of view borders distribution 76
7.6 Sizes of holes in profile distribution 77
7.7 Reduced χ^2/NDF distribution 78
7.8 Number of events after cuts 79
7.9 Cut efficiencies 79
7.10 Pixel pattern - COHE event 83

7.11 Sizes of holes in profile distribution for simulated data 83
7.12 Comparison of direct Cherenkov fraction 84
7.13 Comparison of zenith angle distributions 85
7.14 Comparison of hole size in reconstructed profiles 86
7.15 Comparison of shower core to station distances 87
7.16 Energy error distributions for the energy bin of $10^{17.5}$ eV 88
7.17 GH $\chi^2/ndof$ distributions for the energy bin of $10^{17.5}$ eV 89
7.18 X_{max} distributions for the energy bin of $10^{17.5}$ eV 90
7.19 Comparison of distance of X_{max} to FOV borders for the energy bin of $10^{17.5}$ eV 91

8.1 Integrated uptime without rate limiting 101
8.2 Integrated uptime with T3 rate limiting 102
8.3 Integrated uptime - ratios 103
8.4 Energy dependence of exposure, Comparison 105
8.5 Energy dependence of exposure, mean value 106

9.1 Energy distribution in data 109
9.2 Cosmic ray flux - Comparison 110
9.3 Cosmic ray flux - Mean 111
9.4 Cosmic ray flux ratios 112
9.5 Energy distribution 114
9.6 Energy resolution 116
9.7 Energy-weighted spectrum of cosmic rays 117

1. Introduction

The discovery of cosmic radiation by Victor Hess in 1912 [1] was the beginning of the field of astroparticle physics. For several decades, until artificial accelerators were developed, the cosmic radiation was the only source for certain types of elementary particles with energies of several GeV. Some particles were first discovered in the cosmic radiation, for example the positron [2], the muon [3] and the pion [4].

The discovery of cosmic ray-induced particle cascades, named extensive air showers (EAS), by detecting coincident particles in spatially separated detectors, was first done by Pierre Auger in 1939 [5]. From his measurements of particle counts with Geiger counters, he concluded, that these air showers were initiated by primary particles with an energy of 10^{16} eV. The technique of using a grid of spatially separated detectors to measure cosmic rays by the detection of extensive air showers is still used today. P. Auger's discovery was the starting point of the era of large ground based detectors in cosmic ray physics. The surface detector technique was used for example at the Volcano Range experiment, where Linsley was able to detect air showers induced by ultra high energy cosmic rays with an energy above 10^{20} eV [6].

Ultra high energy cosmic rays (UHECRs) are cosmic rays with energies up to and over 10^{20} eV. The center of mass energy of the first interaction of an ultra high energy cosmic ray particle with the highest measured energies and a particle of Earth's atmosphere is of the order of 10^{15} eV. That is two orders of magnitude higher than the center of mass energy achievable at the largest man-made particle accelerator, the Large Hadron Collider (LHC), which will accelerate two proton streams to a center of mass energy of 1.4×10^{13} eV when it reaches its design energy[7].

Another technique to study ultra high energy cosmic rays was developed in the 1960's: the detection of fluorescence light generated by air showers. This fluorescence light is produced by nitrogen molecules of the Earth's atmosphere after they were excited by the passage of the secondary particles of an air shower. One of the first large fluorescence observatories was the Fly's Eye/HiRes experiment in the 1980's [8]. Whereas the surface detectors sample the air shower development at the ground level, the fluorescence detection is able to measure the whole longitudinal shower development. The duty cycle for fluorescence detectors is only 15 %, because the fluorescence light is only detectable in clear and moonless nights. The surface detection method has a duty cycle of nearly 100 %.

Several theories predict a change from comic rays with a galactic origin to those with an extragalactic origin to happen somewhere in the energy range of 10^{15} eV to 10^{18} eV (see for example [9],[10],[11],[12],[13] and for an overview [14]). This change

in origin would involve changes in the flux and the composition of cosmic rays. Therefore it is paramount to have a simultaneous measurement of the flux and the composition over the whole energy range and an overlap in energies between different experiments as large as possible.

The Pierre Auger Observatory, the largest cosmic ray observatory to date, is the first cosmic ray observatory to use the hybrid detection method: The simultaneous measurement with surface detectors and fluorescence telescopes. This allows the coincident measurement with both detection methods and a combination of the strengths of both methods. The Pierre Auger Observatory is designed to measure cosmic rays with energies from 10^{18} eV to 10^{20} eV and beyond.

The Pierre Auger Observatory has measured the flux of hadronic cosmic rays, their composition and their arrival directions with high statistics in its design energy range (see for example [15],[16],[17],[18] and [19]). The success of the hybrid detection principle led to the decision to extend the energy rage of the Pierre Auger Observatory. Two extensions to the observatory were planned that lower the energy range of the observatory by one order of magnitude down to 10^{17} eV. The extension for the fluorescence detector system is called High Elevation Auger Telescopes (HEAT) and the one for the surface detector system is called Auger Muons and Infill for the Ground Array (AMIGA). The HEAT extension was completed in 2009 and is taking data since then.

This study focuses on the analysis of cosmic ray events measured with the HEAT extension of the Pierre Auger Observatory (often together with the standard fluorescence detector). It presents an analysis of the absolute flux of cosmic rays in an energy range new to the Pierre Auger Observatory. The goal of this work is the measurement of the energy spectrum, that is the absolute flux of cosmic rays as a function of their energy. The main part of this analysis is the calculation of the exposure of the detector. The exposure describes the observation capabilities of a detector and is a combination of the uptime, the field of view and the effective area of a detector. The exposure is calculated by analyzing the uptime from the monitoring data of the detector and the effective area and field of view of the detector with simulated air showers. To do so, it is essential to produce a large shower database, which is another important part of this work. This analysis uses a static detector description for the simulation, because information that is needed for a time dependent simulation normally used for the exposure calculation was not available, for example the absolute drum calibration of HEAT and other parameters that depend on the calibration.

This work is structured as follows: Chapter 2 gives an overview over cosmic ray physics in general, whereas chapter 3 describes the phenomenon of extensive air showers. Chapter 4 details the Pierre Auger Observatory, the largest observatory for the study of cosmic rays. The reconstruction of air shower parameters used for the data taken at the Pierre Auger Observatory is explained in chapter 5. The production of a large database of simulated air showers is presented in chapter 6. The dataset used for the analysis is presented in chapter 7. The core of this work, the calculation of the exposure of the detector and the energy spectrum of cosmic rays

in the HEAT energy range is presented in the chapters 8 and 9. Chapter 10 gives a summary of the work and an outlook. A list of abbreviations and used conventions together with additional tables is found in the appendix A.

2. Cosmic rays

Since the discovery of cosmic rays at the beginning of the last century, several open questions concerning their nature remain: The origin (or the sources of cosmic rays) is unknown and their propagation from their origin to us is still not completely understood. With either direct measurements by satellites or indirect measurements at ground, the energy of cosmic ray particles, their particle type (the composition) and their arrival direction can by measured. With this information it is possible to give some answers to the open questions of cosmic rays. This chapter provides a general overview of the properties of cosmic rays and describes common theories concerning the origin and the propagation of cosmic rays. The chapter is based mainly on a recent review of high-energy cosmic rays from Blümer, Engel and Hörandel [14] and to a lesser extent on a review on cosmic rays by Nagano and Watson[20].

2.1 The nature of cosmic rays

The earth is constantly hit by ionized atomic nuclei from outside the solar system. These nuclei are called cosmic rays. The measured kinetic energy range of cosmic rays spans from several MeV to 10^{20} eV. The flux of cosmic rays is rapidly decreasing with energy, from 1000 particles per second and square meter at GeV energies, to one particle per square meter and year at PeV energies to less than one particle per year and square kilometer at energies above 100 EeV. The differential energy spectrum of cosmic rays, that is the flux in dependence of energy, is shown in figure 2.1.

This rapidly decreasing flux leads to an experimental challenge: Only for the lower energies, the direct measurement of cosmic rays with satellite experiments or balloon - borne experiments is possible. For cosmic rays with higher energies, the sensitive areas of satellite or balloon experiments become too small to achieve a high number of measured cosmic rays in the typical lifetime of balloon or satellite experiments. For cosmic ray energies exceeding 100 TeV the required detection areas become so large, that they are realized as ground level detectors. This leads to another experimental challenge: For ground level detectors, the direct measurement of cosmic rays is not possible, because the cosmic rays which enter the Earth's atmosphere interact with air molecules and produce extensive air showers (EAS), that are cascades of secondary particles (see chapter 3). Only these secondary particles can be measured with ground based detectors and these measurements are then used to gain information on the primary cosmic ray that started the air shower. The energy ranges

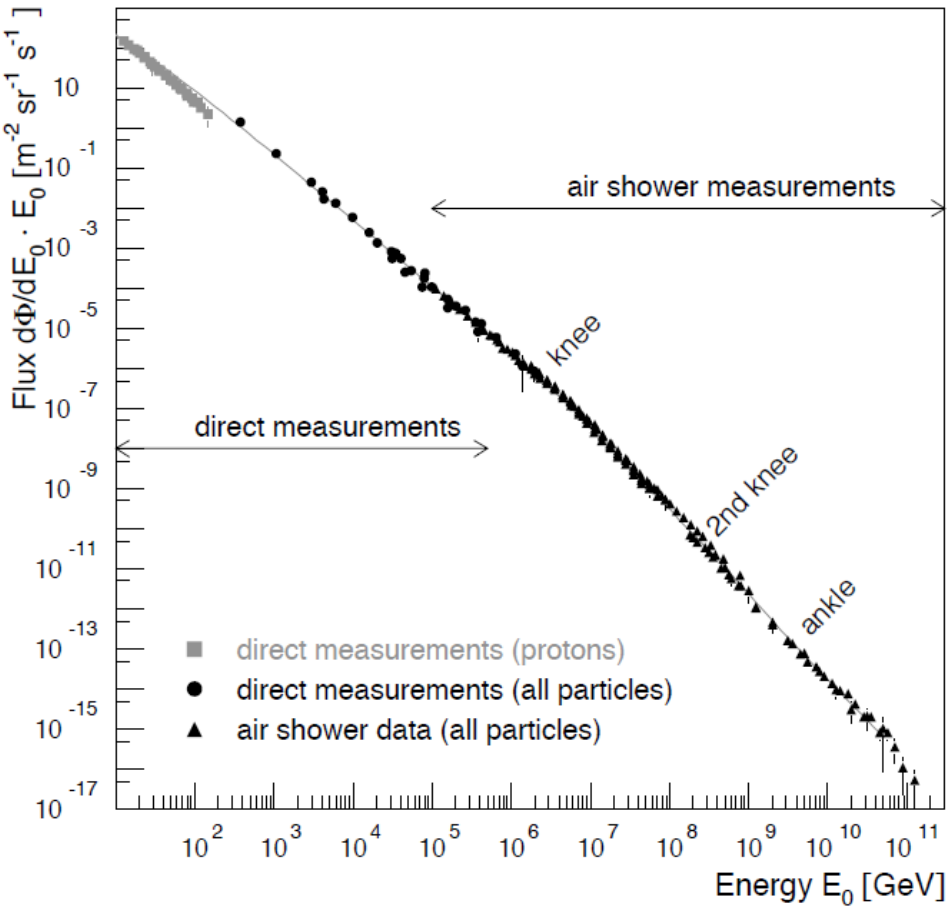

Figure 2.1: All particle energy spectrum of cosmic rays measured directly with detectors above the atmosphere and with air shower detectors. At low energies, the flux of primary protons is shown. From [14].

of direct and indirect measurements of cosmic rays are given by the arrows in figure 2.1.

Over the wide energy range shown in figure 2.1, the energy spectrum follows a power law $\mathrm{d}N/\mathrm{d}E \propto E^{\gamma}$. This is typical for non thermal acceleration processes. Features in the energy spectrum become only visible, when the flux is multiplied with a larger power of the particle energy. In this representation, see figure 2.2, even small changes in the spectral index γ become visible.

Such visible changes in the spectral index are: A steepening of the spectral index from $\gamma \approx -2.7$ at energies of several PeV to $\gamma \approx -3.1$ at higher energies. This feature is called the knee. The second knee, a further steepening of the spectrum, occurs at around $4 \times 10^{17}\,\mathrm{eV}$. At an energy of around $4 \times 10^{18}\,\mathrm{eV}$ the spectrum flattens again. The position of this features is also marked in figure 2.1.[1]

[1]The names of the features in the energy spectrum come from the picture of a stretched leg that is viewed from the side, starting at upper thigh with the lowest energies and going to the toes at the highest energies.

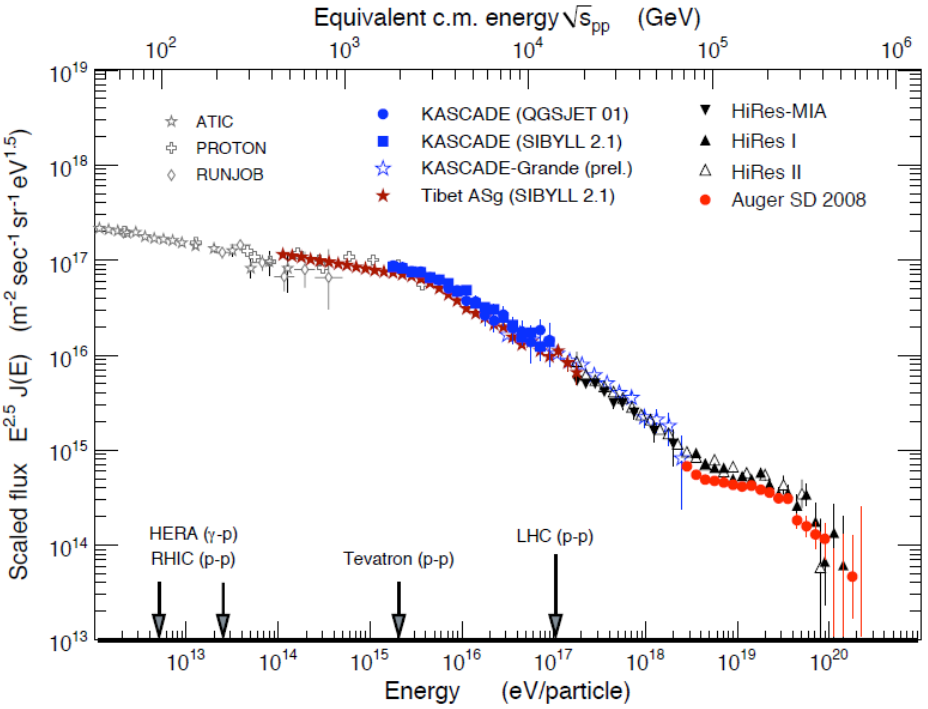

Figure 2.2: Cosmic ray energy spectrum. To make features in the spectrum visible, the flux was multiplied with the energy to the power of 2.5. Shown are direct measurements from ATIC [21], PROTON [22] and RUNJOB [23] and measurements from air shower experiments, such as ASγ [24], KASKADE [25], KASKADE-Grande [26] and Akeno [27] [28] measurements. The highest energy measurements are from HiRes-MIA [29] [30], HiRes I and II [31] and the Pierre Auger Observatory [32]. In addition, the center of mass energy of several particle accelerators is given for comparison. Figure from [14].

2.2 The origin of cosmic rays

There exist two general classes of theories that try to explain the origin of cosmic rays. The first class are the so called "top - down" theories and the second are the so called "bottom - up" theories. In top - down theories, the origin of cosmic rays is explained as a result of the decay of very heavy precursor particles or the interaction of these particles. Top - down theories need new physics or at least new types of particles. Bottom - up theories explain the origin of cosmic rays with the acceleration of low energetic particles to higher energies with processes described by the standard model of particle physics[33] at astrophysical sources. Both models lead to differences in the flux, composition and arrival direction distribution, so that they can be distinguished experimentally.

2.2.1 Top - down models

The so called top - down models for the origin of cosmic rays are non accelerating models. In this models the cosmic rays are produced by the decay of super-heavy

objects. Possible candidates discussed are super-heavy dark matter[34], cryptons[35] or topological defects[36]. All these models need new physics and predict high fluxes of gamma-rays at ultra high energies. Today, nearly all top - down models for the origin of cosmic rays are disfavored by cosmic ray measurements, see for example [37],[38] and [39].

2.2.2 Bottom - up models

The momentarily favored models for the origin of cosmic rays are so called bottom - up models. In them, the cosmic rays are accelerated at astronomical source objects from lower energies to higher energies. Enrico Fermi [40] proposed a process for particle acceleration that involved the interaction of particles with large-scale magnetic fields in the Galaxy. A modification of this process leads to the currently accepted model of cosmic ray acceleration: The first-order Fermi acceleration, that operates in strong shock fronts of supernovae and shock fronts that propagate from supernova remnants (SNR) into the interstellar medium[41].

2.2.2.1 Acceleration

Diffuse first-order Fermi acceleration is the accepted acceleration process for cosmic rays at the moment. Charged particles gain an amount of energy that is proportional to the energy they currently have per acceleration cycle. One cycle is the passage of the particle from the unshocked part of the medium to the shocked region of the medium and back. This makes Fermi acceleration a very attractive process for cosmic ray acceleration. In every cycle there is a probability for the particle to leave the acceleration region. These particles then begin their travel as cosmic ray with the energy they gained in the acceleration region. Particles that stay longer in these regions are those with higher energies. For a particle with charge Z, that stays in the acceleration region with a magnetic field B for the time T, the maximum achieved energy is $E_{max} \sim Z \cdot e \cdot \beta_s \cdot B \cdot T \cdot V_s$, with $\beta_s = V_s/c$ the velocity of the shock front. For typical values, achieved in type II supernovae, this leads to a maximum achievable energy of $E_{max} \sim Z \cdot 10^{14}\,\mathrm{eV}$ [42]. For some special type of supernovae the maximum energy can be of one order of magnitude larger [43]. A process where the accelerated cosmic rays interact with the magnetic field of the accelerating region, which would lead to an amplification of the fields and so to an even higher maximum energy, was proposed [44]. With this mechanism the acceleration of charged particles to energies of $10^{17}\,\mathrm{eV}$ is possible.

Some features in the cosmic ray spectrum can also be explained as features in the acceleration process. One theory for the existence of the knee in the spectrum is that it represents the upper limit of particle acceleration by galactic sources. For energies higher than the knee, a transition from galactic to extragalactic cosmic rays happens. The ankle is then explained as the energy where extragalactic cosmic rays with a steeper spectrum become the dominant contribution. These extragalactic cosmic rays then dominate the spectrum at the highest energies. The other theory explains the features with a phenomenon that is called galactic leakage. Galactic leakage means that for higher energies the cosmic rays are not contained inside the Galaxy

any more. This can be explained by the Larmor radius (the radius of oscillation of a charged particle inside a magnetic field) becoming larger than the size of the galactic disk or the size of the galactic halo. The Larmor radius is given as

$$r_L = 1.08\,\mathrm{pc}\,\frac{E/\mathrm{PeV}}{Z \cdot B/\mu\mathrm{G}} \tag{2.1}$$

If the knee is caused by either of these processes, the cut-off energy for different elements with charge Z would be $E_c^Z = Z \cdot E_c^p$. E_c^p is the cut-off energy for protons. The sum of the flux of all elements with their different cut-off energies would then make up the all-particle spectrum. The knee would then be related to the cut-off for protons and the steeper flux above the knee is a result of the overlap of the cut-offs for the different elements.

2.2.2.2 Astronomical source candidates

Constraints on the travel distance of cosmic rays with energies above $10^{20}\,\mathrm{eV}$ limit the distance to the sources to a maximum of 100 Mpc. Although possible galactic source candidate classes for these high energies exist, they are scarce and distributed anisotropically. They are disfavored by the apparent isotropic arrival direction distribution for the highest energy cosmic rays, because the deflection angle for the highest energies is expected to be of the order of only 5°. Cosmic rays with energies over $10^{18}\,\mathrm{eV}$ are not contained in the Galaxy any more, so their sources are expected to be extragalactic. Shock fronts in magnetized media exist not only for SNR but also for other astrophysical objects, often of the size of galaxies. For diffusive shock acceleration inside a source with the size R and a magnetic field B, the maximum acceleration energy can be given by [45]:

$$E_{\max} \simeq 10^{18}\,\mathrm{eV}\; Z\; \beta_s\; \left(\frac{R}{\mathrm{kpc}}\right)\left(\frac{B}{\mu\mathrm{G}}\right), \tag{2.2}$$

where β_s is the shock velocity in units of the speed of light and Z is the particle charge. A Hillas plot[45] displaying this relation for various astrophysical objects is shown in figure 2.3. Only very few candidate sources exist, for example: active galactic nuclei (AGN)[46],[47],[48], radio lobes of FR II galaxies[49],[50] and gamma-ray bursts (GRBs)[51]. A review of possible sources can be found in [52].

2.3 Propagation

For galactic cosmic rays, it is assumed that they propagate in a diffusive process through the Galaxy and are deflected many times at the randomly orientated magnetic fields inside the Galaxy, that have a mean strength of $B \sim 3\,\mu\mathrm{G}$. Galactic cosmic rays have a Larmor radius of the size of the galactic halo. The repeated deflections of the cosmic rays lead to a total loss of source direction information, so that cosmic rays up to the highest energies have an isotropic arrival direction distribution. The time the cosmic rays are staying in the Galaxy is found to be

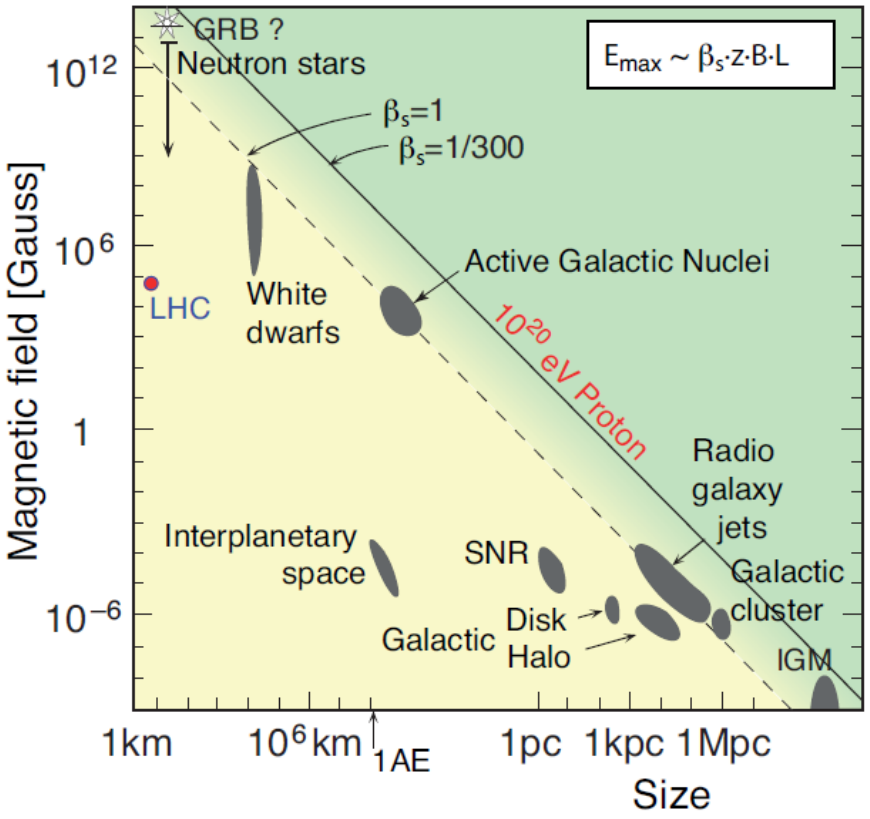

Figure 2.3: Hillas plot [45] of astrophysical sources that would be able to accelerate protons to an energy of 10^{20} eV. Shown is the magnetic field strength of astrophysical objects versus their size. The two diagonal lines represent the possibility of an object to accelerate a proton to energies of 10^{20} eV, for shock front velocities of $\beta_s = c$ for the left line and $\beta_s = c/300$ for the right line. From [14].

about 15×10^6 years for cosmic rays with GeV energies[53]. In addition, spallation processes are possible. These processes change the type of the cosmic ray particle. A cut-off in the spectrum of cosmic rays is expected for energies above 6×10^{19} eV. This so called Greisen - Zatsepin - Kuzmin (GZK)[54],[55] cut-off originates from the interaction of cosmic ray protons with the photons of the cosmic microwave background (CMB). All hadronic particles with energies over 6×10^{19} eV lose their energy relatively fast when propagating, until they have an energy below the GZK energy. For protons the interaction process with the CMB is mainly the formation of a $\Delta^+(1232)$ resonance[56]:

$$\gamma + p \rightarrow \Delta^+ \rightarrow p + \pi^0$$

and

$$\gamma + p \rightarrow \Delta^+ \rightarrow n + \pi^+$$

The proton loses about 20% of its energy in this reaction, but if the resulting proton has an energy that is over the GZK energy, this process can happen again.

The possibly produced neutron decays again into a proton. Heavier cosmic ray nuclei lose their energy through photo disintegration when interacting with the CMB photons[57].

For the highest energy cosmic rays with energies above $10^{19.5}$ eV the angular deflection in our Galaxy is expected to be only a few degrees[58]. Together with large voids with very low magnetic fields between galaxies[59] this would lead to small total angular deflections and the cosmic rays would approximately point back to their sources. With a high number of detected events with these energies, cosmic ray astronomy would become possible, which would allow measurements of correlations between arrival directions and sources or source regions.

2.4 Summary

The simultaneous measurement of the energy, the particle type and the arrival direction of cosmic rays with high statistics and small systematic uncertainties over a large energy range will help to answer questions concerning the origin of cosmic rays and their propagation through the universe. For the highest energy cosmic rays this is done by ground based air shower detectors, which measure extensive air showers (EAS) which were instigated by cosmic rays hitting the Earth's atmosphere. The phenomenon of EAS and possible detection techniques are described in the next chapter.

3. Extensive Air Showers

When a cosmic ray particle enters the Earth's atmosphere and interacts with a molecule of the atmosphere (or rather a nucleus in the molecule) it generates a cascade of secondary particles. This cascade is called an extensive air shower (EAS). In this chapter the phenomenology of extensive air showers and the detection techniques used to measure air showers are presented. The description of air showers and the detection methods follows again the recent review of high-energy cosmic rays from Blümer, Engel and Hörandel[14]. A detailed description of this topic can be found in [60].

3.1 Phenomenology

The phenomenon of air showers can be described by two general classes of air showers: Electromagnetic showers that are produced by photons or electrons and positrons entering the atmosphere and hadronic showers, which are produced by hadronic particles entering the atmosphere. The processes in an air shower are described by cross-sections which depend on the amount of traversed matter. A new size for the description of these processes is the slant depth, or atmospheric depth X. It is defined as a path integral

$$X(s) = \int_s \rho(x)\mathrm{d}x \tag{3.1}$$

along the track s over the atmospheric density ρ at point x. The unit of the slant depth is $g\ cm^{-2}$. The slant depth is $0\,\mathrm{g\ cm^{-2}}$ at the top of the atmosphere and approximately $1000\,\mathrm{g\ cm^{-2}}$ at ground level for a vertical track.

3.1.1 Electromagnetic showers

If an air shower is instigated from a photon or an electron or a positron, the shower is called an electromagnetic shower. For electromagnetic showers the so called Heitler model[61] exists, which, although an oversimplification, can describe basic shower properties. The two main processes for electromagnetic showers are the bremsstrahlung of electrons[1] and the pair production of electrons by photons. For the total energy loss $\mathrm{d}E/\mathrm{d}X$ of electrons one gets:

$$\frac{\mathrm{d}E}{\mathrm{d}X} = -\alpha(E) - \frac{E}{X_\mathrm{R}} \tag{3.2}$$

[1] Until otherwise noted, the term "electrons" is used to describe electrons and positrons together in the following.

with X the slant depth, $\alpha(E)$ the ionization energy loss given in the Bethe-Bloch formula and the radiation length X_R which depends on the material in which the shower is developing. For air it is $X_\mathrm{R} \approx 37\,\mathrm{g/cm^2}$. The two processes of particle multiplication and ionization energy loss are competing in the shower. The critical energy E_c is the energy, when an electron loses the same energy due to ionization and particle production. It is $E_\mathrm{c} = X_\mathrm{R}\,\langle\alpha(E_\mathrm{c})\rangle \approx 86\,\mathrm{MeV}$.

In the Heitler model, the incoming cosmic ray interacts after a depth distance λ_em. Two new particles with half the initial energy are produced. Each of these particles interacts again after traveling the distance λ_em and so forth. After n successive interactions the number of particles is 2^n. The number of particles as a function of depth X is then $N(X) = 2^{X/\lambda_\mathrm{em}}$. New particles are produced until the energy of the secondary particles is smaller than the critical energy E_c, when absorption processes become dominant over particle production.

The maximum number of particles in the shower is then given by $N_\mathrm{max} = E_0/E_\mathrm{c}$ and the depth of the shower maximum is $X_\mathrm{max} = \lambda_\mathrm{em}\log_2(E_0/E_\mathrm{c})$. E_0 is the energy of the primary particle. The slant depth where the total number of particles in the shower reaches its maximum is called the shower maximum X_max. After this point, the number of particles in the shower declines again because of absorption processes. The shower maximum can be given for different types of particles in the shower, for example electrons or muons, separately.

Important features of electromagnetic showers, that can be learned from the Heitler model are, that the number of particles at the shower maximum is proportional to the primary energy and the depth of the shower maximum depends logarithmically on the primary energy.

More advanced calculations using cascade theory give further answers[62][63]. The depth of the shower maximum for shower particles of energy E is given by $X_\mathrm{max} \approx X_\mathrm{R}\ln(E_0/E)$. When the energy distribution of the particles in the shower is considered, one gets, for example, the shower maximum for electrons in a photon induced shower as

$$X_\mathrm{max} \approx X_\mathrm{R}\left[\ln\left(\frac{E_0}{E_\mathrm{c}}\right) + \frac{1}{2}\right]. \tag{3.3}$$

For energies above E_c the energy spectrum of secondary particles can be described by a power law $\mathrm{d}N/\mathrm{d}E \sim E^{-(1+s)}$ with the shower age parameter s which can be given as $s \approx 3X/(X + 2X_\mathrm{max})$. A function often used to fit longitudinal shower profiles is the Gaisser-Hillas function[64]:

$$N(X) = N_\mathrm{max}\left(\frac{X - X_0}{X_\mathrm{max} - X_0}\right)^{(X_\mathrm{max}-X)/\Lambda} \exp\left(\frac{X_\mathrm{max} - X}{\Lambda}\right) \tag{3.4}$$

with the mean free path length Λ (around $70\,\mathrm{g\,cm^{-2}}$ for protons in air) and the shape parameter X_0 which is only very weakly dependent on the depth of the first interaction.

The lateral particle distribution is mainly determined by multiple Coulomb scattering of electrons. It can be described by the Nishimura-Kamata-Greisen function (NKG)[65]

$$\frac{\mathrm{d}N_\mathrm{e}}{r\ \mathrm{d}r\ \mathrm{d}\phi} = C(s)N_\mathrm{e}(X)\left(\frac{r}{r_1}\right)^{s-2}\left(1+\frac{r}{r_1}\right)^{s-4.5} \tag{3.5}$$

with r the distance to the center of the cascade (the shower axis) and ϕ the azimuth angle around the axis.
The normalization constant is $C(s) = \Gamma(4.5-s)/[2\pi r_1^2\Gamma(s)\Gamma(4.5-2s)]$, the Molière unit is $r_1 \approx 9.3\,\mathrm{g\ cm^{-2}}$ and $N_\mathrm{e}(X)$ is the number of electrons at slant depth X.

3.1.2 Hadronic showers

The main difference between electromagnetic and hadron-initiated showers stem from the fact that hadronic showers produce a significant higher muon number compared to very few muons for electromagnetic showers. In addition, multi-particle production in hadronic interactions lead to large event-to-event fluctuations. A similar model to the Heitler model can be developed for hadronic showers[66],[67],[68],[69].

In it, a hadronic interaction of a particle with energy E produces n_tot new particles with energy E/n_tot. Of these new particles, two thirds are charged particles n_c (charged pions) and one third are neutral particles n_n (neutral pions). The neutral pions decay immediately into electromagnetic particles $\pi^0 \to 2\gamma$. The charged pions re-interact with air nuclei if their energy is greater than some typical decay energy E_dec or decay otherwise. The decay energy is a model parameter. The number of generations of hadronic interactions n follows from $E_\mathrm{dec} = E_0/(n_\mathrm{tot})^n$.

Under the assumption that one muon is produced in the decay of each charged particle, this leads to the number of muons as

$$N_\mu = (n_\mathrm{c})^n = \left(\frac{E_0}{E_\mathrm{dec}}\right)^\alpha \tag{3.6}$$

with $\alpha = \ln n_\mathrm{ch}/\ln n_\mathrm{tot} \approx 0.86\cdots0.93$. The value of α follows directly from the charged particle multiplicity of the Heitler model: In each interaction, the number of charged particles is 2/3 of the total number of particles produced in the interaction. With $n_\mathrm{ch} = \frac{2}{3}\ n_\mathrm{tot}$ the value of $\alpha \approx 0.86\cdots0.93$ follows. The values of α and E_dec depend on the muon energy threshold. The number of muons produced in an air shower increases almost linearly with primary energy and depends on the air density and the particle multiplicities of hadronic interactions.

The simple model allows to estimate the energy that is transferred into the electromagnetic shower component. After n generations the energy in the hadronic component is given by

$$E_\mathrm{had} = \left(\frac{2}{3}\right)^n E_0 \tag{3.7}$$

and the energy in the electromagnetic component by

$$E_\mathrm{em} = E_0 - E_\mathrm{had} \tag{3.8}$$

The number of generations of charged pions is typically five to six (known from simulations[70]) and increases slightly with energy. Because of this, the fraction of the shower energy that is transferred into the electromagnetic component is increasing from 70 - 80% at 10^{15} eV to 90 - 95% at 10^{20} eV.

The depth of shower maximum of a hadron induced shower is given by the shower maximum of the electromagnetic component $X^e_{\max}$. The first hadronic interaction produces electromagnetic particles with total energy $\sim E_0/n_{\mathrm{tot}}$. This leads to the lowest order approximation

$$\begin{aligned} X_{\max}(E_0) &\sim \lambda_{\mathrm{had}} + X^{\mathrm{e}}_{\max}(E_0/n_{\mathrm{tot}}) \\ &\sim \lambda_{\mathrm{had}} + X_{\mathrm{R}} \cdot \ln\left(\frac{E_0}{n_{\mathrm{tot}} E_{\mathrm{c}}}\right). \end{aligned} \tag{3.9}$$

λ_{had} is the hadronic interaction length.

A nucleus as primary shower particle can be described as a superposition of a number of protons[71]. A nucleus with a mass A and an energy E_0 is considered as A independent nucleons with energy $E_{\mathrm{h}} = E_0/A$. The superposition of the individual nucleon showers leads to

$$N^A_{\max} \approx A \cdot \frac{E_{\mathrm{h}}}{E_{\mathrm{c}}} = \frac{E_0}{E_{\mathrm{c}}} = N_{\max} \tag{3.10}$$

$$X^A_{\max} \approx X_{\max}(E_0/A) \tag{3.11}$$

$$N^A_{\mu} \approx A \cdot \left(\frac{E_0/A}{E_{\mathrm{dec}}}\right)^{\alpha} = A^{1-\alpha} \cdot N_{\mu} \tag{3.12}$$

In good approximation, the number of charged particles at shower maximum is independent of the primary hadron whereas the number of muons and the depth of the shower maximum do depend on the mass of the primary particle. For a given energy, the number of muons is increasing with heavier primary nuclei.

Because of the superposition of several hadronic showers, the shower-to-shower fluctuations for nuclei are smaller than those for proton induced showers. Shower-to-shower fluctuations are the fluctuations between several air shower cascades from identical primary cosmic ray particles under identical conditions. These fluctuations are produced by the stochastic nature of the particle processes in the air shower cascade.

The basic shower properties are confirmed by detailed Monte Carlo Simulations of air showers. The longitudinal profiles of two single air showers, the first with a proton primary, the second with an iron primary, simulated with CORSIKA [72] with an energy of 10^{19} eV are shown in figure 3.1. One can see, that in the region of the shower maximum less than 1 % of the charged particles are muons and that the electromagnetic component is absorbed much faster than the muonic component.

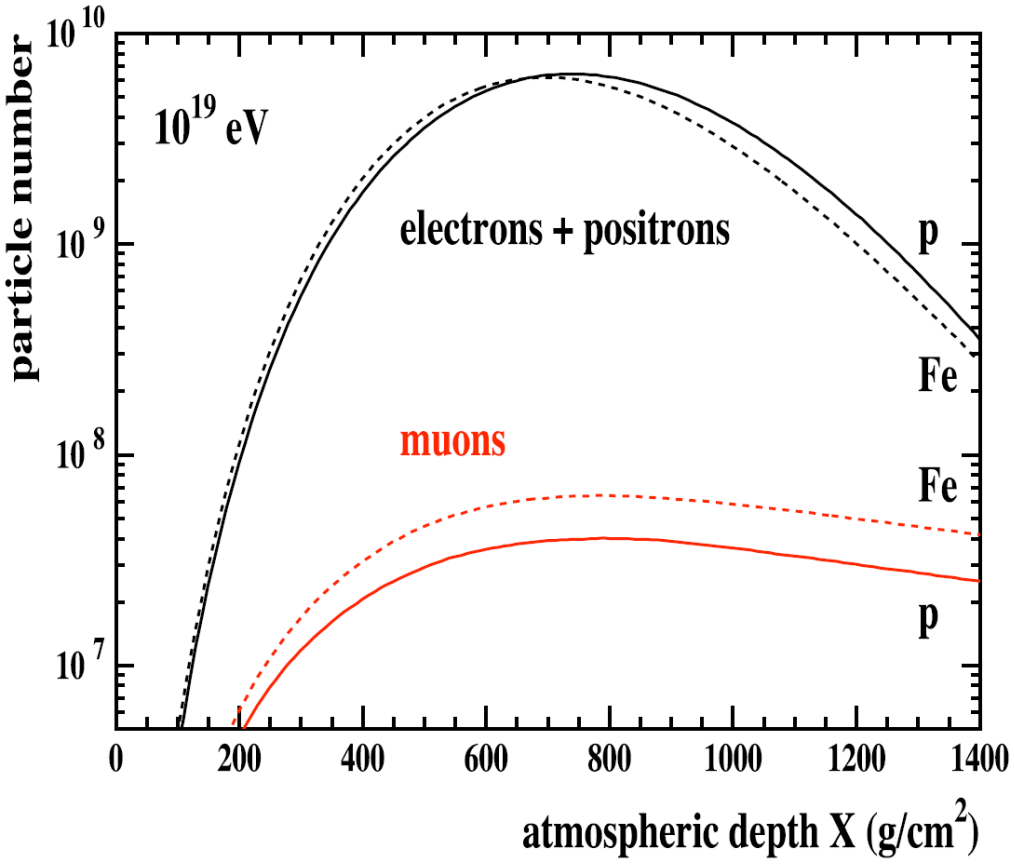

Figure 3.1: Longitudinal shower profiles. Shown are the number of electrons with $E_{\text{kin}} > 250\,\text{keV}$ and muons with $E_{\text{kin}} > 250\,\text{MeV}$. The solid lines give the distribution for a proton primary, the dashed lines give the distribution for an iron primary. (From [67].)

3.2 Detection techniques

Several established techniques for the detection of air showers exist. They all aim at reconstructing the shower geometry, which is defined by the shower axis (the path of the shower development through the atmosphere) and the position of the shower core, that is the point where the shower axis enters the ground. The different techniques are described in the following. The detection techniques used by the Pierre Auger Observatory are described in more detail in chapter 4, as this analysis was done with data from the Pierre Auger Observatory.

3.2.1 Detection of charged secondary particles at ground level

The measurement of charged particles at ground level is the oldest method to detect air showers. An array of particle detectors, for example scintillators or water Cherenkov detectors are used. Because of the high number of secondary particles, only a small fraction of the total detector area (in the percent range or below) has

to be instrumented for a successful sampling of the particle densities. From the measured particle densities, the shower core position and the total number of particles can be calculated. From the timing information in the different detectors, the shower front and perpendicular to it the shower axis can be reconstructed.

The reconstruction of the primary energy is also possible with different methods depending on the used detector. Composition information can be gained from several parameters: the electron-muon number ratio, the arrival time distribution of the particles, the curvature of the shower front and the slope of the lateral particle distribution, which all depend on the shower maximum $X_{\max}$, which is not directly detectable with a surface detector. This results in a dependence on the used air shower Monte Carlo model for the reconstructed values.

3.2.2 Measurement of Cherenkov light

Many particles in an air shower have relativistic velocities. One third of the electrons in an air shower emit Cherenkov light[73] in the forward direction, with an opening angle of 1.3° at sea level in air. Electrons have a very low Cherenkov threshold of 21 MeV at sea level and contribute mostly to the Cherenkov light in air showers. Two techniques are used to study air showers by the detection of Cherenkov light: Light integrating detectors, consisting of arrays of upward looking photo-multiplier-tubes (PMTs) and imaging detectors, consisting of light collecting mirrors and cameras with segmented read-out.

Light integrating Cherenkov detectors use arrays of PMTs to measure the lateral distribution of the Cherenkov photons over a large area. The empirical relation for the lateral distribution of Cherenkov light is

$$C(r) = \begin{cases} C_{120} \cdot exp(s[120 - r/\mathrm{m}]); & 30\,\mathrm{m} < r \leq 120\,\mathrm{m} \\ C_{120} \cdot (r/120\,\mathrm{m})^{-\beta} & 120\,\mathrm{m} < r \leq 350\,\mathrm{m} \end{cases} \tag{3.13}$$

with C_{120} the Cherenkov light intensity at 120 m distance from the shower core and s the exponential inner slope and β the outer slope. The primary energy is correlated with the Cherenkov light intensity at 120 m, C_{120} grows with $E^{1.07}$. The shower maximum $X_{\max}$ is approximately linearly related to the exponential slope s. With the relation between shower maximum and the mass of the primary particle, light integrating Cherenkov detectors are able to measure the energy and the composition of cosmic rays. For more information see [74] and [75].

Imaging Cherenkov detectors are mainly used in TeV γ-ray astronomy. Examples for Cherenkov telescopes are H.E.S.S[76], MAGIC[77] and VERITAS[78].

For both Cherenkov detection methods, the integrating and the imaging type, the light flux is so low, that only moonless nights can be used for the observation of air showers by the detection of Cherenkov light. This leads to a duty cycle of 10%. The same is true for the detection of fluorescence light, described in the next section.

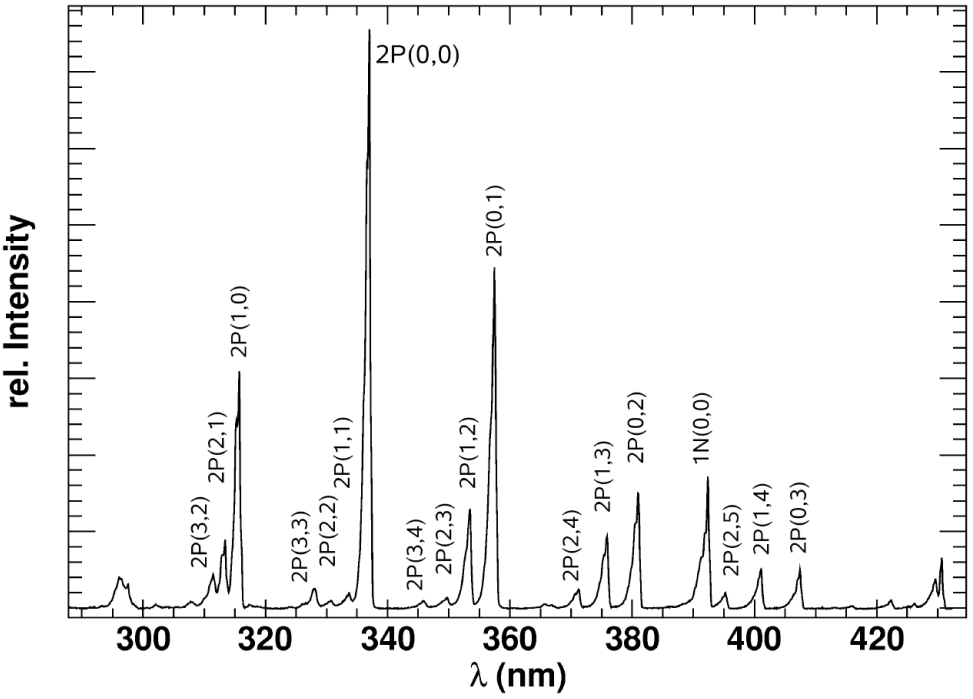

Figure 3.2: This plot shows the fluorescence light spectrum of air measured by the AIRFLY experiment with an electron beam of 3 MeV at 20° C and a pressure of 800 hPa. The spectroscopic identification for every line is given. Figure from [79],[80].

3.2.3 Detection of fluorescence light

The study of air showers by the measurement of fluorescence light is possible for very high energies of cosmic rays $E \gtrsim 10^{16}$ eV. With this technique, the longitudinal shower profile can be directly measured. The fluorescence observation of air showers has the same limitation as the Cherenkov observation: Data taking operations are only possible in clear moonless nights, which limits the duty cycle to around 10%.

The fluorescence light is emitted by nitrogen molecules that are excited by the passage of the charged particles of the air shower trough the atmosphere. Several emission bands exist. Most of the fluorescence light emission is found in the near UV range with wavelengths between 300 nm and 400 nm. The lifetime of the excited states is 10 ns and the fluorescence light is emitted isotropically. A spectroscopic measurement[79],[80] of the emission bands is found in figure 3.2.

The number of fluorescence photons produced per deposited energy is called the fluorescence yield. It depends on the gas mixture and the atmospheric conditions. Competing with the de-excitation of the nitrogen molecules by fluorescence light emission is the de-excitation through collision, the so called collisional quenching (see [81]). Collisional quenching is increasing with pressure and almost cancels the density dependence of the energy deposit per unit length of particle trajectory. This results in a rate of 4 - 5 fluorescence photons produced per meter and charged shower particle which is only weakly height dependent at the relevant altitudes.

Recent progress in the measurement of the fluorescence yield by several experiments is summarized in [82]. The fluorescence yield is currently only known to a precision of about 15% [83].

The fluorescence yield is independent of the energy of the exciting particle. Together with the atmospheric dependence of the fluorescence yield this allows a calorimetric measurement of the energy deposited in the atmosphere. Around 90% of the total shower energy is converted to ionization energy and hence is accessible for detection. This value has to be checked with simulations.

The full reconstruction of an air shower profile needs the reconstruction of the shower geometry, the calculation of the Cherenkov light fraction in the detected light flux and absorption of light in the atmosphere, which is wavelength dependent. The Cherenkov light can either be treated as background light contribution or as independent signal[84]. From the longitudinal shower profile, the Cherenkov light contribution in the detected signal can be calculated from electron energy distributions and models for the angular dependence of Cherenkov radiation[8],[85],[86],[87].

Several possible observation methods exist: One is the observation of the air shower by one fluorescence telescope (monocular observation). The image of the light track gives the shower-detector plane (SDP) (see figures 5.1 and 5.2)[8],[88]. From the time sequence of the PMT signals follows the orientation of the shower within the SDP. The typical reconstruction resolution is 1° for the orientation of the SDP and 4° to 15° for the angle of the shower axis inside the SDP[89].

Another observation geometry is the stereo observation. Stereo observation means that the air shower is observed by two fluorescence telescopes that are spatially separated. The angular resolution of a reconstructed air shower observed in stereo mode is of the order of 0.6°[89]. The detection of an air shower in more than two detectors is possible. The Pierre Auger Observatory, for example, has detected several air showers with three or even all of its four fluorescence detectors. Because of the low number of these events, no special reconstruction method is used and these air showers are reconstructed with the standard hybrid reconstruction method (see chapters 4.2 and 5).

Another observation method is the so called hybrid observation method. In this method, the timing information of surface particle detectors is used to measure the arrival time of the shower front on the ground. With the hybrid observation method a similar angular reconstruction quality as in the stereo case can be achieved[90],[91].

The atmosphere is an important part of the detector for the fluorescence observation of air showers. Possible changes in the state of the atmosphere have to be continuously monitored. Most important is the measurement of the wavelength dependent Mie scattering and the detection of clouds in the detector field of view[92],[93],[94].

3.2.4 Detection of radio signals

Air showers produce also radio frequency electromagnetic waves. The detection of air showers by these radio waves was first predicted by Askaryan in 1961. Experimental

difficulties in the detection of the radio signal were only recently overcome. The theory describing radio wave production is not complete and several production mechanisms are proposed. One is the Askaryan-effect[95], which is the coherent Cherenkov radiation of the charge excess. The other is the geosynchrotron effect[96] due to the acceleration of the charged shower particles in the Earth's magnetic field. Several experiments are currently working in this field.

3.3 Summary

The phenomenon of extensive air showers was described in this chapter. The detection of EAS as a means to study cosmic rays was explained for several detection techniques. In the next chapter, the Pierre Auger Observatory, which is the largest observatory for cosmic rays, is introduced. It uses a hybrid approach of detecting the same air shower simultaneously with several detection methods. The main detection methods are the detection of secondary particles at ground level and the detection of fluorescence light. The shower reconstruction methods used by the Pierre Auger Observatory and also for this analysis are described in the next chapter.

4. The Pierre Auger Observatory

The Pierre Auger Observatory is the largest observatory for the study of ultra high energy cosmic rays. It was planned as "one observatory with two sites", one on the northern and the other on the southern hemisphere, to achieve a full sky coverage. Construction for the southern site, located in the "Pampa Amarilla", close to the city of Malargüe, Province Mendoza, Argentina, started in 2001. Data taking operations started in January 2004, with a continuously growing detector. The construction of the southern site was completed in 2008. The Pierre Auger Observatory uses an array of 1600 water-Cherenkov detector stations, the so called Surface Detector (SD) and 27 fluorescence telescopes, located at the border of the array in five sites, that overlook the array, the so called Fluorescence Detector (FD). A picture of a single SD station and a FD telescope building can be found in figure 4.1. A map of the observatory can be found in figure 4.2. The simultaneous detection of extensive air showers with surface and fluorescence detectors is called the hybrid detection principle. In the following chapter, the Surface Detector, the Fluorescence Detector and the extensions to the Pierre Auger Observatory are described.

4.1 The Surface Detector

The Surface Detector of the Pierre Auger Observatory is the detector part that samples secondary shower particles at ground level. The surface detector consists of 1600 water Cherenkov detector stations that are positioned on a hexagonal grid with a spacing of 1500 meters between single detector stations. The whole surface detector array covers an area of 3000 km^2. Only a small part of the total area has to be covered by the detectors because of the high number of secondary particles. This fraction is around 5×10^{-6} for the surface detector array. Each of the detector station works autonomously, and communicates with the central data acquisition (CDAS) via a wireless network.

A schematic of a single SD station can be found in figure 4.3 and a picture of a deployed SD station can be found in figure 4.4. Every detector station consists of a cylindrical water tank with an area of ten square meters filled with twelve tons of ultra pure water. The tank walls are lined with Tyvek©, a plastic material that is highly reflective. Three twelve inch photomultiplier tubes (PMT) monitor the water volume. A GPS clock is used to get timing information for the station. A communication antenna is used for the data uplink to a concentrator, usually a large radio tower located close to each one of the four fluorescence detector buildings. The clock, antenna and PMTs are operated by an electronics package that is part of the

Figure 4.1: This picture shows one of 1600 Surface Detector stations in the front and one of four standard Fluorescence Detector buildings with its communications radio tower in the back.

event trigger. Power for the station comes from a solar panel with a battery as buffer to allow the operation without sunlight.

Air showers are detected by their secondary particles: Muons and a small fraction of electromagnetic particles that enter the water volume of the detector station. Many of these particles have a higher velocity than the speed of light in water and produce light via the Cherenkov effect. This Cherenkov light is detected, either directly or after reflection of the tank walls, by the PMTs. The amount and time structure of the measured light is analyzed by the detector station, and if specific properties are met, a trigger for the single station is generated. If several stations close together have triggered, data from all stations in a larger part of the array surrounding these stations is read out by CDAS and stored in the raw data stream. Several SD trigger levels exist. For more information on the SD trigger levels see [98].

4.2 The Fluorescence Detector

The Fluorescence Detector (FD) of the Pierre Auger Observatory is the detector part that detects cosmic rays by measuring the longitudinal profile of extensive air showers by measuring the fluorescence- and Cherenkov-light that is produced. A detailed description of the FD can be found in the paper ”The fluorescence detector of the Pierre Auger Observatory”[99]. In the following, a brief overview of the detector is presented.

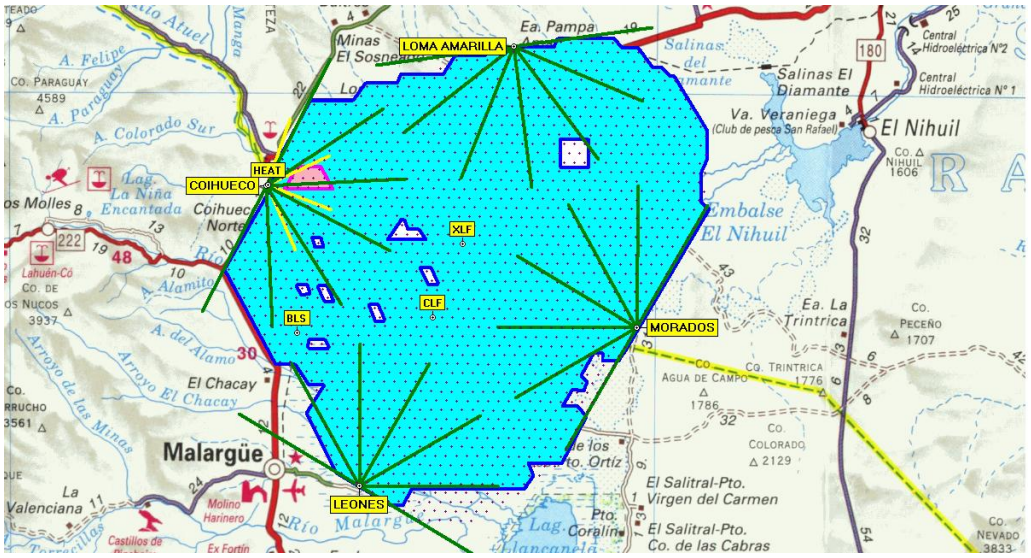

Figure 4.2: This map shows the southern site of the Pierre Auger Observatory located close to the city of Malargüe in Argentina. Each blue dot represents one of 1600 surface detector stations. The blue area shows the actual instrumented area. Some areas are not filled because of problems with terrain access. The location of the five fluorescence detector buildings at the borders of the surface detector array and their names are shown in yellow. The field of view borders of the fluorescence telescopes is shown with green lines and the field of view of the HEAT telescopes is shown with yellow lines. In addition, three installations of the atmospheric monitoring are shown: the balloon launching station - BLS and the two LASER facilities - CLF and XLF (see chapter 4.2.3).

The Fluorescence Detector consists of 24 fluorescence telescopes that are situated in four buildings at the edge of the SD array overlooking the array and studying the atmosphere above the array, see figure 4.2. Every FD building houses six telescopes. The FD buildings are located on small hills at the borders of the SD array. The names of the FD buildings in clockwise sequence are Los Leones, Coihueco, Loma Amarilla and Los Morados, starting with the south building. The entity of six telescopes is often called an ”eye”. The High Elevation Auger Telescopes - HEAT form a fifth eye (with only three telescopes) and is located close to the standard telescope building Coihueco, see chapter 4.4.1.

Each telescope has a field of view of 30°×30° in azimuth and elevation. Combined, one eye has a field of view of 30° in elevation and 180° in azimuth. A schematic view of an FD building (or eye) is shown in figure 4.5.

A telescope consists of the telescope optics, the PMT camera and the read-out electronics. A schematic of a single telescope is shown in figure 4.7. The optics system of an FD telescope consists (following the way of the light) of a filter, a corrector ring, a spherical mirror and the PMT camera. The entrance window of the telescope is made of Schott M-UG 6 filter glass [100] to absorb visible photons. The filter glass has a high transmitivity for wavelengths between 290 nm and 410 nm (see figure 4.6) which is the wavelength range of the fluorescence spectrum (see

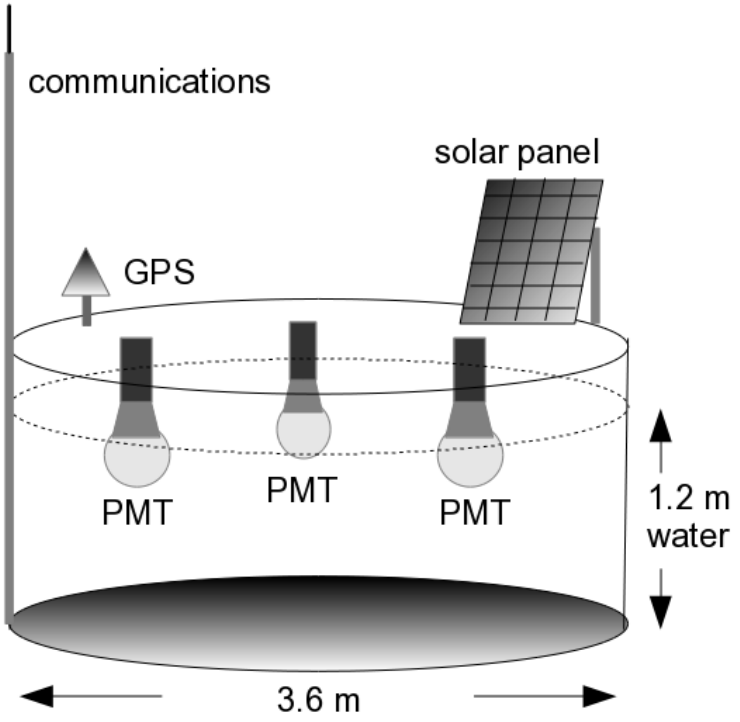

Figure 4.3: A schematic of an Auger SD station. Shown is the water tank, the three PMTs, the solar panel, the GPS antenna and the communications antenna. From [97].

figure 3.2). The filter is needed to reduce the much higher number of background photons (outside the fluorescence wavelength range) which would otherwise make the detection of the very faint fluorescence light impossible.

The telescope design is a modified Schmidt camera design that partially corrects spherical aberration and removes coma aberration. The mirror of the telescope has an area of around $13\,\mathrm{m}^2$ and is segmented in two configurations: Half of the standard telescopes use a tessellation of 36 rectangular shapes as mirror segments and the other half of the telescopes use 60 hexagonal mirror segments. The shape of the so formed main mirror is the same for both configurations. The HEAT telescopes use the hexagonal mirror configuration.

The change from the standard Schmidt telescope design is the use of a corrector ring instead of a full correction plate at the telescope opening. The corrector ring is the circumferential part of the standard corrector plate of a Schmidt telescope and is built of 24 segments. The aperture of the telescope is enhanced by a factor of two when using the corrector ring compared to a design without corrector ring. The light that enters the telescope through the filter passes the corrector ring and is reflected from the mirror on to the camera where it is detected. The camera consists of 440 pixels arranged in a geometric matrix in the focal plane of the telescope. The camera has 22 rows of pixels and 20 columns. Each pixel consists of a light concentrator and

Figure 4.4: This picture shows one of 1600 Surface Detector stations deployed in the pampa.

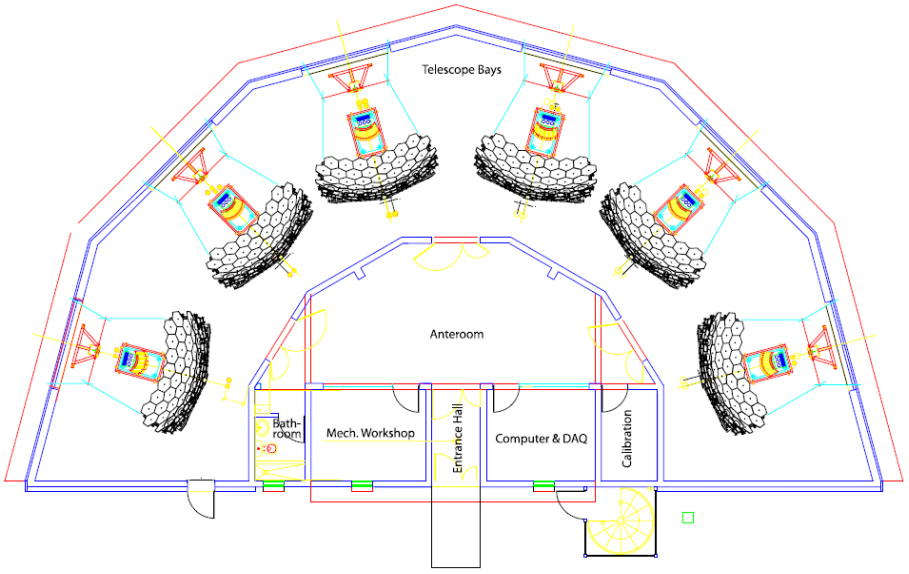

Figure 4.5: A schematic view of a standard FD building with its six telescopes is shown. Figure from [99].

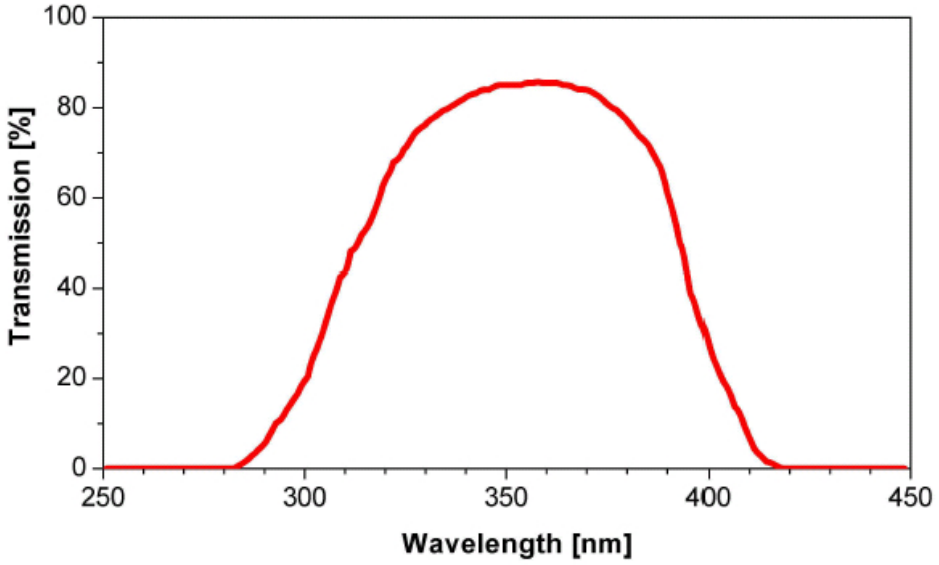

Figure 4.6: Shown is the relative transmission coefficient of the MUG-6 filter glass used in the aperture of the FD telescopes. Figure from [99].

a photomultiplier and has a viewing angle of around 1.5°. The spherical form of the focal plane leads to dead space between the single pixels when mounted. This dead space is covered with reflective light collectors, that transfer the light from the dead space into the PMTs. The PMTs are of the type PHOTONIS XP3062 [101] with a hexagonal window.

The electronics for the telescopes was specially designed to fulfill the requirements of a fluorescence detector. A schematic overview of the hierarchical FD data acquisition (FDAS) and the used electronics is shown in figure 4.8. For more details on the electronics see the paper "The fluorescence detector of the Pierre Auger Observatory"[99]. The timing information for each eye is generated by a GPS clock. The information that is written in the data stream is the PMT signal versus time. The analogue PMT signal is therefore digitized by an analogue-to-digital converter (ADC) and the data consists of ADC counts versus time.

4.2.1 FD trigger description

The FD uses several trigger levels to reduce the number of non air shower events in the data stream and to guarantee that nearly all real shower events are in the data stream of the telescope. The first two levels are hardware triggers, implemented in the camera electronics for each telescope. The first level trigger (FLT) is the pixel trigger. The sum of the signal from several time bins is compared to a threshold value. The number of added time bins can be varied between five and 16. If the value exceeds this threshold, a pixel trigger is generated. The threshold is adjustable to give a constant trigger rate of 100 Hz per pixel. This adjustment is needed because the background light level changes with time. The second level trigger (SLT) generates an internal trigger, if the pixel triggers are on a straight line inside the

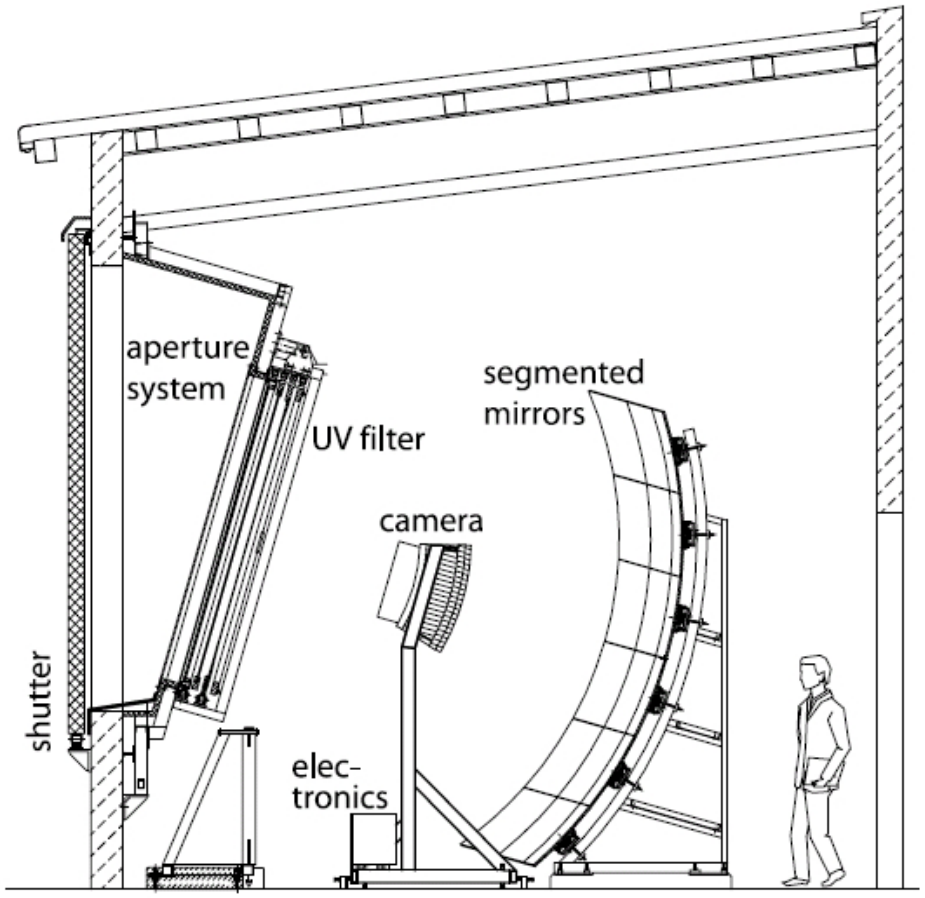

Figure 4.7: A schematic of a single FD telescope from the side is shown. From left to right one sees the telescope aperture, which contains the UV filter and the corrector ring, the camera and the mirror. Figure from [99].

camera. Therefore, the pixel trigger tracks are compared to all possible geometries of five pixels that form a straight track on the camera. To allow for possible defective pixels, only four pixels have to match the five pixel pattern. The five basic shapes are shown in figure 4.9. The number of total pattern classes checked, after rotation and mirror imaging is 108. The rate of SLT triggers ranges from 0.1 to 10 Hz per telescope. The next trigger step is a software trigger. Events that passed the SLT are stored on the MirrorPC for each telescope. The third level trigger (TLT) uses a software algorithm to remove noise events from the data. Possible noise event sources are lightning triggers, direct muon impacts on the camera and random pixel triggers. Distant lightning can lead to a high number of triggers over the hole camera for several seconds. By analyzing the multiplicity of triggered pixels 99% of lightning events (which triggered more than 25 pixels) are removed in a first step. In a second step the actual FLT data is checked to remove noise events with less than 25 triggered pixels. Events passing the TLT are then sent to the EyePC, where coincident events from the different telescopes are merged by an event builder. The rate of TLT triggers is 0.01 Hz per telescope. A T3 trigger request for events that

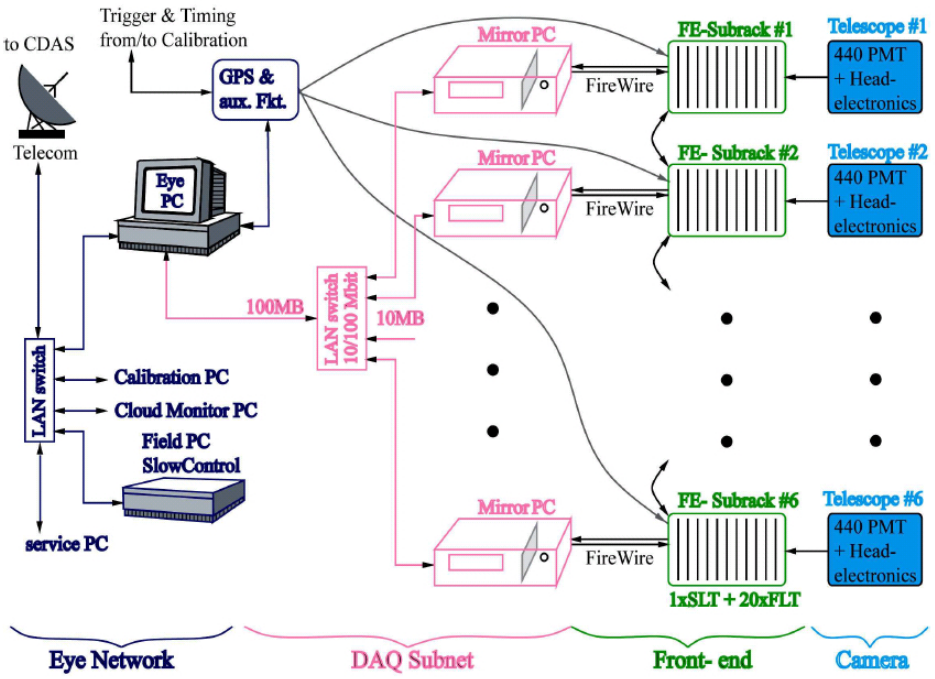

Figure 4.8: This picture shows the schematic data flow of the FD from right to left. Figure from [99].

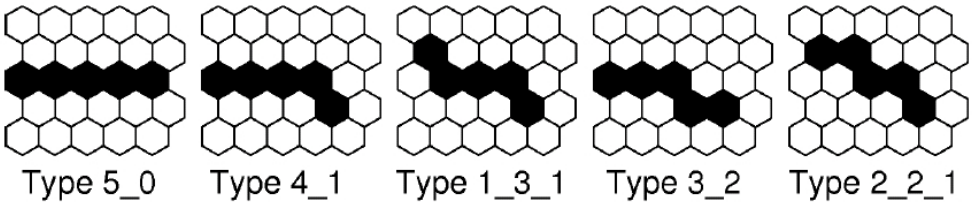

Figure 4.9: Basic Second Level trigger patterns that are accepted as straight lines. Rotations and mirror images of this basic patterns are also checked by the SLT. From[99].

pass basic quality cuts is send to CDAS, which is an external trigger for the SD. This external trigger is needed, because the SD is not fully efficient for low energy showers and an independent SD trigger is not generated. After receiving a T3 trigger, a part of the SD array in the telescope field of view is read out to get the data from the single SD stations to allow a hybrid reconstruction (see chapter 5). The rate of T3 triggers is 0.02 Hz per eye.

4.2.2 Energy calibration and energy scale

The general energy calibration of the FD telescopes is done by the so called drum calibration. For that, a calibrated light source is mounted in front of the telescope aperture and the response of the telescope to the known light flux is measured. The light source inside the drum has a wavelength of 375 ± 12 nm. The response

of every single PMT is saved in a database and that value is used for simulation and reconstruction. To study a possible time dependence of these values, the drum calibration is repeated after several months. The history of the different calibration constants is also saved in the database and used appropriately. Other calibration techniques using other wavelengths are also used. For more information on the telescope calibration see [99] and [102].

Several sources of systematic uncertainties for the FD energy exist and are related to the detector, the atmosphere and the used reconstruction technique. The current estimates for these uncertainties are given in the following (values from [103]). The uncertainty of the absolute fluorescence yield is 14%, the uncertainty from the absolute FD calibration is 9%, uncertainties from the molecular attenuation description and the multiple scattering model are 1% each, the invisible energy description gives an uncertainty of 4%. The effect of quenching (that is the dependence of the air fluorescence yield on the temperature and humidity of the air, see [80]) on the fluorescence yield gives an uncertainty of 5%, the FD wavelength response leads to an uncertainty of 3%, the aerosol attenuation has an uncertainty of 7% and the FD reconstruction method gives an uncertainty of 10%. All these effects are independent and lead to a total systematic energy uncertainty of 22%.

The energy resolution, that is the event to event statistical uncertainty is given as 10%[104].

4.2.3 Monitoring

The status of the Pierre Auger Observatory has to be measured constantly, to guarantee a high quality of the measured data. Since the atmosphere is part of the detector in a general sense, a monitoring of several atmospheric properties is also needed. Monitoring data is saved in a general monitoring database (and mirrors of the database) and can be used later for reconstruction or simulation purposes. The following describes the monitoring of the FD. For information on the SD monitoring see [105].

4.2.3.1 Detector Monitoring

An important task of the monitoring is to provide the necessary information to calculate the uptime of the detector for all possible detector configurations (see [106]). The uptime is the fraction of time that the detector was able to measure. Bad measurement conditions and internal dead times reduce this fraction. For that, the status of every hardware component down to the single PMT level of the FD is monitored. In addition, possible deadtimes from the DAQ electronics (on telescope or eye level, FDAS) are monitored. Deadtimes that are introduced by the communication system between the FD and CDAS together with veto deadtimes from the atmospheric monitoring (for example when the LIDAR is taking data) are also logged. The following uptime parameters are then stored for ten minute time bins in the monitoring database:

An individual uptime fraction for every telescope,

an uptime fraction for the whole eye,

the FDAS uptime fraction,

the CDAS connection fraction and

the CDAS uptime fraction.

For HEAT, the deadtime introduced by the T3 rate limiting is also included (see chapter 4.4.1.2). In addition the state of the FD electronics is measured, for example the pedestal and the variance of the ADC counts registered in every pixel. With this information, the background light detected by the telescope can be measured. Problems in the power supply or with the electronics in general can be seen in these values. Also monitored is the rate of triggered events per telescope or eye. Periods with an unstable detector can be identified and removed from the data analysis. The combination of all this information allows then the calculation of the uptime fraction for the detector.

4.2.3.2 Atmospheric Monitoring

Basic atmospheric parameters that are monitored at each of the FD buildings are temperature, air pressure and wind velocities. In addition, a rain sensor is installed at each of the eyes. If the wind is too strong or if rain or snow are falling at the site of the FD building, the shutters of the telescopes are automatically closed to protect the detector from damages. Temperature and density profiles were generated in the past by radio sondings, which were launched at the balloon launching station (BLS). At present meteorological information from the GDAS database (see [107],[108],[109]) is used to generate atmospheric profiles. Cloud cameras and satellite images are used to detect the presence of clouds in the detector field of view. A backscattering LIDAR (Light Detection And Ranging) at each FD building is used to detect clouds and measure their altitude inside the detector field of view.

Another important parameter to be measured are the aerosols in the atmosphere. They are responsible for the attenuation and scattering of light produced by the air shower. Several detection systems are used to monitor aerosols: The FD telescopes itself are used to detect light from LASER beams generated at the central laser facility (CLF) and the extreme laser facility (XLF)[1]. The CLF and XLF mimic air shower signals by using ultraviolet laser beams. Light from the beams gets scattered out of the beam and is then visible in the FD telescopes with a pixel pattern similar to that of air showers. The detected laser beams are also used to monitor other detector parameters of the FD telescope. It is also possible to generate artificial hybrid events with the LASER facilities. For that, part of the LASER light is transferred into an SD station that is located at the sites of the LASER facilities.

Data measured with the LIDARs are also used to quantify the aerosol content of the atmosphere. The scattering properties of the aerosols are measured with two atmospheric phase function monitors (APF). Two optical telescopes are used to measure the wavelength dependence of the aerosol attenuation, the horizontal attenuation monitor (HAM) and the fotometric robotic telescope for atmospheric monitoring

[1]Named so because of its remote location inside the array.

(FRAM). Data from all atmospheric monitoring sources are saved in the monitoring database and can be used when reconstructing air shower data. The use of most of these measurements depends on telescopes that have an absolute drum calibration.

A detailed description of the atmospheric monitoring and the impact of the measured parameters on the shower detection can be found in [110].

4.3 Hybrid Detection

The hybrid detection principle is the combination of the surface and fluorescence detection principle. For the so called "brass" hybrid events, the timing information from one surface detector station is used as additional information for the shower geometry reconstruction of the fluorescence information. Because of the much smaller uncertainties and overall better reconstruction quality compared with showers that were reconstructed with FD information only (called "FD mono"), this hybrid reconstruction is the standard reconstruction for FD information. The subset of showers for which an independent hybrid and SD reconstruction is possible is called "golden" hybrid. These events are used to cross-calibrate the two detectors. The systematic uncertainty of the energy measurement of the FD is transferred to the SD energy scale by the energy calibration between FD and SD. The resulting SD energy scale uncertainty is still smaller than the SD-only uncertainty, which depends on Monte Carlo simulations and is dependent on the used hadronic model. This cross-calibration allows the combination of the strengths of both detection concepts, leading for example to a measurement with the SD with 100% duty cycle and a small energy uncertainty.

4.4 Extensions of the Pierre Auger Observatory

The Pierre Auger Observatory, with its Surface and Fluorescence Detector, was designed for the detection of ultra high energy cosmic rays with energies above 10^{18} eV. After its completion, several extensions to the observatory were built. Two of these extensions, those to the surface and fluorescence detectors, aim to lower the energy range of the observatory by one decade down to 10^{17} eV. This is done by adapting the established detection methods. These two extensions are located close to each other at the designated location for extensions of the Pierre Auger Observatory, which is on the northwestern side of the SD array in the field of view of the Coihueco FD eye. This allows a hybrid measurement in this interesting energy range and gives an overlap with measurements from other cosmic ray experiments. The layout of the extension of the SD and FD can be seen in figure 4.10. Several other extensions are test beds for new techniques for the detection of air showers and use the know how and the chance of coincident measurements with an established cosmic ray detector.

4.4.1 The High Elevation Auger Telescopes - HEAT

HEAT, the High Elevation Auger Telescopes[111][112], are the extension of the Fluorescence Detector of the Pierre Auger Observatory. As explained earlier, the 24

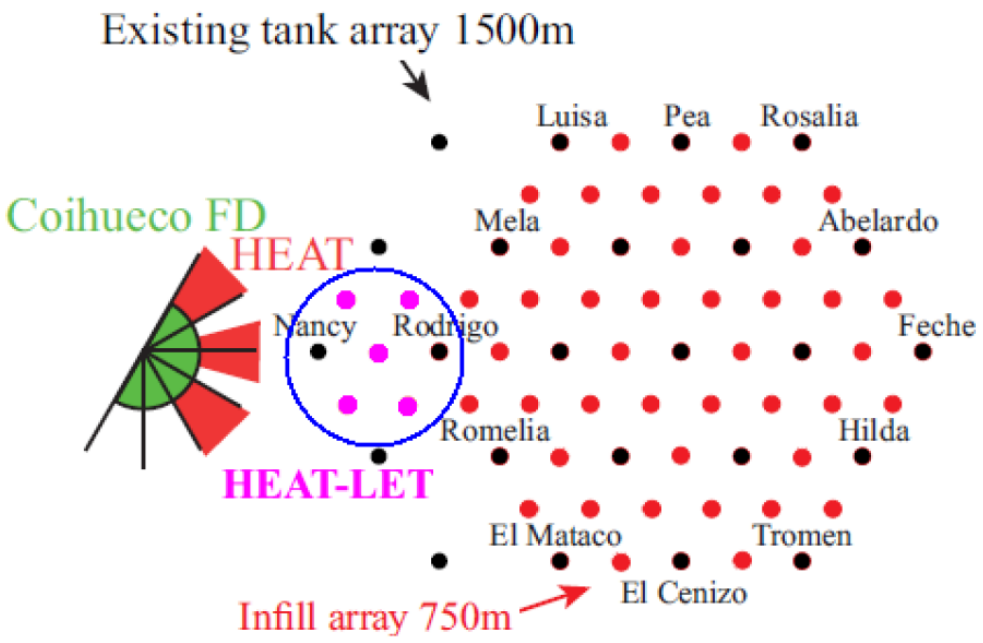

Figure 4.10: Shown is a map of the positions of the AMIGA infill detector stations and the position of the Coihueco and HEAT telescopes. AMIGA is the extension of the SD and HEAT the extension of the FD of the Pierre Auger Observatory. Black points show SD stations of the regular array, for some of them the individual station names are given in black. Red dots show the additional infill SD stations. Pink dots show the 5 HEATLET stations. The field of view of the Coihueco and HEAT telescopes is shown with green and red slices respectively. Shown is the status of the infill at the end of 2011.

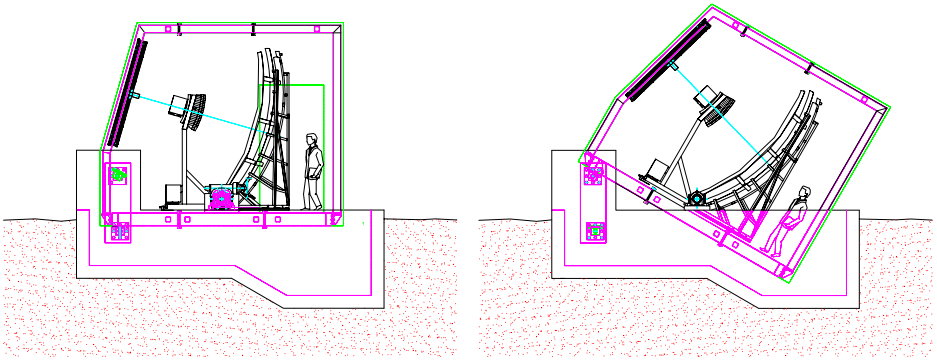

(a) HEAT in horizontal position **(b)** HEAT in inclined position

Figure 4.11: Shown is the technical drawing of one HEAT telescope. (a) shows the telescope in "downward" mode, (b) shows the telescope in "upward" mode. Only the telescope shelter and its ground plate are shown. The layout inside the shelter is the same as for a standard FD telescope.(Compare to figure 4.7).

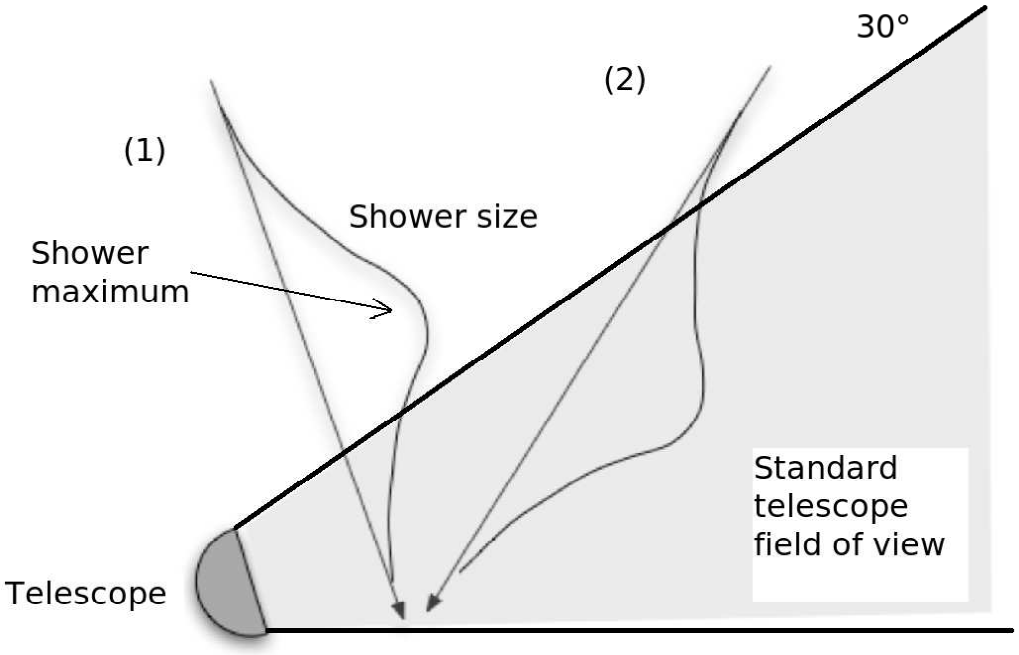

Figure 4.12: A schematic illustration of the geometric field of view bias of standard telescopes. Shown in gray is the field of view of one standard telescope (0° to 30° in elevation) and the longitudinal profiles of two air showers of the same low energy. The shower (1) on the left has its shower maximum outside the field of view and is discarded for data analyses, whereas the shower on the right (2) has its shower maximum inside the field of view. Figure adapted from [112].

telescopes of the FD (called standard telescopes) have a field of view from 0° to 30° in elevation. This leads to a geometric bias for low energy showers: Low energy showers produce less fluorescence light than higher energy showers. To detect these low energy showers with an FD telescope, the distance between the telescope and the showers has to be small. Together with the condition, that the shower maximum $X_{\max}$ has to be observed for a successful reconstruction, the limited field of view in elevation leads to a positive selection bias for showers with a large $X_{\max}$ (closer to the ground) and shower geometries which run towards the telescope and a negative selection bias for showers with a smaller $X_{\max}$ (higher in the atmosphere) and shower geometries which point away from the telescopes. This bias leads to a lower energy range for the standard FD telescopes of roughly $10^{17.6}$ eV. A schematic illustrating this bias can be found in figure 4.12. The shower on the left has its shower maximum outside the field of view of a standard telescope and is discarded in data analyses, whereas the shower on the right has its shower maximum inside the field of view of the telescope and is accepted for analyses.

Another challenge for the detection of close low energy showers is their high angular velocity. Because of the small distances they propagate through the field of view of the telescope in a shorter time than showers with larger distances. With a too coarse time resolution of the detector those events are not resolved with enough detail and are discarded.

Figure 4.13: A picture of the three tilted HEAT telescopes. Behind the middle telescope the DAQ container, which houses the shared electronics for all HEAT telescopes is visible. Further in the back a part of the standard fluorescence building Coihueco is visible. Picture source: H.O. Klages, KIT

Figure 4.14: View over part of the infill array from behind Coihueco and HEAT. On the left side the three HEAT telescope shelters in downward mode are visible. The green building on the right is the standard FD building Coihueco. On the right side of Coihueco the radio communication tower is visible. The structure with the metallic dome in front of Coihueco is a LIDAR, a part of the atmospheric monitoring of the observatory.

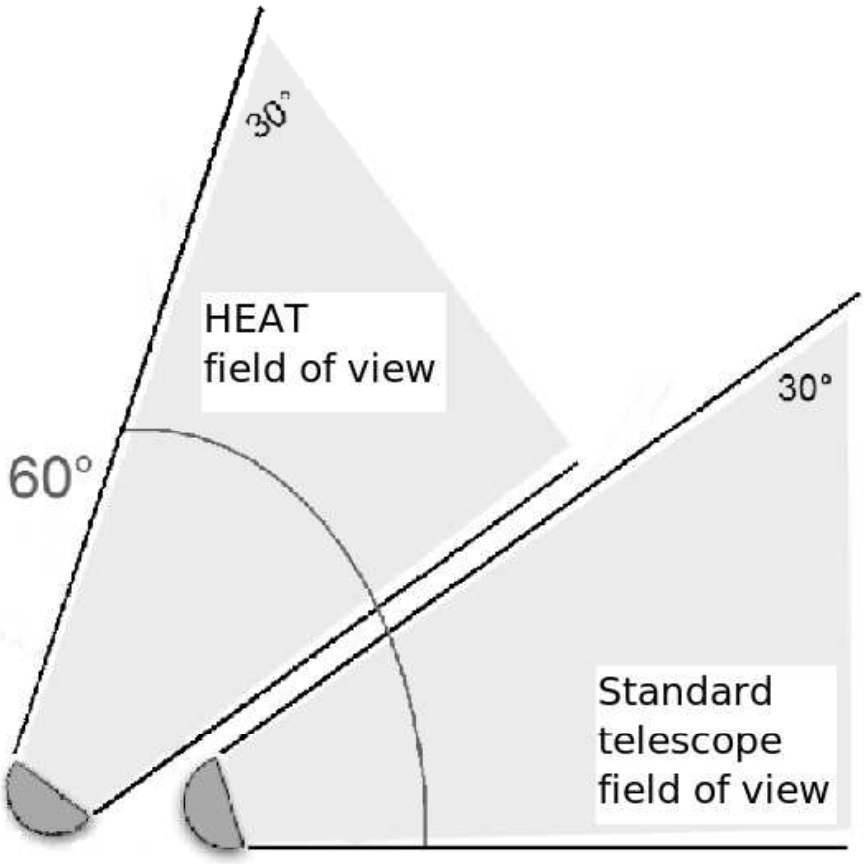

Figure 4.15: Reduction of the geometric field of view bias by HEAT: The combined field of view is extended from 0° to 30° in elevation to 0° to 60°. This allows the measurement of low energy air showers that have to be close to the telescope. Figure adapted from [113].

To reduce the geometric bias, the elevation coverage of the Fluorescence Detector has to be enlarged, see figure 4.15. This was done by the construction of three additional FD telescopes - HEAT. The optical system of these telescopes is a copy of that of the standard telescopes. The electronics of the telescopes were upgraded to allow a higher time resolution to handle the high angular shower velocities of close showers. The greatest change compared to the standard telescopes is, that the telescopes are not enclosed in a concrete building, but in single telescope shelters, that are mounted on top of a hydraulic mechanism. With this hydraulic system, it is possible to change the elevation of the optical axis of the telescopes between two pointings: 15° and 45°. The pointing of the optical axis of 15° leads to an elevation range from 0° to 30°, this is called the "downward" position. The pointing of 45° leads to an elevation range of 30° to 60°, this is called the "upward" position. The three telescopes are located at a distance of 180 meters to the standard FD building Coihueco, orientated so, that the HEAT field of view in downward position overlaps with that of some Coihueco telescopes. In upward position the HEAT field of view combined with the Coihueco field of view gives an elevation coverage from 0° to 60°.

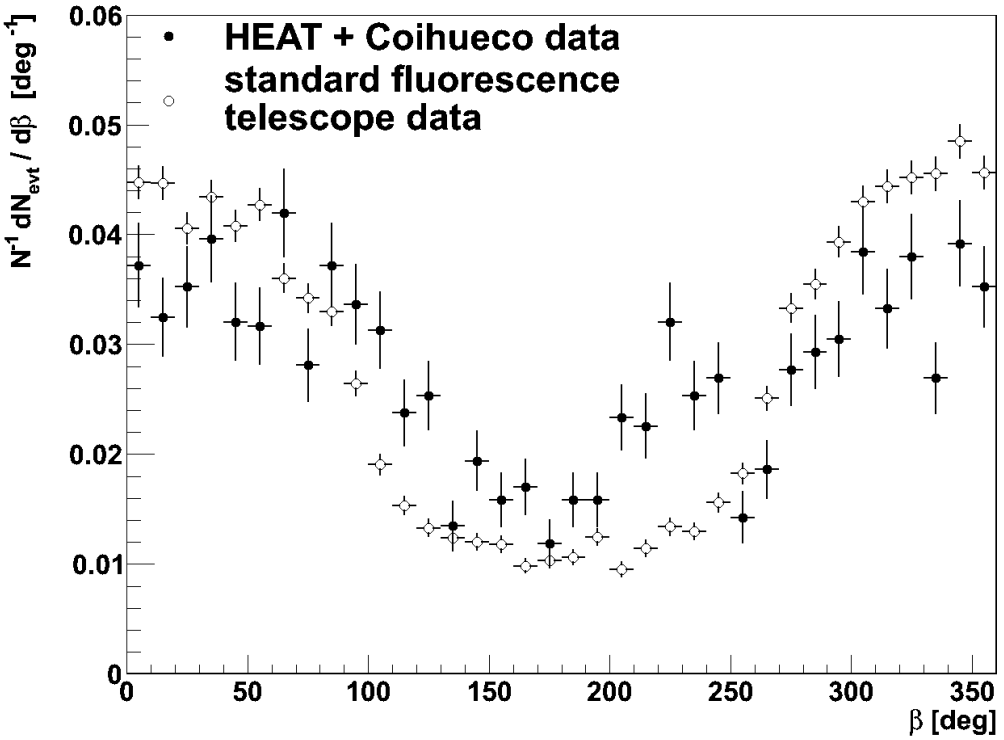

Figure 4.16: Reduction of the geometric field of view bias: Distribution of angle β, the difference of the azimuth angle of a shower and the azimuth angle of the mean line of sight of the telescopes. $\beta = 0°$ or $360°$ corresponds to the front of the detector, $\beta = 180°$to its back. The distribution for the combination of HEAT and Coihueco and for standard fluorescence telescopes are normalized by the total number of registered showers in each detector. Only hybrid showers with $X_{\max}$ in the field of view are considered. Figure from [111].

Only three telescopes are needed to achieve a high number of detected air showers because of the much higher rate of air showers at these lower energies.

The reduction of the geometric bias can be seen when comparing the arrival directions and shower distances of detected events between Coihueco only and the combination of Coihueco and HEAT. Figure 4.16 shows the distribution of the angle β for the combination of HEAT and Coihueco compared to that of standard telescopes. β is the difference between the azimuth angle of a shower and the azimuth angle of the mean line of sight of a telescope. $\beta = 0°$ or $360°$ corresponds to the front of the telescopes, $\beta = 180°$ corresponds to the back of the telescopes. More showers from "behind" the telescope are seen when HEAT is included. Figure 4.17 shows the distribution of the perpendicular distance between the telescope and the shower for the combination of HEAT and Coihueco compared to data from the standard telescopes only. More showers with smaller distances are seen by the combination of HEAT and Coihueco(see [111]).

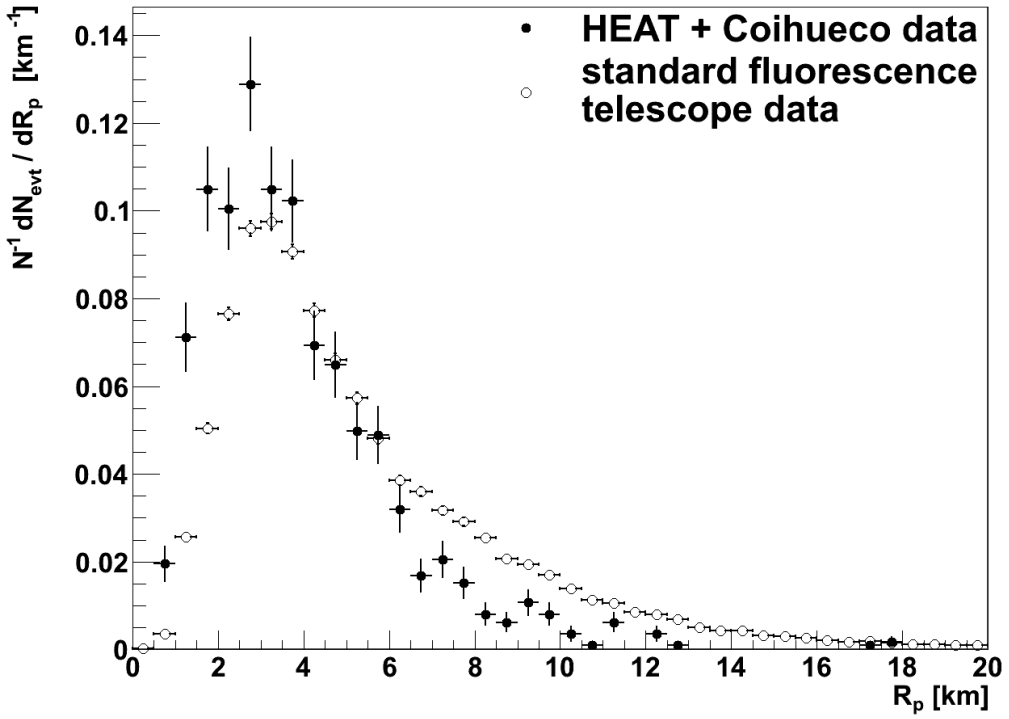

Figure 4.17: Reduction of the geometric field of view bias: Distribution of perpendicular distances from the shower to the telescope. The distribution for the combination of HEAT and Coihueco and for standard fluorescence telescopes are normalized by the total number of registered showers in each detector. Only hybrid showers with $X_{\max}$ in the field of view are considered. Figure from [111].

4.4.1.1 Comparison between HEAT and standard FD hardware

Whereas the optic system of HEAT is the same as that for the standard FD telescopes, the electronic system for HEAT was updated. The sampling rate of the electronics was changed from 10 MHz for the standard FD to 20 MHz for HEAT. This corresponds to a FADC bin size of 50 ns. The higher sampling rate is needed to measure showers close to the telescopes. This change in sampling rate leads to a change in the time interval of the FLT, that was also changed to 50 ns. The SLT is still operating with a time interval of 100 ns, but the number of FADC bins is doubled. These changes were also introduced in the detector description for the reconstruction and simulation modules in the Offline framework (see chapters 5 and 6).

4.4.1.2 HEAT Rate limiting

When HEAT was first operated in the Fall of 2009, it was soon measured that HEAT produced a very high rate of events when in upward mode, six to eight times higher than the rate when in downward mode. The reason for this are the very high number of very low energy showers that shine directly into the HEAT telescopes when they are tilted. For these events the high Cherenkov fraction is strong enough to trigger the telescopes. If HEAT would be allowed to operate with this high rate of events,

the SD and CDAS would be overwhelmed by the high number of trigger requests from HEAT. This would lead to an unstable operation of the SD in front of HEAT and lead to a loss of events from the SD. To reduce the effect of the high trigger rate on the SD, the dynamic T3 rate limiting was reactivated for HEAT. This rate limiting was integrated into the software of the FD in 2005 to reduce T3 trigger rates caused by lightning storms or the shooting of the LIDAR into the FD field of view but it was never used, because other ways to solve these specific problems were developed. The rate limiting reduces the T3 trigger rate of HEAT on a statistical basis. The description of the rate limiting given here follows that of the appendix C of the internal GAP-Note[2] 2010-123[114]. First, assume that two T3 events in the time interval Δt can be handled by CDAS. For an average event rate ω the average number of events in the time interval Δt is $N = \omega \cdot \Delta t$. For uncorrelated events (like cosmic rays) the possibility to observe m events in Δt is given by Poisson statistics

$$P(m; \Delta t) = (\omega \cdot \Delta t)^m \ \frac{e^{-\omega \cdot \Delta t}}{m!}. \tag{4.1}$$

The probability to observe more than two events in the time interval Δt is given by

$$P(m > 2; \Delta t) = 1 - \left(1 + \omega \cdot \Delta t + \frac{1}{2}(\omega \cdot \Delta t)^2\right) \ e^{-\omega \cdot \Delta t}. \tag{4.2}$$

If the value of this probability is smaller than the value of the allowed rate ω (ignoring units) for two consecutive events that would send a T3 to CDAS, the last event is vetoed.

The rate limiting was implemented with a rate of $\omega = 0.01\,\mathrm{s}^{-1}$ on 2010/05/17. From this date on HEAT was allowed to send T3 triggers to CDAS. The rate was changed to the higher value of $\omega = 0.02\,\mathrm{s}^{-1}$ on 2010/05/31 and operated with this value since this date.

The rate limiting implemented in this form leads to a bias on the field of view. This would further bias analyses that use hybrid events, because the T3 rate (and so the hybrid trigger rate) is limited for HEAT. To remove this bias, the same procedure applied on HEAT data by the hardware has to be used on the raw data from other eyes that will be used together with HEAT data. The rate limiting, first for HEAT data by the hardware, then on the raw data from other eyes reduces the number of events that can be used for analyses by up to 25%. For the combined Coihueco and HEAT reconstruction (COHE), the correction for the T3 rate limiting is done by the tool simpleMerger, written by S. Müller from the Karlsruhe group. It can be found in the OfflineKG extension of the Offline software framework. This tool merges the raw data from Coihueco, HEAT and the SD.

The veto to the events is applied on a statistical basis only. This leads to the effect, that high quality events are treated the same way as low quality events. Further studies on the high trigger rate of HEAT are underway[115]. The Karlsruhe group

[2]GAP-Notes are the internal papers of the Pierre Auger Collaboration. GAP stands for "Giant Array Project" and was the historical name of the observatory at the time of its conception.

is working on another method to reduce the high number of T3 triggers for HEAT, but this time with the goal to reduce low quality events and to keep a maximum of high quality events in the data. First tests were already done in the FD shifts of March and April 2012 [116].

4.4.1.3 Tilt Monitoring for HEAT

A completely new monitoring system is installed in the three HEAT telescopes, the so called Tilt Monitoring. This system was installed, because the stability of the optical system when the telescopes are tilted from the downward to the upward position is of utmost importance for a correct geometry reconstruction. The Tilt Monitoring is a set of four distance and four inclination sensors for each HEAT telescope. The Tilt Monitoring measures inclination and distance variations around the clock with a time resolution of 1 Hz, an angular resolution of 0.01 ° and a distance resolution of 0.1 mm. The used sensors types are potentiometers for the distance measurement and inclinations are measured with micro-electro-mechanical system (MEMS) sensors, which measure the the change in capacity introduced by the change in position of a seismic mass inside a capacitor(see [117]).

It was developed by J. Calvo de Nó from the Aachen group in his diploma thesis [113], before the construction of the HEAT telescopes had even started. For testing purposes, a prototype set of sensors was installed in one telescope bay of the standard FD eye Los Leones, where it was operated for one year. After the construction of the HEAT telescopes, the Tilt Monitoring was installed in every HEAT telescope shelter by the Aachen group. The used hardware is basically the same as that for the prototype. The only changes are the removal of the weather-station that was used in the prototype and a change from coated carbon fiber to temperature stable cables for the distance sensors because of problems with the handling of the fibers. The prototype sensors were reused in one of the HEAT shelters. All new sensors were calibrated with the method developed for the prototype system. A recalibration of the prototype sensors showed no changes in the sensor characteristics after over one year of operation. The mounting points of the sensors can be found in figure 4.18. The positions for the sensors are given when standing behind the mirror, looking towards the telescope aperture. The four inclination sensors are mounted an the following positions inside the telescope shelter:

1. base of the camera
2. top of the camera
3. top middle of the mirror and
4. left side of the shutter.

The distance sensors are mounted at the first point given in the following list, and then connected with the cables to the second point:

1. top left of mirror to top left of the camera

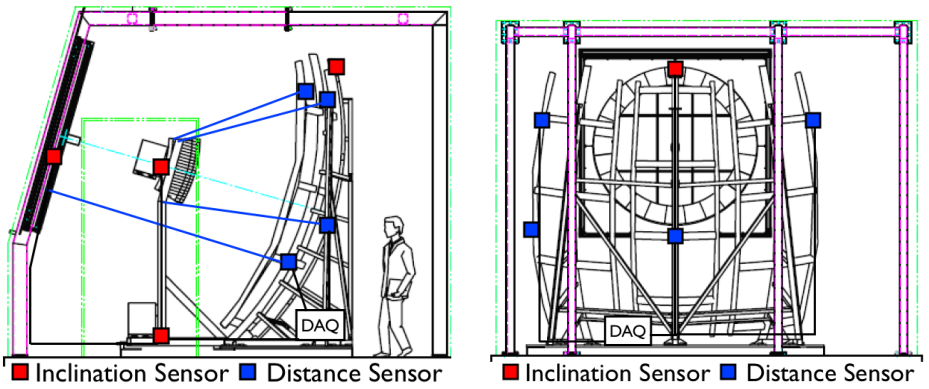

(a) (b)

Figure 4.18: Position of the Tilt Monitoring sensors inside the HEAT telescopes. The left picture shows the view from the side, the right picture shows the view from behind the mirror. The distance sensors are marked in blue, the inclination sensors are marked in red.

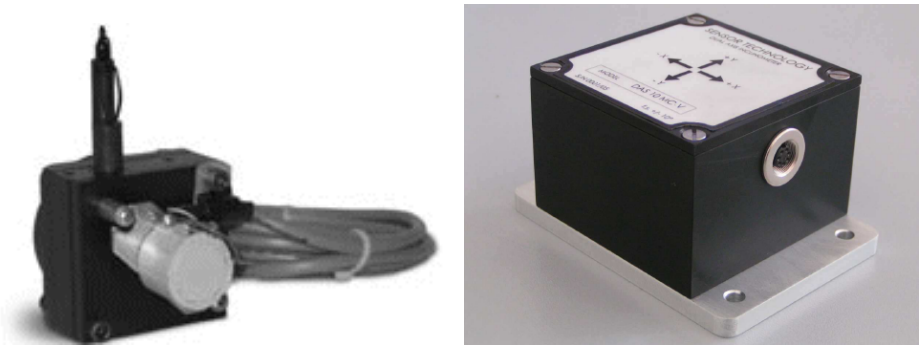

(a) (b)

Figure 4.19: Sensor types installed in the HEAT telescopes. 4.19a shows the potentiometer distance sensor type PTX-101 and 4.19b shows the inclination sensor type DAS-15-MC-RS232.

2. top right of mirror to top right of the camera
3. bottom left of the mirror to the shutter and
4. center of the mirror to a point beneath the camera.

With this setup, it is possible to measure changes in the distances or inclinations on a global scale or between important parts of the telescope optics when tilting the telescope.

An example measurement from the Tilt Monitoring is shown in figure 4.20. It covers a time span of roughly 9.5 hours. In this time, the telescope was tilted and immediately untilted. Then the telescope was tilted and untilted with breaks in the tilting and untilting process. Afterwards, the telescope was tilted for several hours

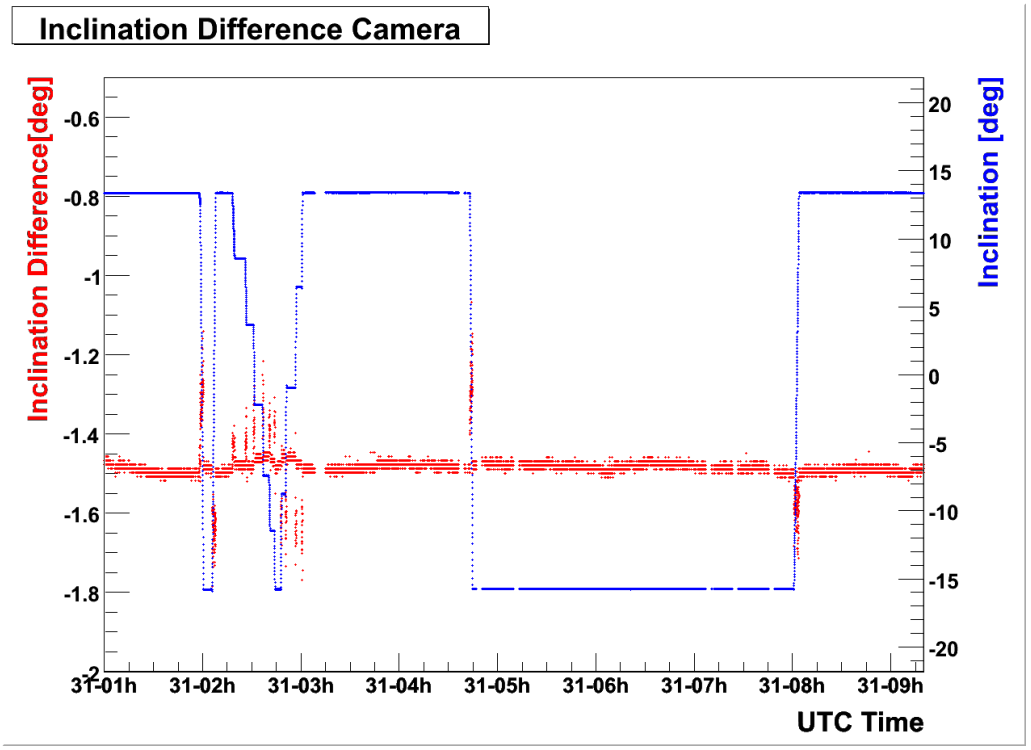

Figure 4.20: Data from the Tilt Monitoring for a 9.5 hour period. Shown in blue is the data from the tilt sensor one. A value of 13° corresponds to the downward position, a value of -16° corresponds to the upward position. In red, the difference between the inclination sensor one and the inclination sensor two is shown. A small offset of 1.55° is not corrected. Three cycles from downward to upward over different timescales are shown.

and then untilted again. These operations are clearly visible in the blue data points, which show the inclination of the ground plate of the telescope on a range from 13° (downward) to -16° (upward). The global offset of the measurement is not corrected, because only relative differences are studied. The red data points show the difference in inclinations between the ground plate and the top of the camera. An offset of 1.55° is not corrected. Changes in the difference are only visible for times when the telescope is actively moving. A short time after the tilting operation has stopped, the difference stabilizes on the value of 1.55 textdegree, the same value in tilted as in untilted position.

For a complete overview of the Tilt Monitoring, the sensors and the calibration procedure see the diploma thesis by J. Calvo de Nó [113], the PhD thesis by S. Schulte [118] and an upcoming GAP-Note on the Tilt Monitoring[119].

4.4.2 AMIGA - Auger Muons and Infill for the Ground Array

AMIGA - Auger Muons and Infill for the Ground Array is the extension of the surface detector of the Pierre Auger Observatory. It consists of two parts: An infill

to the array of SD stations and additional muon detectors close to the infill detector stations.

On an area of 23.5 km^2 61 additional SD detector stations are inserted into the standard SD grid, forming an array with a spacing of 750 meters between stations. The reduced spacing lowers the energy threshold for the detection of cosmic rays down to 10^{17} eV. The infill is located close to the standard FD building Coihueco and is covered by the field of view of Coihueco and HEAT, allowing again the hybrid detection of low energy showers with both extensions. The possibility for the installation of additional SD stations on an even smaller grid (433 meter spacing or smaller) in part of the infill exists.

The second part of AMIGA are additional muon detectors. They will be located close to every SD station in the infill area. They consist of buried scintillator muon detectors (MD) with an area of 30 m^2 each under 2.3 meters of soil. The soil is used as absorber for the rest of electromagnetic particles (electrons, positrons, photons) from the shower cascade and to give a lower threshold of roughly 1 GeV for the detection of muons. Together with its associated SD station, which measures muons and electromagnetic particles together, the measurement of the muons alone by the MD gives additional information on the shower development by allowing the separate measurement of electromagnetic and muonic parts of the shower front.

4.4.3 HEATLET

HEATLET - The HEAT Low Energy Trigger tanks are 5 additional SD stations inserted in the standard array closest to HEAT, that form a small infill array with 750 meter spacing of 9 stations between HEAT and the AMIGA infill array. With these stations directly in front of HEAT the number of detected hybrid events for the lowest energy showers detectable by HEAT is greatly enlarged. These stations were installed and included into the DAQ in the fall of 2011.

4.4.4 Auger Engineering Radio Array - AERA

AERA - The Auger Engineering Radio Array is the extension of the Pierre Auger Observatory that studies the possibilities for the detection of extensive air showers by their generated radio pulses with frequencies in the MHz range[120][121]. It is the successor to several smaller proof-of-concept setups that were located at different positions inside the SD array (see for example [122]). AERA is located at the designated part of the SD array for observatory extensions, where also the AMIGA infill is located and inside the combined HEAT and Coihueco field of view. This allows for possible super - hybrid events, which were recorded with the standard SD, the infill, the standard FD, HEAT and the radio detector (RD). AERA is planned in several stages. The construction of stage one of AERA, with 21 antenna stations was finished in 2010. Stage two and three aim to enlarge the covered area and use larger antenna spacings with up to 150 antenna stations on an area of 20 km^2. AERA stage one is currently taking data. A map of the AERA array is found in figure 4.22(a) and a picture of one AERA stage one antenna station is shown in figure 4.22(b)(both from [121]).

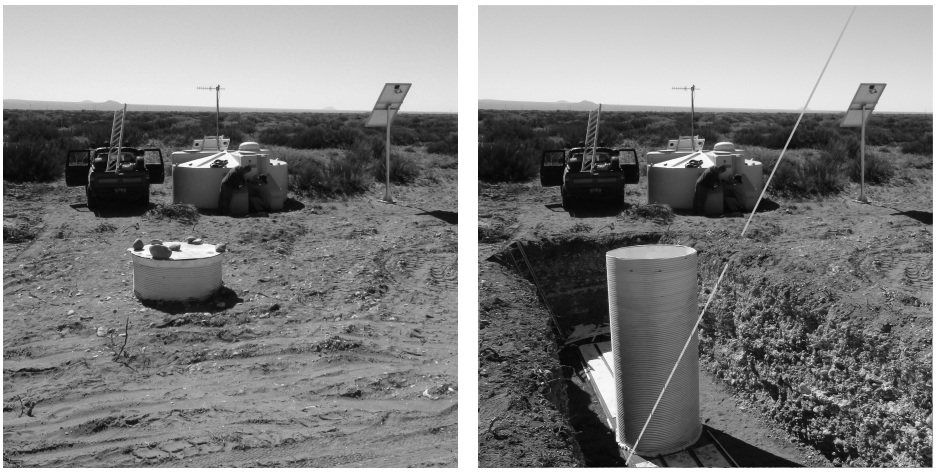

(a) (b)

Figure 4.21: The AMIGA detection concept. (a) shows a surface infill SD station with its associated muon counter already buried. (b) shows a photo montage depicting the detector concept: any impinging muon with an energy over one GeV propagates in the soil and is capable of reaching the buried scintillator. See chapter 4.4.2.

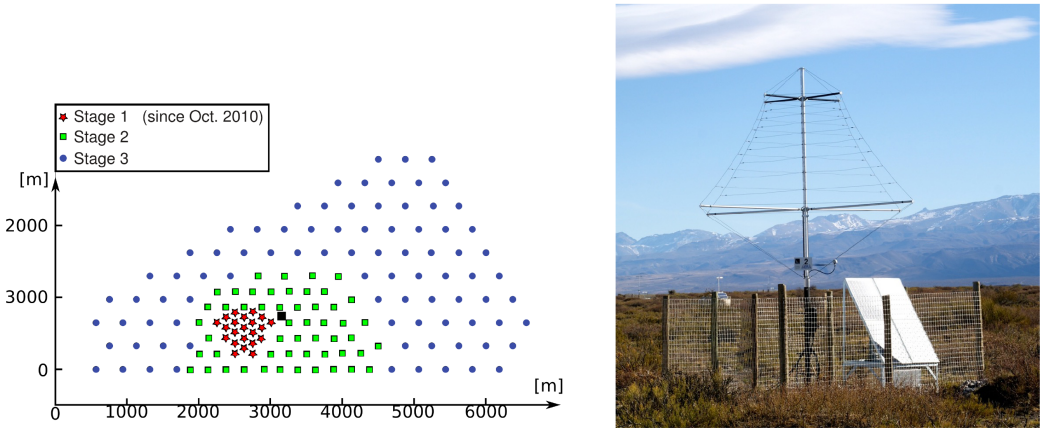

(a) (b)

Figure 4.22: A map of the AERA array on the left. The positions of antenna stations for the different phases of construction are color coded. On the right a picture of one AERA antenna station is shown. Both from [121].

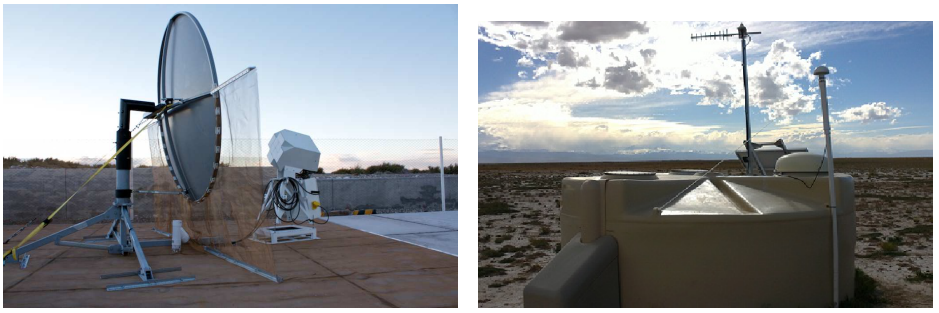

(a) (b)

Figure 4.23: Prototype experiments for microwave detection of air showers. 4.23(a) shows the antenna dish of AMBER installed close to the HEAT telescopes as an example for several experiments. 4.23(b) shows a SD station with an installed EASIER antenna (right mast, c.f. figure 4.3 and 4.4). Pictures from [123].

4.4.5 Microwave-detection of extensive air showers

The detection of cosmic rays by measuring radio emissions with frequencies in the microwave regime (GHz frequencies) that are generated by the shower cascade is studied with several prototype experiments located at different sites in the Pierre Auger Observatory. Two different techniques are explored: The use of large imaging dish antennas that overlook the SD array and the use of small horn antennas located on SD stations. The experiments using the first method are called AMBER (Air-shower Microwave Bremsstrahlung Experimental Radiometer), MIDAS (Microwave Detection of Air Showers) and FDWave. The second method is explored by EASIER (Extensive Air Shower Identification using Electron Radiometer)[123]. The microwave technique would allow a measurement of the longitudinal shower profile with a 100% duty cycle while using low cost commercial equipment. As an example, the antenna dish of AMBER and a SD station with an EASIER antenna are shown in figure 4.23.

4.5 Summary

The Pierre Auger Observatory, its detectors and their hardware were introduced. The general reconstruction methods for data were explained. The extensions of the observatory were described. In the next chapter, the flow of data reconstruction for data used in this analysis, that from the standard FD and HEAT, is described.

5. Air Shower Reconstruction

This chapter describes the reconstruction of air shower data at the Pierre Auger Observatory and that used for this analysis. At first, a short overview of the SD data Reconstruction is given, afterwards the reconstruction of hybrid data is explained in detail. For data taken with the HEAT telescopes modifications to the reconstruction are necessary. These modifications are also explained.

The goal of the air shower reconstruction is to reconstruct the energy, the particle type and the arrival direction of the primary cosmic ray that entered the atmosphere and produced the air shower that was measured by the Pierre Auger Observatory. This has to be done from the sampled secondary particle distribution at ground level for the SD and from the part of the longitudinal shower profile that was detected by the FD.

5.1 SD Reconstruction

The reconstruction of air showers detected with the SD of the Pierre Auger Observatory is done in several steps. The arrival direction of the air shower is reconstructed by fitting a curved shower front to the arrival times measured in the detector stations. For the energy reconstruction, a modified Nishimura-Kamata-Greisen (NKG) function is fitted to the signal measured in the single stations (see [124]). The measured signal is given in the unit vertical equivalent muon (VEM), that is the signal one muon that penetrates a SD station with a zenith angle of 0° is generating. The used NKG function is of the form

$$S(r) = S_{1000}(E, A, \theta)\left(\frac{r}{r_1}\right)^{\beta(\theta)}\left(\frac{r + r_2}{r_2 + r_1}\right)^{\beta(\theta)+\gamma} \tag{5.1}$$

with $r_1 = 1000\,\mathrm{m}$ and $r_2 = 700\,\mathrm{m}$ and r the distance to the shower core. S_{1000} is the energy estimator that depends on the energy E, the zenith angle θ and the primary particle type (atomic mass number A) and represents the signal at a distance of 1000 m to the shower core. $\beta(\theta)$ is derived from data and γ is zero for showers with a not too large number of stations. The energy estimator S_{1000} is chosen, because shower to shower fluctuations are minimal for this value. The optimal value is dependent on the spacing between detector stations and was studied in simulations. The zenith angle dependency for the S_{1000} energy estimator is calculated by the constant intensity cut (CIC) method (see [125] and sources therein) which gives a new energy estimator $S_{38°}$, so called for the zenith angle of 38°, which is the median

zenith angle for the SD zenith angle range from 0° to 60°. This zenith angle range is used, because the response of the surface detector changes with higher zenith angles. A different reconstruction method for air showers with higher zenith angles (called horizontal air showers) is used (see [124]). The energy dependence of S_{38° is then calibrated with the FD energy from golden hybrid events. A mass-estimator for SD data can be derived from the time structure of the signal measured in the stations, for example the rise time of the signal.

5.2 FD Reconstruction

Several reconstruction methods for data taken with the FD exist. Explained here are the FD mono reconstruction and the hybrid reconstruction that is an extension of the FD mono method. The first step is the reconstruction of the shower geometry and with this information then the profile reconstruction which leads to the energy reconstruction of the shower.

5.2.1 Shower geometry reconstruction

5.2.1.1 FD mono reconstruction

The reconstruction of the shower geometry is the first step in the reconstruction of the air shower information. The shower detector plane (SDP) (see figure 5.2) is the plane that contains the shower axis and the center of the eye. It is given by the pattern of triggered PMTs on the camera surface, see figure 5.1, which shows the pixel pattern of a typical FD event. The triggered pixels are marked by the filled hexagons. The time information of the pixels is color coded, from early (purple) to late (red). Grey pixels are accidental hits on the camera (background light or direct muon hits) that were removed from the reconstruction because they do not fit to the time structure of the event. A preselection on the triggered pixels, that allows only non isolated pixels in space and time, is used. A unit normal vector $\overrightarrow{n}$, the so called SDP vector, gives the orientation of the SDP. A convention that reduces the two allowed normal vectors for every SDP to one is used. A χ^2 minimization is used to determine the SDP that best describes the triggered pixel pattern. It uses the pointing direction $\overrightarrow{r_i}$ of the i-th triggered pixel. The used χ^2 function is

$$\chi^2 = \sum_i |\overrightarrow{n} \cdot \overrightarrow{r_i}|^2 w_i, \tag{5.2}$$

w_i is the signal in pixel i. After the SDP is fixed, the geometry is reduced to a planar problem.

The next step is the calculation of the shower axis inside the SDP. This is done by using the timing information from the triggered pixels to find the perpendicular distance R_p from the detector to the shower axis and χ_0, the angle of the shower axis inside the SDP (see figure 5.3). Again, a χ^2 minimization is used to determine the best fit parameters χ_0, R_p and t_0, which is the time the shower passes the point of R_p. The used χ^2 function is given as

$$\chi^2 = \sum_i \frac{(t_i - t_i^{\mathrm{exp}})^2}{(t_i^{\mathrm{err}})^2}, \tag{5.3}$$

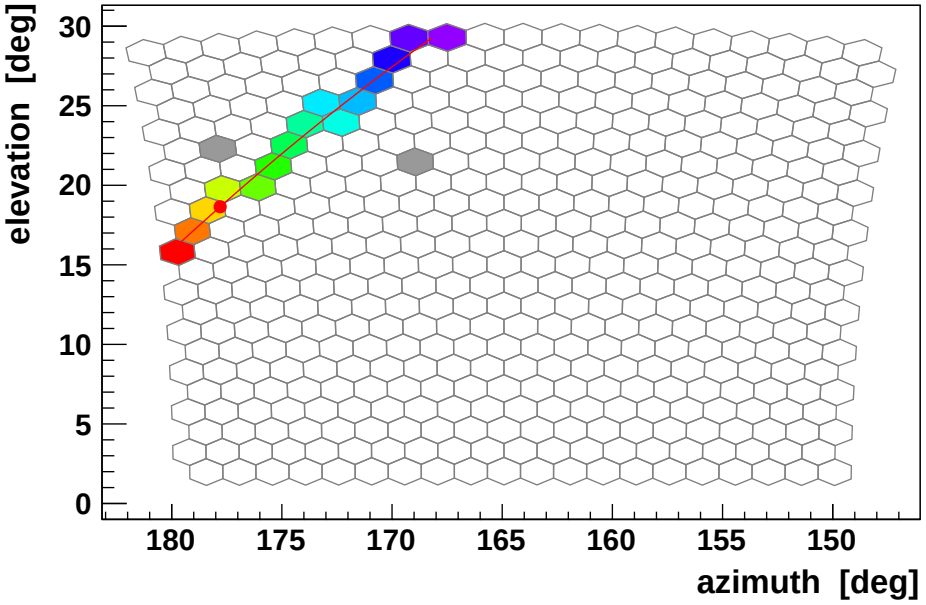

Figure 5.1: Pixel pattern of an FD event. The arrival time is color coded from purple (early) to red (late). The red line is a representation of the reconstructed SDP.

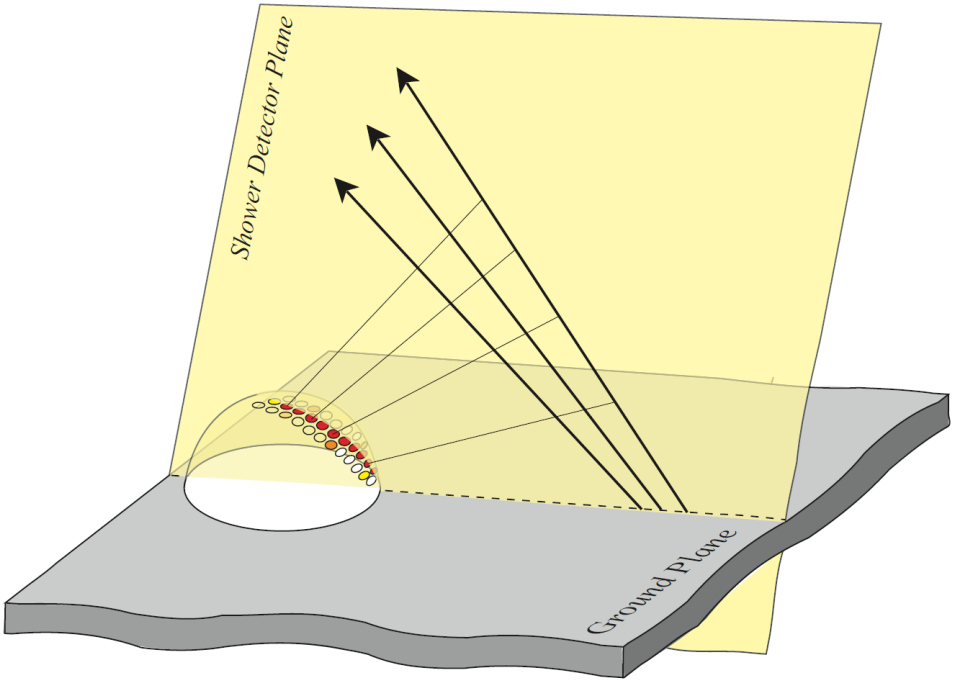

Figure 5.2: Illustration of the SDP. The SDP is given by the pattern of triggered PMTs. Several showers can have the same SDP. Figure from [126].

with t_i the measured arrival time of light from the shower at the telescope, t_i^{exp} the expected arrival time at the telescope and t_i^{err} the time uncertainty of the i-th pixel which measured light from the point S_i on the shower axis (see figure 5.3). The time uncertainty is mainly the pulse centroid uncertainty of the pixel, which stems from the finite extension of the single PMT field of view and the resolution of the data taking hardware. Typical values for the time uncertainty lie between 40 ns and 200 ns. For a detailed description see [126]. The expected arrival time t_i^{exp} can be derived from geometrical considerations. The propagation time τ_i^{shower} of the shower from a light emission point S_i to the reference point at time t_0 on the shower axis can be given as

$$\tau_i^{\mathrm{shower}} = \frac{R_{\mathrm{p}}}{\mathrm{c} \cdot \tan\left(\chi_0 - \chi_{\mathrm{i}}\right)}, \tag{5.4}$$

with c the speed of light and χ_i the viewing angle towards S_i. The propagation time τ_i^{prop} from S_i is

$$\tau_i^{\mathrm{prop}} = \frac{R_{\mathrm{p}}}{c \cdot \sin\left(\chi_0 - \chi_i\right)} \tag{5.5}$$

The combination of these formulae leads to

$$\begin{aligned} t_i^{\mathrm{exp}} &= t_0 - \tau_i^{\mathrm{shower}} + \tau_i^{\mathrm{prop}} \\ &= t_0 + \frac{R_{\mathrm{p}}}{c}\left(\frac{1}{\sin\left(\chi_0 - \chi_i\right)} - \frac{1}{\tan\left(\chi_0 - \chi_i\right)}\right) \\ &= t_0 + \frac{R_{\mathrm{p}}}{c}\tan\left(\frac{\chi_0 - \chi_i}{2}\right) \end{aligned} \tag{5.6}$$

for the expected arrival time. The correlation between times and angles for an example event is shown in figure 5.4. The main uncertainty in the fit result comes from the uncertainty of the shower axis inside the SDP. This uncertainty is dependent on the specific geometry and the observed shower track length. The large uncertainties that occur in the FD mono reconstruction method lead to large uncertainties in the calculation of the shower energy. These large uncertainties can be reduced by the FD stereo reconstruction method, which calculates the shower axis as intersection axis between the two SDPs from two different eyes. The probability to detect the same shower with two (or more) different eyes is only high for showers with high energies[1], which limits the applicability of this method.

5.2.1.2 Hybrid Reconstruction

A method to reduce the large uncertainties that can occur for the FD mono reconstruction method, the hybrid reconstruction method, is used at the Pierre Auger Observatory. It uses information from the FD and SD for the reconstruction of the shower geometry. The geometry reconstruction is improved by using the timing information of the SD station with the highest signal. A pixel view of an example

[1] Only showers with high energies produce enough light to be visible over the distances between FD eyes, which is of the order of 20 km or more

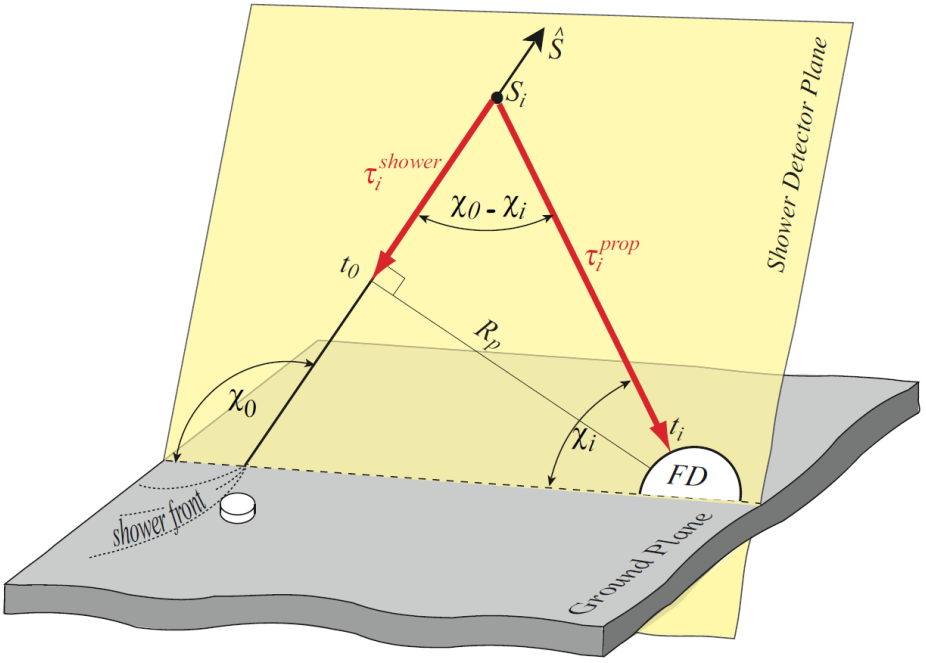

Figure 5.3: Illustration of the shower / detector geometry for an FD mono case. Figure from [126].

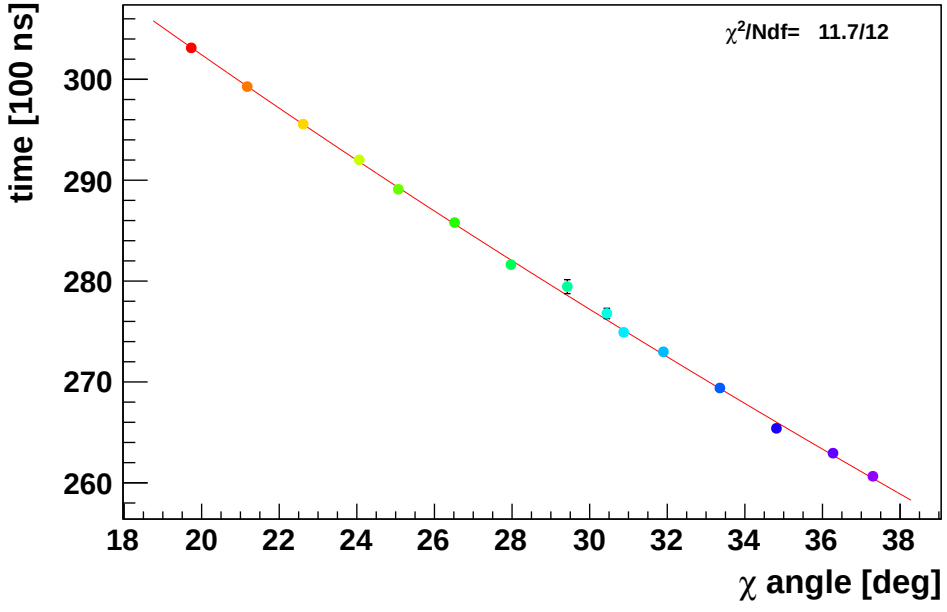

Figure 5.4: Time - angle correlation after fitting for an example event. The dots are the measured (χ_i, t_i)-pairs which are color coded depending on the arrival time from early (purple) to late (red).

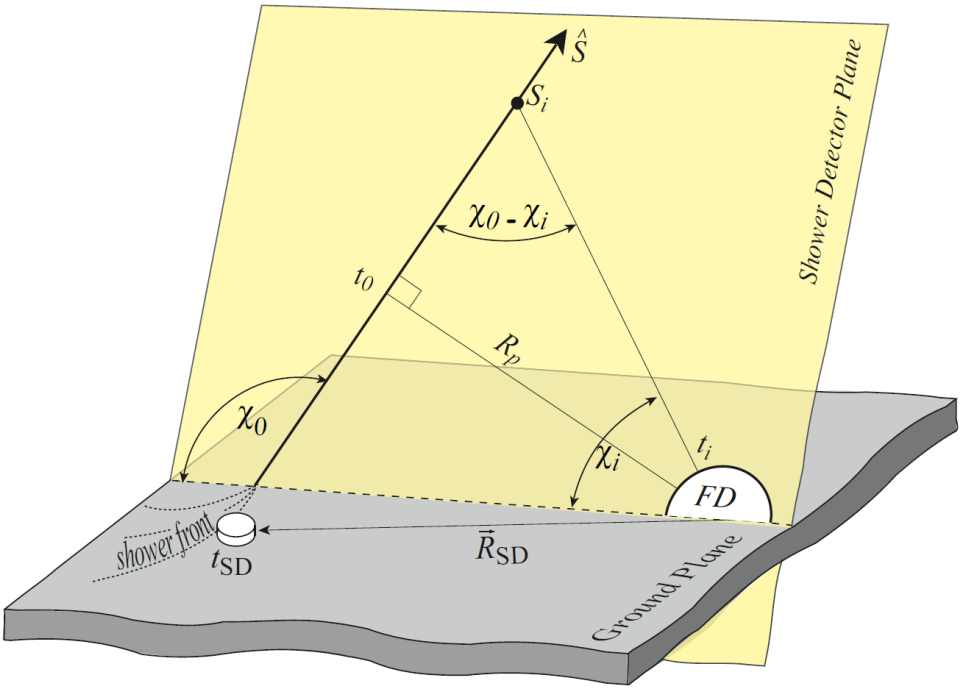

Figure 5.5: Illustration of the shower / detector geometry for the hybrid reconstruction method. Figure from [126].

hybrid event is shown in figure 5.6. The used SD station is marked by the small black square. The expected time from the SD station can be given as

$$t_{\mathrm{SD}}^{\mathrm{exp}} = t_0 - \frac{\vec{R}_{\mathrm{SD}} \cdot \hat{S}}{c}, \tag{5.7}$$

with $\vec{R}_{\mathrm{SD}}$ as the vector pointing from the telescope to the hottest SD station and $\hat{S}$ the unit vector of the shower axis pointing towards the origin of the coordinate system and t_0 again the reference time. A schematic overview of the geometry is given in figure 5.5. For this overview, the shower front is assumed to be planar, whereas the real shower front is curved. This is considered in the geometry reconstruction implemented in the Offline software. This additional timing information is then used as additional data point for the timing fit (see figure 5.7). The data point of the SD station is marked by the small black square. The data point of the SD station is somewhat distanced from the FD data points, leading to a larger leverage arm for the timing fit, which improves the resolution of the axis fit, leading to smaller angular uncertainties.

The χ^2 function that is minimized for the hybrid geometry reconstruction is then a combination of the SD and FD parts (compare to equation. 5.3):

$$\chi^2_{\mathrm{hyb}} = \underbrace{\sum_i \frac{(t_i - t_i^{\mathrm{exp}})^2}{(t_i^{\mathrm{err}})^2}}_{\text{FD part}} + \underbrace{\frac{(t_{\mathrm{SD}} - t_{\mathrm{SD}}^{\mathrm{exp}})^2}{(t_{\mathrm{SD}}^{\mathrm{err}})^2}}_{\text{SD part}}, \tag{5.8}$$

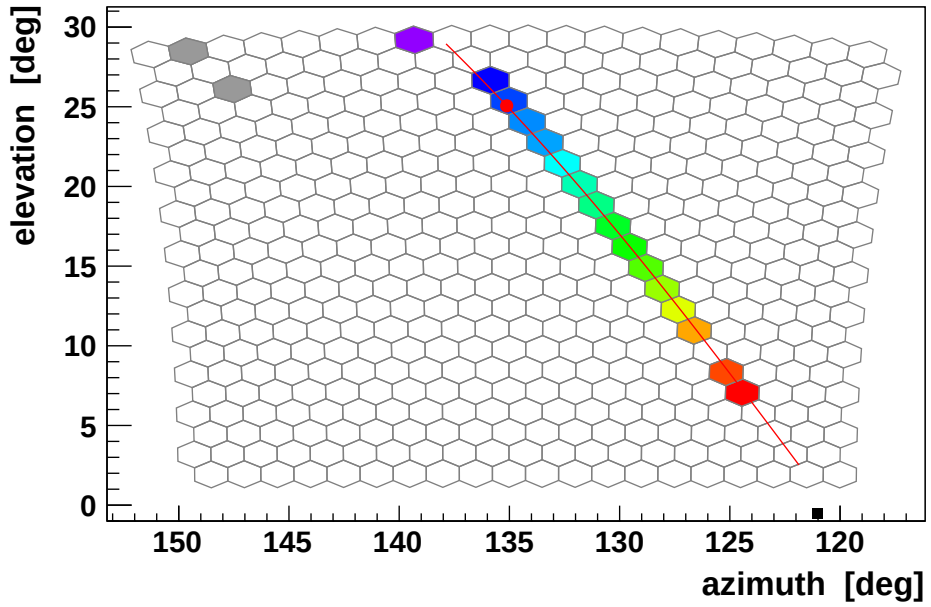

Figure 5.6: This figure shows the pixel pattern of a hybrid event. The used SD station is marked by the small black square (located on the horizontal axis).

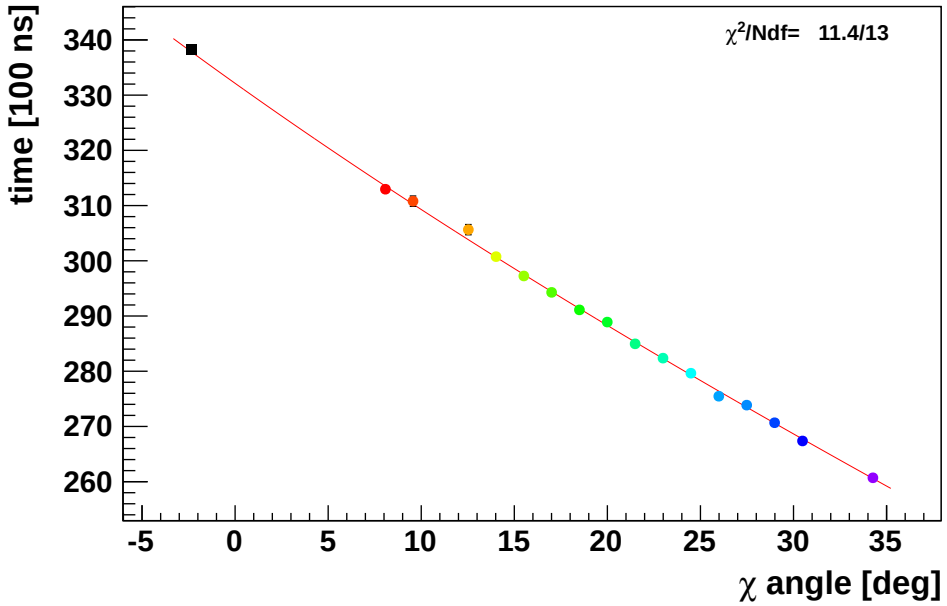

Figure 5.7: This figure shows the time - angle correlation after fitting for an example hybrid event. The used SD station is marked by the small black square. Note the distance in time and angles between the SD data point and the FD data points.

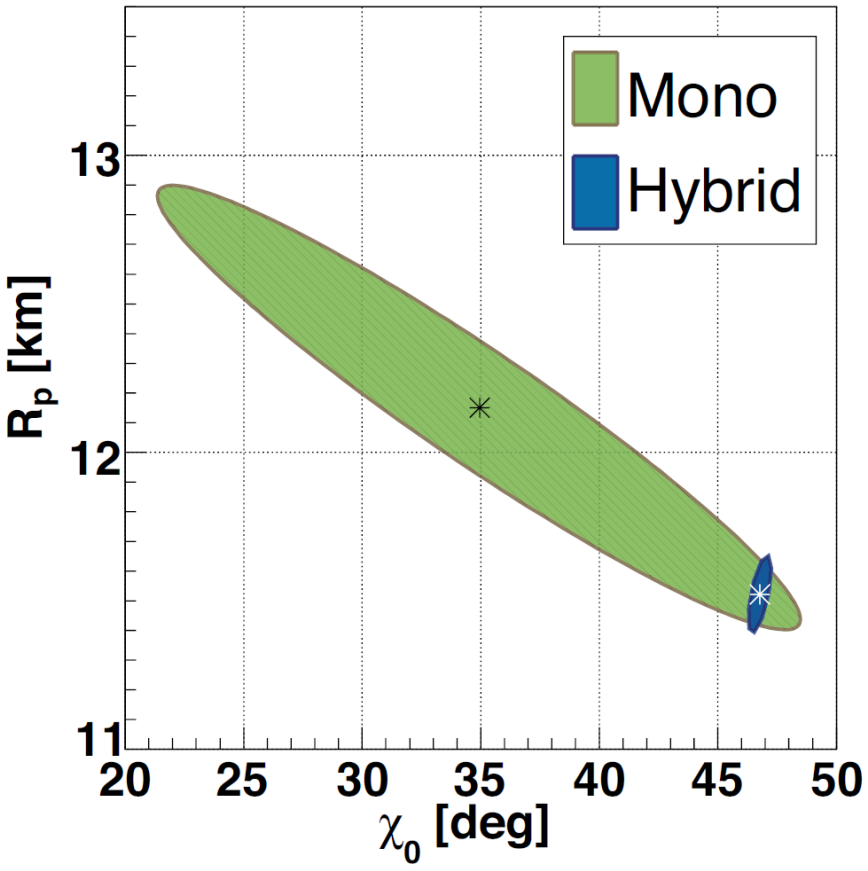

Figure 5.8: Comparison of reconstructed values for R_p and χ_0 for one example event. The solution of the FD mono method is shown with the black star, its 1 σ contour given in green. The solution of the hybrid method is given with the white star, its 1 σ contour given in blue. Figure from [126][127].

with t_{SD} is the measured and t_{SD}^{exp} the expected time information from the used SD station. t_{SD}^{err} is the expected uncertainty for t_{SD} and t_{SD}^{exp}. With this method, the resulting resolution for the shower axis can be better than 0.5°. The advantage of the hybrid reconstruction method versus the FD mono reconstruction method can be seen, for example in figure 5.8. For one typical shower the reconstructed values used in the axis reconstruction, R_p (the perpendicular distance detector - shower axis) and χ_0 (the angle of the shower axis inside the SDP) are shown. The fit result of the FD mono reconstruction is given with the black star with its 1 σ uncertainty in green. The white star shows the solution for the hybrid reconstruction with its 1 σ uncertainty in blue. One can see that the large uncertainty and the correlation of the two parameters for the FD mono reconstruction method is reduced significantly by the use of the additional timing information of one SD station in the hybrid reconstruction.

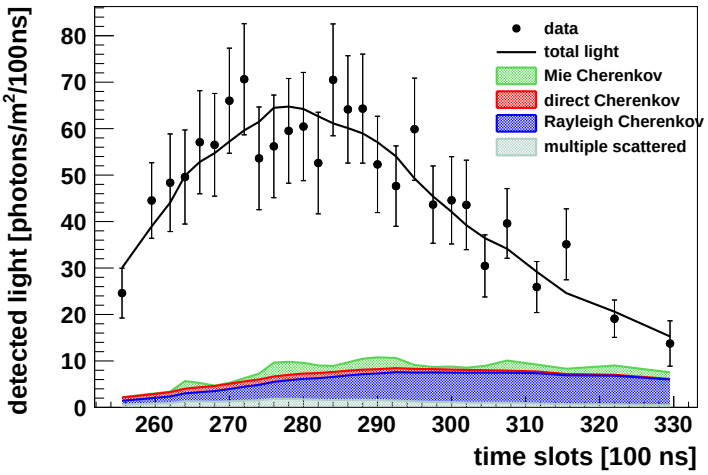

Figure 5.9: An example of a light-at-aperture measurement (dots) and the reconstructed light sources (shaded areas)

5.2.2 Reconstruction of the longitudinal energy deposit profile

With the geometry reconstruction completed, the energy deposit of the shower has to be reconstructed. To do that, the light profile at the aperture, that is the number of photons per time unit reaching the telescope has to be converted to the energy deposit at the shower axis as a function of atmospheric depth along the shower axis. With the shower geometry known, the light attenuation between the shower and the telescope aperture can be calculated for the different segments of the shower. Two main processes for the light scattering exist: Molecular scattering (Rayleigh scattering) and aerosol scattering (Mie scattering). For a detailed description of light scattering processes see [110]. Typical values for the light attenuation are found to be between 15% and 85%, depending on the shower geometry.

The light detected at the aperture can have several sources: The fluorescence light itself, direct and scattered Cherenkov light and multiple scattered light. Multiple scattered light was scattered by both processes, molecular and aerosol scattering. These different light sources have to be disentangled[84]. This allows the calculation of the energy deposit profile from the detected light profile. An example of a measured light profile together with the reconstructed light sources can be found in figure 5.9 and the reconstructed energy deposit profile in figure 5.10.

To this energy deposit profile, a Gaisser-Hillas function is fitted. The total shower energy is then calculated by integrating the Gaisser-Hillas function to get the calorimetric energy and correcting for the "invisible energy" of the shower. The invisible energy of the air shower is that part of the energy of an air shower that is converted into neutrinos in the cascade of secondary particles. Secondary neutrinos travel through the atmosphere without interacting with it. The energy carried by secondary neutrinos is then lost for the measurement by fluorescence detectors. The fraction of invisible energy of an air shower was studied with simulations, and a

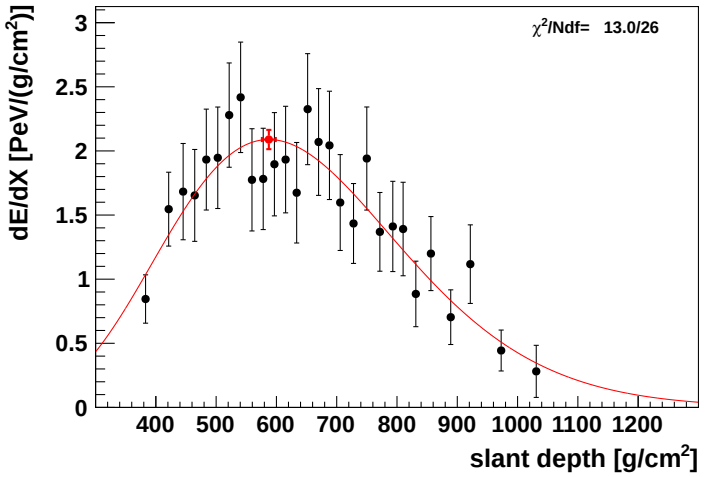

Figure 5.10: Reconstructed example energy deposit profile for a shower with an energy of around 10^{18} eV. The shower is the same as in figure 5.9. The line shows the Gaisser-Hillas fit of the profile.

parametrization of its energy dependence is used in the reconstruction software. The slant depth of the shower maximum $X_{\max}$ is also gained from the fit of the Gaisser-Hillas function.

5.3 Offline Software Reconstruction Framework

The Offline framework [128] is a software framework by the Pierre Auger collaboration for the reconstruction and simulation of its air shower data. It uses a modular design to describe the detector down to the smallest part, the atmosphere above the detector and the air shower itself. The description of physical processes and mathematical tools are implemented in the framework. The Offline version used for the reconstruction of the air shower data used in this study was v2r7p4.

The Offline modules used for the reconstruction of Coihueco and HEAT data and their function, important settings or settings that differ from the standard settings are described[2]. The necessary steps and the used modules are listed in the order in which they are used in the reconstruction sequence.

For the reconstruction of HEAT data, the first step is the preparation of the raw data. Data taking operations for the FD detector are organized into runs: Every eye of the FD that is actively taking data with all or part of its telescopes generates a run file which contains the measured raw data of the whole eye. For every run the general detector configuration of the eye is static, that means the number of active telescopes in the DAQ per eye is constant for every runfile. If the number of active telescopes has to be changed (for example because the moon enters the field of view

[2]The two character abbreviations in the name of the modules (for example “OG” or “WG”) are used to distinguish between different implementations or versions of modules that can perform the same or equivalent tasks.

of a single telescope), the actual run is stopped, the number of telescopes in DAQ is changed and a new run is started. The first step for the data reconstruction is the removal of run files from the data set where the detector was not in a desired state. This analysis uses a static detector description, with all Coihueco telescopes active and all HEAT telescopes active and in the upward position. This detector configuration is called COHE. Run files that don't match these criteria are removed. Also, run files from the three other standard FD eyes are not used. For the SD detector the raw data is also divided into run files. These run files are produced for a time span of 24 hours and contain data with a changing detector configuration (because the number of active SD station changes).

The next step is the merging of the suitable Coihueco -, HEAT- and SD-runfiles into hybrid raw data files that are used for the reconstruction. This merging process is done with the program simpleMergerKG. The events for the two eyes and the SD data are ordered chronologically and if two or three events from the different detectors were measured within a certain time frame they are combined to a single event. A preselection of the events is possible at this time: It is possible to discard events that have no coincident FD and SD part, or change the number of eyes or SD stations that have to be in a certain event to be accepted. Also the maximum allowed time difference for events to be considered coincident can be changed. For this specific analysis, the settings for the preselection were, that only coincident hybrid events with at least one eye and one SD station with a maximum timing difference between events of 200 μs were allowed. These settings were chosen, because only hybrid events will be used later for the analysis, so the reconstruction of FD or SD only events is unnecessary. The time difference of 200 μs was chosen rather large, but wrongly merged events will be removed by the reconstruction later, when the different parts of the event do not match. Another important feature is the rate limit bias reduction for HEAT. To reduce the bias against HEAT, that is introduced by the rate limiting for HEAT T3 events on hardware level, Coihueco events have to be vetoed with the same procedure that is implemented in the hardware, when their rate is too high (see chapter 4.4.1.2). This is also done by the simpleMerger. The output of the simpleMerger are ROOT[129] file containers which span a maximum time of 24 hours. These files are then usable as input for an Offline reconstruction.

The first module in the reconstruction module chain is the **EventFileReaderOG**. This module reads the events from raw data or the output of the detector simulation. The use of several file types is possible, for example the file types for raw SD data, raw FD data, raw hybrid data or the Offline file type used to store the output of the Offline detector simulation.

The module **EventCheckerOG** checks for possible damaged or incomplete files, for example events with a missing time information or a missing detector description. Events which could become problematic in the further reconstruction chain are skipped. This module is used only as a precaution, because the files generated by the simpleMerger or the simulation (see chapter 6.4) should be without errors. No event in this analysis triggered this module.

The **FdCalibratorOG** converts the raw FADC traces that were recorded by the telescopes (or the simulated ones) into photon counts versus time. For this, the calibration constant, that gives the number of photons per ADC count for the pixel (or the global value per telescope, in case the pixel is part of a HEAT telescope) is used.

The **FdEyeMergerKG** module is responsible for the merging of the telescope information from the physical eyes into those of the virtual eyes, in this case the virtual eye COHE, consisting of the six telescopes of the eye Coihueco and the three HEAT telescopes in upward position. The information from the physical eyes is not changed in this process. The concept of virtual eyes is described in chapter 5.4.1.

After that, the **FdPulseFinderOG** searches for pulses in the photon-number versus time traces for every pixel, to find the times when the specific pixel measured the maximum signal from the air shower. This time is equivalent to the time when the air shower (or a part of the air shower) crossed the field of view of this specific pixel. The shower front of an air shower is extended spatially (and so also in time), leading to the possibility to find several pulses for a specific pixel at different times.

The SDP of the shower is then calculated by the module **FdSDPFinderOG**. For that a plane is fitted in which all pixels with a pulse are lying.

From the timing information of the pixels, the module **FdAxisFinderOG** finds a preliminary shower axis, that lies in the SDP.

In the case of a hybrid event, the module **HybridGeometryFinderOG** calculates a shower axis from the timing information of the FD pixels and the timing information from one SD station. Out of the set of SD stations with a signal in the event normally the station with the highest signal is selected. The HybridGeometryFinderOG works only on physical eyes.

For a reconstruction of data from a virtual eye, the **HybridGeometryFinderWG** is used. It is a modification of the OG module and incorporates techniques used in older stereo reconstruction modules. It was developed specifically for the COHE reconstruction, but is able to work on arbitrary virtual eyes. Data from physical eyes is ignored by this module. To use data that was detected with telescopes at different sites, the calculation is done in shower core dependent coordinates and angles, after transformation of the telescope dependent data. This module was developed by D. Kruppke-Hansen from the Wuppertal group. For more information on this module see [114].

From the intensity and time distribution of the recorded signal, the **FdApertureLightKG** module reconstructs the light flux at the telescope aperture.

Together with the geometry information of the previous modules and the light flux at the aperture, the module **FdEnergyDepositFinderKG** calculates the energy deposit profile of the air shower, and by fitting a Gaisser-Hillas profile to the energy deposit profile, the shower maximum and the total energy deposit of the shower in the atmosphere are determined. With this information, the energy of the primary particle is calculated.

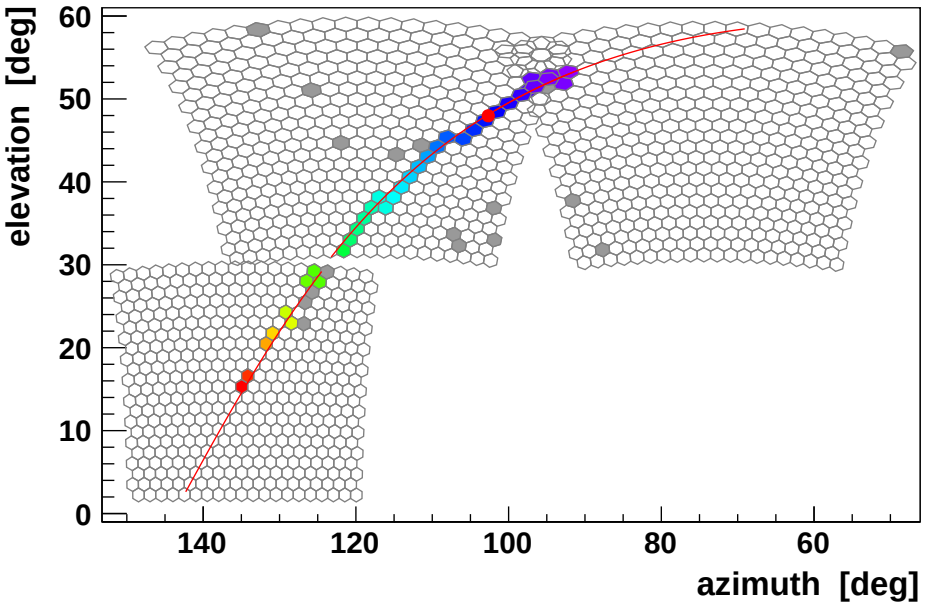

Figure 5.11: This figure shows the pixel pattern of a reconstructed COHE event with an energy of around 10^{17} eV which was recorded in 2 HEAT mirrors and one Coihueco mirror. Without HEAT, this event would not have been reconstructable. Notice the gaps between the telescope field of views.

The last module in the reconstruction module chain is the **RecDataWriterNG**. This module writes all information from the previous modules into the output files, again a ROOT file container. These so called ADST files (Advanced Data Summary Tree[130]) can be viewed by the EventBrowser program of the ADST toolkit (a part of the Offline framework) or used for further analyses.

The pixel pattern for a reconstructed example COHE event can be found in figure 5.11. The event had an energy of around 10^{17} eV. The data was recorded in two HEAT and one Coihueco telescope.

5.4 Modifications for HEAT Reconstruction

The hardware of the HEAT telescopes differs in some aspects to that from the standard FD telescopes because of updates that were made. In addition the possibility to operate the HEAT telescopes with two different pointings and the need for a combined reconstruction of Coihueco and HEAT have made modifications to the standard reconstructions necessary.

5.4.1 Physical and virtual eyes in the detector description

The reconstruction and simulation software for the standard FD uses the “eye” as a unit for the description of the detector. One eye consists of the six telescopes located in one FD building. For a combined reconstruction of HEAT and standard FD data (for example from the eye Coihueco) this description is not usable. The

new construct of a virtual eye is introduced for such cases. The reconstruction in this case is not eye-based any more but telescope-based. A virtual eye is a container that is able to hold a number of physical telescopes from different physical eyes. The virtual eye COHE contains all six telescopes of the physical eye Coihueco and all three telescopes of the physical eye HEAT in the upward position. For more details see the GAP note "A first look at HEAT data"[114].

5.4.2 Cross Calibration for HEAT

The data from a drum calibration campaign of the HEAT telescopes is currently under study and will be ready in 2013. This means that no calibration constants for the PMTs of the three HEAT telescopes is available yet. For a first preliminary telescope calibration, a so called cross calibration was used[114]. A first step for the cross calibration is the so called "flat-fielding", a process that is also the first step for a drum calibration. While the camera is illuminated with the drum light source, the differences in PMT-gain over the whole camera are minimized by changing the gain of PMTs. This can be done without knowledge of the absolute calibration constant. Afterwards, a global calibration constant (as opposed to a calibration constant for each single PMT) was assigned to each HEAT telescope. Events that were measured in downward mode were reconstructed and compared to the same events that were measured with Coihueco telescopes. Afterwards, the global HEAT calibration constants were changed and the process repeated until the differences in reconstructed energies between Coihueco and HEAT were minimal. The same procedure was done with simulated events as a cross-check.

Because of the limited number of nights when HEAT was operated in downward mode, the number of events for this study is relatively small, from 50 to around 100 events per single telescope. The resulting calibration constants were used for this analysis. A possible change of the calibration constants by tilting the telescopes was studied. A change of the orientation of the PMTs inside the Earth's magnetic field might lead to a different signal amplification in the PMTs and so to a different calibration constant. The measured effect on the calibration constant was found to be negligibly small with a maximum of 2 percent[131]. The drum calibration for the HEAT telescopes was also done in the downward position. The possibility to perform a drum calibration in the upward position is studied.

Figure 5.12 shows the relative energy difference between the reconstructed Coihueco energy and the reconstructed HEAT energy for downward data in black. On the left side the distribution before the correction of the calibration constant is shown. The distribution after the correction is shown on the right side. The Monte-Carlo simulation uses the same calibration constants for simulation and reconstruction, so the simulated distribution is already centered around zero before the constants are corrected. After correction, the two distributions match very well.

5.4.3 HEAT telescope pointing

The absolute pointings of the HEAT telescopes were calculated by comparing the reconstructed HEAT shower geometries with Coihueco geometries from showers that

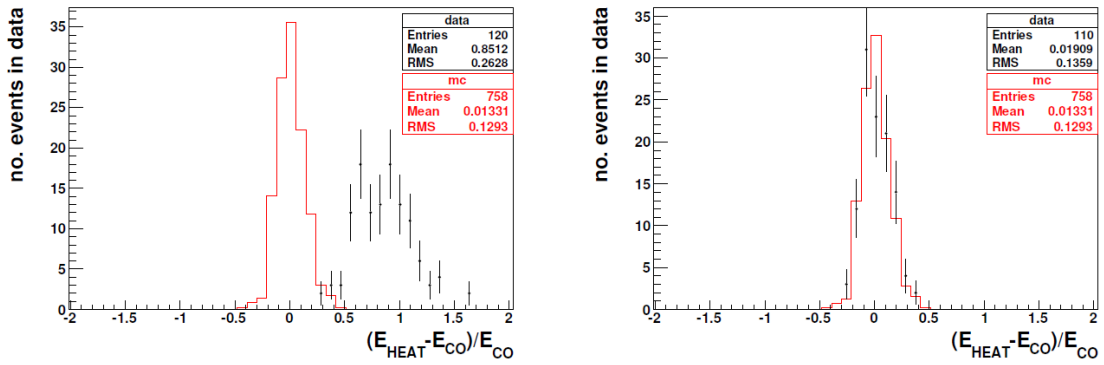

Figure 5.12: Cross calibration of HEAT and Coihueco. The difference in energy for downward events seen simultaneously in HEAT and Coihueco is shown in black. The red curve shows the difference in energies for simulated events. On the left, the distribution before the correction is shown, the right plot shows the distribution after correction. For more details see chapter 5.4.2. Figure from [114]

were detected with both eyes. This analysis uses the pointings for the HEAT and Coihueco telescopes from the internal note GAP-2011-123 [132] for the simulation and reconstruction of air shower data.

5.5 Summary

This chapter described the data reconstruction methods for the Pierre Auger Observatory and in detail the specific reconstruction method used for this analysis was described. The production of a large database of simulated showers is presented in the next chapter. For simulated showers, the same reconstruction as described in this chapter is used after the air shower simulation and the simulation of the atmosphere and the detector response.

6. Air Shower Simulation

The production of a library of simulated air showers is described in this chapter. The simulation of air showers is needed to calculate the detector response of the HEAT telescopes (or of the combined detector COHE) to air showers instigated by cosmic rays in this new energy range for the Pierre Auger Observatory. The shower library is used to calculate simulation and reconstruction efficiencies, the effective area of the detector and in the end a large fraction of the several ingredients needed for the calculation of the exposure of the detector.

The simulation of air showers is separated into three parts: First the simulation of shower profiles with Conex, then the simulation of the light produced by the air shower together with the propagation through the atmosphere, optics and electronics of the fluorescence detector and finally the response of the surface detector to the secondary particles of the air shower with the Offline software framework[128]. The last part consists of the reconstruction of the simulated detector data with the same shower reconstruction which is used for real data (see chapter 5). This chapter describes the used software and their settings and the contents of the simulation library.

6.1 The air shower simulation software Conex

Conex[133] is a fast hybrid simulation software for cosmic ray air showers. Hybrid in this case means, that for the first interactions of an air shower cascade, Monte Carlo simulations are used. When the energy of the secondary particles is relatively low after several interactions (O(10)), the further development of the air shower is calculated by numerically solving cascade equations. This leads to a considerable speed-up in computation times compared to full Monte Carlo simulations like CORSIKA[72]. On a modern XEON processor, the simulation of one air shower with an energy of 10^{18} eV takes around 60 seconds with Conex and up to several days for a full simulation with CORSIKA. To reduce the computation times, CORSIKA uses a so called *thin sampling* or *thinning* technique[134]. Thin sampling randomly selects secondary particles from the air shower as representative particles for whole classes of secondary particles and discards the rest.

The interactions of these representative particles are further calculated with a higher weight in the following Monte Carlo simulation steps. This method reduces the computation time to several hours but introduces the possibility of statistical fluctuations, which is increasing with increasing levels of thin sampling. For the simulation

of hybrid events, where only the longitudinal profile of air showers is of importance, and not the actual distribution of secondary particles on the ground, Conex is a software which is capable of generating a large number of air showers which cover large phase-spaces in energies and angles and primaries in a reasonable time. The output of the used Conex version 2r2.3i are ROOT[129] container files that are easy to handle for further processing.

6.2 Hadronic Interaction Models

It is possible to use different high energy interaction models when simulating air showers with Conex. For this study, three different models were used: Epos 1.99[135], Sibyll 2.1 [71][136] and QGSJET-II-03 [137][138].
These models use parameterizations or look up tables for high energy hadronic interactions. They are based on datasets of lower energy reactions, measured at particle colliders. The extrapolation to the high energies that occur in air shower reactions is different for the models. This leads to differences between the simulation results, if showers with the same starting parameters (i.e. particle type, energy, zenith and azimuth angle) are simulated. These so called model uncertainties differ from the shower-to-shower fluctuations, occurring when a shower with the same starting parameters and the same model is simulated repeatedly.

6.3 Simulation Input

In a first step, a total 720,000 showers were simulated with Conex and Offline. For every discrete energy bin in $\lg \frac{E}{\mathrm{eV}} = (17.25, 17.50, 17.75, 18.00, 18.25, 18.50)$ 10,000 showers were simulated for every combination of primary type (proton or iron) and hadronic interaction model (Epos 1.99, Sibyll 2.1, QGSJET-II). For the low energy bins $\lg \frac{E}{\mathrm{eV}} = 16.50, 16.75, 17.00$ the number of Conex showers was doubled to 20,000 per combination of primary particle and interaction model because of the low reconstruction efficiencies at these energies. The showers were simulated in batches of 1000 to 2500 showers per file, depending on shower energy, to allow the parallel simulation of the whole dataset.
For the exposure calculation, the number of simulated showers was later increased, to get a stable result, especially for the lowest energies, see chapter 8.2.2. In total, 2,343,000 Conex showers were generated and used as input for the shower simulation.

The simulations were performed on the cluster of the Aachen physics institutes and on the HPC cluster of the RWTH Aachen University[139].

The azimuth angle distribution was chosen as flat between $\phi_{\mathrm{min}} = 0°$ and $\phi_{\mathrm{max}} = 360°$. The zenith angle distribution was chosen to represent the isotropic influx of cosmic rays on a flat surface between $\theta_{\mathrm{min}} = 0°$ and $\theta_{\mathrm{max}} = 65\ °$ following the distribution of $\frac{\mathrm{dN}}{\mathrm{d}\cos(\theta)} \sim \cos(\theta)$. In Conex only the shower energy, the type of primary and the azimuth and zenith angles are defined. The distribution of azimuth and zenith angles for one example file of Conex showers with an energy of $10^{16.75}\,\mathrm{eV}$ containing 2500 proton events simulated with QGSJET-II is shown in figure 6.1.

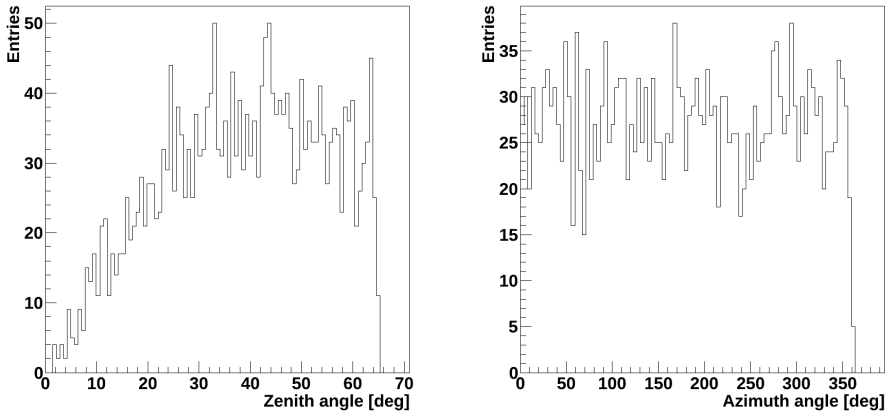

(a) (b)

Figure 6.1: Zenith and azimuth angle distributions for a subset of 2500 Conex showers, simulated with QGSJET-II, proton primaries and an energy of $10^{16.75}$eV. 6.1 (a) shows the zenith angle distribution and 6.1 (b) shows the azimuth angle distribution.

All 720,000 Conex showers were used as input for the Offline detector simulation. The output from the detector simulation was then used as input for the same shower reconstruction that was used for the real data (see chapter 5). The foot points of the showers, or shower cores, that are the points where the shower axis intersects the Earth's surface, were randomly distributed in an area that is overlooked by the Coihueco field of view. The footprint of the Coihueco field of view was chosen, because the footprint of the HEAT field of view is fully enclosed by that of Coihueco. The azimuthal slice was centered on the border between Coihueco telescope 3 and Coihueco telescope 4 with a width of 180° in azimuth. The minimum distance for shower cores to the detector was set to 1000 meters, because there are no SD stations closer to the detector than that and the chance for a hybrid trigger in a SD station is negligible. The maximum allowed distance for a shower core to the detector is chosen as 1.2 times the maximum range found in data when using a relaxed cut set. The distances range from 5400 meters for the lowest simulated energies ($10^{16.5}$ eV) to 35,400 meters for the highest simulated energies of $10^{18.5}$ eV.

The distribution of eye - shower core distances for real data with just basic cuts can be found in figure 6.2. The maximum distance between the detector and the shower core in real data is always smaller than the value used for the simulation and no hybrid showers cores are closer than 1300 meters to the detector. Figure 6.3 shows the distribution of shower cores for hybrid HEAT data after all quality cuts (see chapter 7) over the hole energy range used in the analysis. The figure shows the number of shower cores per km^2 normalized to the total number of showers. As an overlay, the position of SD detector stations is given with the black dots. The position of HEAT and Coihueco is given by the pink dot. A concentration of events relatively close to HEAT on the western edge of the infill is clearly visible. The absence of shower cores closer than 1000 meters to HEAT and the maximum

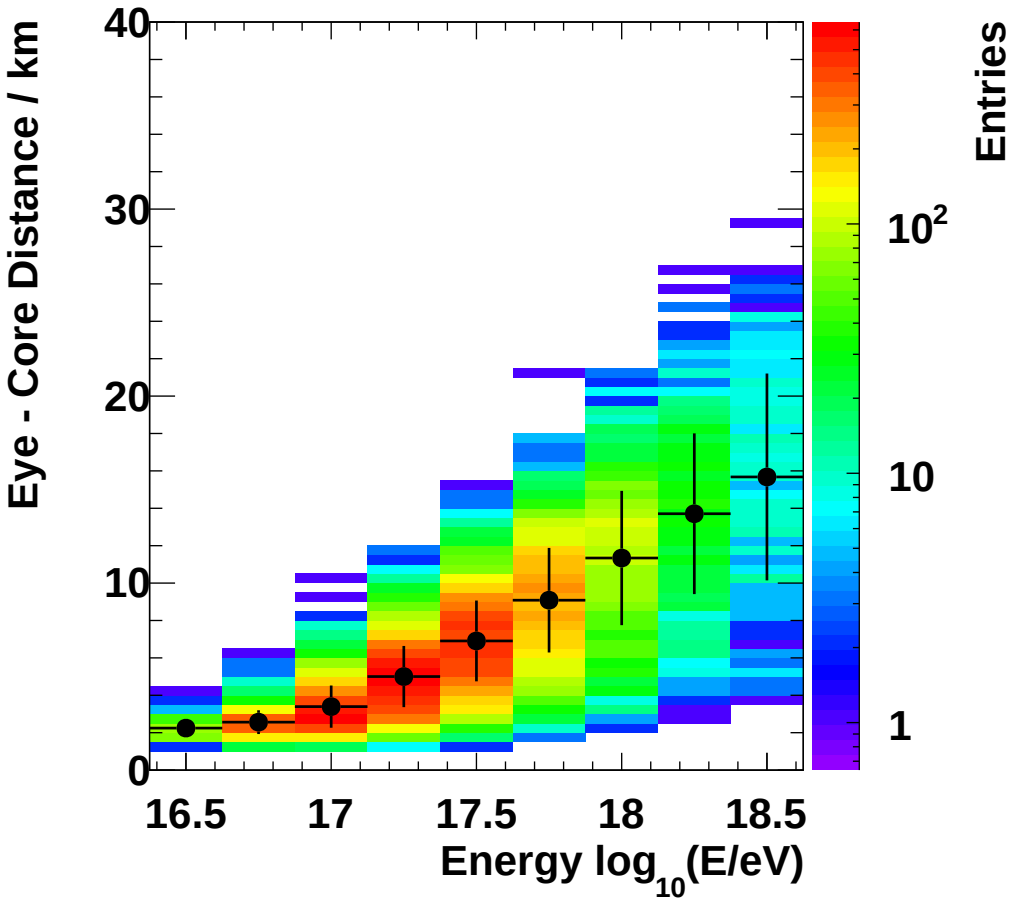

Figure 6.2: This figure shows the distributions of distances from the detector to the shower core in dependence of the shower energy for COHE data. The black dots give the mean of the distribution per energy bin. The horizontal error bars give the bin width and the vertical error bars give the standard deviation. Only basic quality cuts were used.

distance of cores is visible. Easting and Northing are Cartesian coordinates for points on the Earth's surface in a coordinate system centered roughly on the center of the SD array.[1]

6.4 The Offline Simulation Software Framework

The Offline framework is a software framework by the Pierre Auger collaboration for the reconstruction and simulation of its air shower data. It uses a modular design to describe the detector down to the smallest part, the atmosphere above the detector and the air shower itself. The description of physical processes and mathematical tools are implemented in the framework. The Offline version used for the simulation was v2r7p4.

[1]The used coordinate system is the so called Universal Transversal Mercator (UTM) coordinate system. For more information see http://earth-info.nga.mil/GandG/publications/tm8358.1/toc.html.

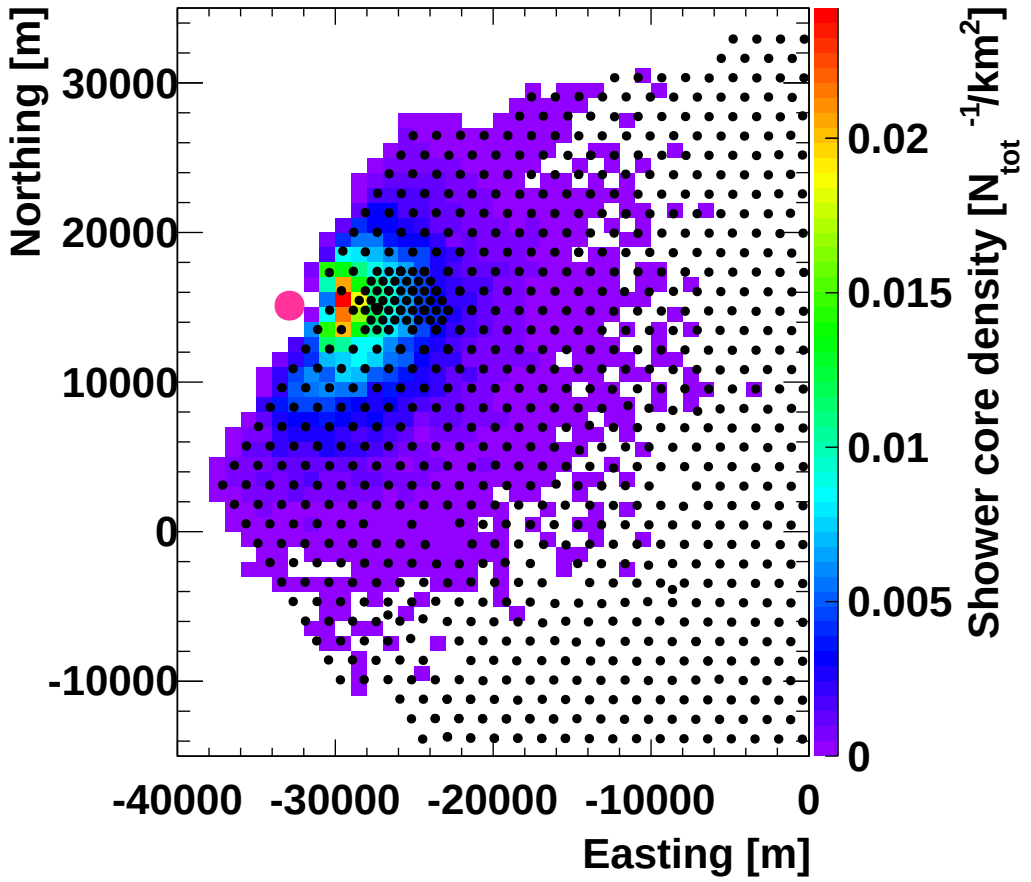

Figure 6.3: This figure shows the distributions of shower cores in the SD array. The number of shower cores per km^2 normalized to the total number of showers is shown as colored bins. The overlay of black dots marks the positions of SD detector stations. The single pink dot marks the position of HEAT and Coihueco.

The Offline modules used for the shower simulation are described, together with a short explanation of their function and important settings or differences to the standard settings. The modules are presented in the order in which they are used in the simulation sequence. A more detailed description of the modules and the used techniques for the simulation can be found in the internal note GAP 2008-014 [140] or in the updated version of that note that is part of every Offline installation.

For each event in the Conex files, the module sequence is run trough once, until there is no new event in the Conex file. The simulation-module chain starts with the **EventFileReader**. This module is able to read in the output files of several air shower simulation software packages (Corsika, Aires, Seneca and Conex) and several Auger specific file types, be it SD raw data, FD raw data, hybrid raw data and the file type that is generated as output of an Offline detector simulation. In this instance it reads the single air showers from the Conex files.

The **MCShowerChecker** checks the Monte Carlo profile for (non-physical) negative entries in the electron number profile end rejects the event if these occur. This was never the case for all simulations.

The event time and the shower cores are generated in the module **EventGenerator**. The used values for the shower foot points can be found in chapter 6.3.

Following that, the module **FdSimEventChecker** sets the status of all FD detector components. For this simulation, all Coihueco telescopes and all HEAT telescopes are set to be active in the DAQ.

The simulation of the light generation of the air shower, both fluorescence and Cherenkov light, is done by the module **ShowerLightSimulator**. The number of fluorescence photons is calculated from the energy deposit $\frac{\mathrm{d}E}{\mathrm{d}X}$. The number of emitted Cherenkov photons is calculated from the number of electrons and positrons above the Cherenkov energy.

The light propagation in the atmosphere is handled by the module **LightAtDiaphragmSimulator**. It calculates which part of the simulated air shower lies in the field of view of a telescope. With this information, the number of direct fluorescence and Cherenkov photons and the number of Mie and Rayleigh scattered Cherenkov photons at the telescope diaphragm is calculated.

In the module **ShowerPhotonGenerator** the up to now one-dimensional treatment of the shower is corrected to include the lateral shower structure. This is done by expanding the shower structure with the lateral distribution of the energy deposit $\frac{\mathrm{d}E}{\mathrm{d}X}$. The lateral distribution is generated from the lateral structure of the light at the aperture (the arrival time distribution and angular distribution of the photons at the aperture). The resulting lateral structure is then similar to an NKG function (see equation 3.5).

The next module in the chain, **TelescopeSimulatorKG** is used for the ray tracing of photons, which were generated at the telescope diaphragm by the previously mentioned modules, in the telescope optics. For that, reflectivity and transmission properties of all materials inside the telescope are considered properly. The module generates the photon signal for any photon that enters the sensitive area of a PMT.

The air shower is not the only light source from which photons can reach the PMTs inside the telescopes. The main sources of background light are UV-bright single stars, the moon, the milky way or the atmosphere itself. For the time-scale of an FD event, the background light shows nearly no time variation. The module **FdBackgroundSimulator** calculates the mean number of background photons arriving at the photocathode of each PMT. The background photons can be simulated in three different ways: a lookup table with measured background light levels that exist for some telescopes, information from the FD monitoring, which is measuring the background light for every PMT, or a zenith angle dependent parametrization. For the HEAT telescopes, only the third method is applicable, because there exists no lookup table for these telescopes and the second method needs drum calibrated telescopes to work. Point sources of background light (like stars) are not considered for

the parametric simulation. For the time scales of air showers, the background light generated by stars is constant and leads only to a higher signal baseline for a single pixel. For a RealMC simulation, the simulated background light level is generated from the measured background light level of the FD monitoring and contains the effect of single stars (see [141],[142] and [143]). A RealMC simulation is a time dependent simulation which modifies the detector status depending on the monitoring data.

The **FdElectronicsSimulator** is the module that simulates the electronics and sampling effects of the telescope. The output of this module are simulated measured ADC traces of the PMT signals.

These ADC traces are used as input in the module **FdTriggerSimulator**, where the three telescope based trigger levels and the eye based trigger level are simulated (for a detailed description of the FD trigger levels see chapter 4.2.1).

The module **SdSimpleSim** handles the SD part of the simulation, when Conex showers are used as simulation input for a hybrid simulation. Conex showers are only one dimensional objects which contain the longitudinal profile of the air shower, their lateral extension for the FD part of the simulation is handled by the ShowerPhotonGenerator module. The same method is used for Corsika showers. Something similar has to be done for the SD simulation part. The SdSimpleSim does that combined with a simulation of the response of the SD stations to the expanded lateral distribution together with a simulation of the trigger response of the single SD stations. (For more information on the module and the lateral expansion see the internal GAP note 2008-061[144] and sources therein, i.e. [145], [146], [86], [147], [148], [149] and [150].) For the simulation of the whole SD different specialized modules exist.

The **CentralTriggerSimulator** is an implementation of the CDAS trigger logic and generates the response of the CDAS system to the FD and SD triggers.

Together with the **CentralTriggerEventBuilder** module a hybrid event is build from coincident SD and FD triggers.

The **EventBuilder** stores the information from all previous modules in the correct data types to generate a valid Offline event.

The last module in the simulation chain, the **EventFileExporter** writes all information of the simulated events from the other modules into a file that is then used as the input for the shower reconstruction. The file type itself is again a root file[129] container. For bookkeeping purposes, untriggered shower profiles are also kept in the file.

The reconstruction of these simulated events is similar to the reconstruction of real data and was already explained in chapter 5.

6.5 Summary

This chapter described the air shower simulations and the use of hadronic interaction models. The simulation software chain used in this analysis was given in detail. The

resulting simulated air showers are used for the exposure calculation needed for the spectrum calculation. Before the simulated and reconstructed air showers can be analyzed, low quality events that could taint the analysis have to be removed. This is done by using a set of cuts on the simulated data and on the real data to select only high quality events. The data selection process is described in the next chapter. With this reduced data set of high quality events, both measured and simulated, the exposure and finally the energy spectrum is calculated.

7. Data Selection

To guarantee that the analysis is not tainted by events with a low quality, several selection criteria that allow only high quality events to pass have to be used. These cuts are used for the real data and for the simulated data alike.

One important tool for the rejection of low quality events is the quality database of the Pierre Auger Observatory. It contains information on the state of the atmosphere, for example the occurrence of clouds and the abundance of light scattering aerosols. Unfortunately, the use of this tool was not possible for this analysis: The quality database is only generated when the whole information from all different monitoring sources is completely analyzed and available. Important parts of monitoring database depend on the measurement with drum calibrated telescopes (for example aerosol information). With these information missing, there exists no quality database for HEAT. The quality of the data resulting from the possible cut set was studied and no problematic events or large biases were found.

The goal is to use only high quality events from times when all six Coihueco telescopes and all three HEAT telescopes were actively taking data and the three HEAT telescopes were in the upward position.

The used raw dataset consists of events taken with the fluorescence telescopes in the eyes Coihueco and HEAT of the Pierre Auger Observatory, detected from June 2010 to September 2011. June 2010 was chosen as starting point for the data taking period, because from this month onward the HEAT electronics (for example the rate limiting) was operated in its final state (see chapter 8.3). The end date of September 2011 is marked by the installation of additional SD stations close to HEAT (HEATLET, see chapter 4.4.3). With the integration of these stations into the DAQ, the detector response changes, especially for low energy showers. The use of a static detector description would not be possible, if the data taking period would be extended.

Data taking operations for the fluorescence detector of the Pierre Auger Observatory are organized in so called "runs". For each run the detector configuration is static, that means, that for each run, the number of active telescopes in the DAQ per eye is constant. If the number of active telescopes has to be changed, the run is stopped and a new run for the different configuration is started. For this analysis, only events from runs with the detector-configuration "all HEAT telescopes active in DAQ and tilted upwards and all Coihueco telescopes active in DAQ" are used. This is also considered for the uptime calculation (see chapter 8.3).

The event set is generated by merging the raw data information of the fluorescence eyes Coihueco and HEAT with the raw data from the surface detector with the simpleMerger. This merging process includes a correction for the effects of the rate limiting for HEAT. This correction leads to a reduction in event numbers between 25% and 30% (see chapter 8.3). The rate limiting is described in detail in chapter 4.4.1.2. The total dataset of measured events before cuts contains roughly 600,000 events and has a size of 60 GB.

The used cuts, an explanation of their function and the effect on the number of events is given in the following. The selection was done with the program selectEvents from the ADST-Analysis toolkit[151], that is part of the Offline framework.

7.1 Description of used cuts

The used cuts can be put roughly into three categories: General cuts, geometric cuts and profile cuts. The general cuts check for basic properties that the events must fulfill, for example that the event is a hybrid event. The geometric cuts work on the reconstructed shower geometry, for example that the zenith angle of the event has to be smaller than 60°. Profile cuts force the events to fulfill several requirements on the reconstructed shower profile, for example, that possible holes in the measured profile are not too large. In the listing, the name of the cut is given first, followed by a short description or explanation of the cut and its chosen value. The technical term of the cut used within the Offline framework is given as last item in parenthesis. If a cut has no effect on simulated data, a short explanation is given in the cut description. Where possible, the event distribution of the cut value is shown. Figures which show the distribution of specific values of the reconstructed events depict the distributions at this specific point in the cut process. Events that where discarded by cuts that where applied earlier are not shown in the distributions.

Basic cuts

Event has successful energy reconstruction The energy determination is the last step in the reconstruction of an air shower. Events that have a reconstructed energy were reconstructed successfully.(hasEnergy)

Event is a hybrid event This cut guarantees, that only hybrid events (events that use the timing information of one surface detector station in addition to the fluorescence light measurement) are in the data sample. The geometric errors for this type of events is much smaller than for FD only events (see chapter 5).(isHybrid)

Event was taken when all HEAT telescopes were in upward position This is a boolean cut, that can only be passed by events that were recorded when all HEAT telescopes were orientated in the upward position. This cut is needed, because the exposure calculation was only done for this specific detector configuration. In addition, times when the detector was not in this configuration were excluded from the uptime calculation (see chapter 8.3). This cut has no effect on simulated data, because the detector description for the simulation contains the HEAT telescopes only in the upward position.(heatOrientationUp)

Event contains no saturated pixels This cut removes events with saturated pixels. Pixels get saturated, when the recorded light signal is too high and larger than the dynamic range of the PMT. This can be the case for close high energy showers or showers that fall directly into the telescope.(skipSaturated)

Event contains no bad pixels This cut removes events that contain pixels that were flagged as non operative (marked black in the event picture). This cut has no effect on simulated data, because the detector description for the simulation does not contain defective pixels.(!badPixel 1)

Event was seen with virtual eye COHE The telescopes of the Pierre Auger Observatory are organized into eyes. The eyes one to four consist of the 24 standard telescopes, the HEAT telescopes form the fifth eye. The combined reconstruction of data from Coihueco (eye four) and HEAT (eye five) uses internally the eye number six. This cut is needed to remove the events that were reconstructed with the standard reconstruction separately for Coihueco and HEAT. This cut is passed by events that were reconstructed with the combined COHE-reconstruction and contains the events that were recorded in Coihueco and HEAT together and those events that only triggered Coihueco or HEAT (see chapter 5).(eyeCut 100000)

The uncertainty on the reconstructed energy of the event is smaller than 20% Measurement uncertainties and statistical uncertainties are propagated by the reconstruction algorithm to calculate uncertainties on reconstructed properties. This cut forces the events to have a relative energy uncertainty $\sigma(E)/E$ to be smaller than 20 %, with systematic uncertainties excluded. The distribution of relative energy errors is shown in figure 7.1.(energyError 0.2)

The maximum amount of direct Cherenkov light is 50% The removal of high Cherenkov-fraction events is needed, because the reconstruction software for air showers was developed to work with the fluorescence signal and uses the Cherenkov signal as additional information. This cut is only passed by events that have a reconstructed direct Cherenkov fraction in the total detected light signal of less than 50 %. This cut is needed to remove events that shine directly into the telescopes. That is possible because of the changed field of view of the HEAT telescopes compared to the standard telescopes. The effect of showers with the dominant light fraction of the shower signal not from fluorescence light, especially for HEAT, is studied, see for example[152]. The event distribution of direct Cherenkov fractions is shown in figure 7.2.(maxDirCFrac 50.)

Geometric cuts

The distance of the shower core to the next SD station must be smaller than 800 m The distance between surface detector stations is 1500 m. The reconstructed core of the accepted events must be closer to an surface detector station than 800 meters. This limits the active detector area to inside the surface detector array and removes events that fall outside this area. For the distribution of shower core - SD station distances see figure 7.3. (maxCoreTankDist 800.)

The zenith angle has to be smaller than 60° Only events with a reconstructed zenith angle smaller than 60° are accepted. Since the response of the surface detector

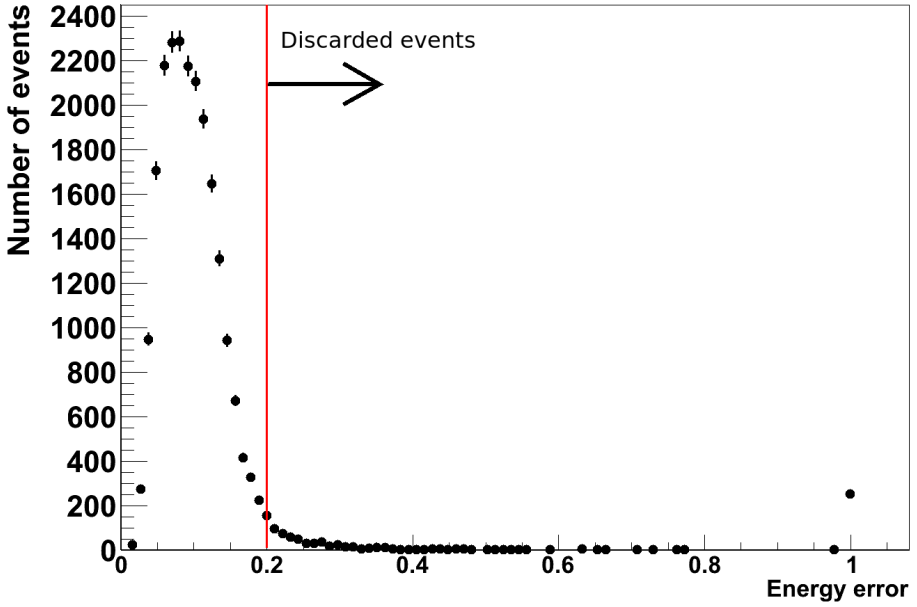

Figure 7.1: Distribution of the reconstructed energy error for reconstructed events. Only events with an energy error smaller than 20% pass. Events to the right of the red line are discarded.

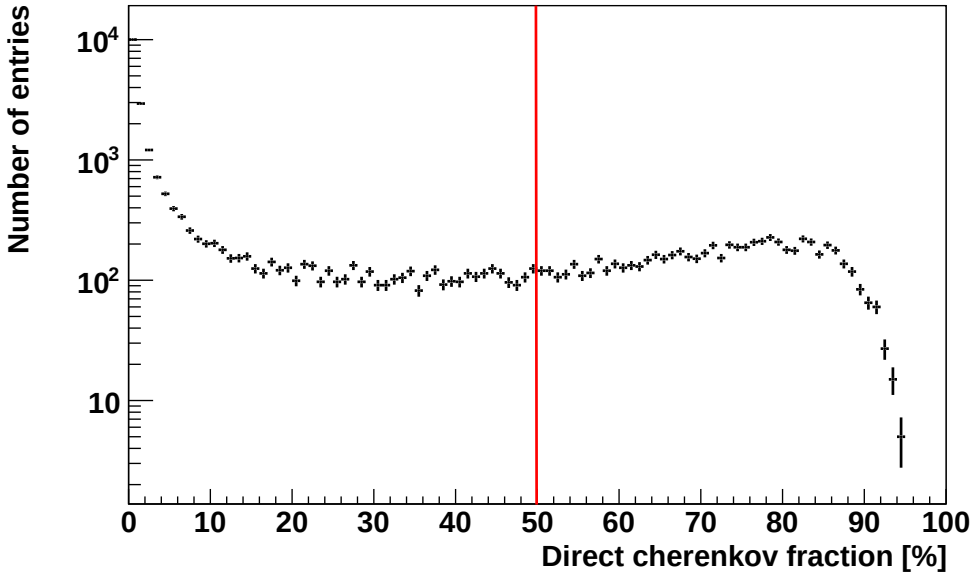

Figure 7.2: Event distribution of the direct Cherenkov fraction of the total light signal. Only events with a direct Cherenkov fraction smaller than 50% pass. Events to the right of the red line are discarded.

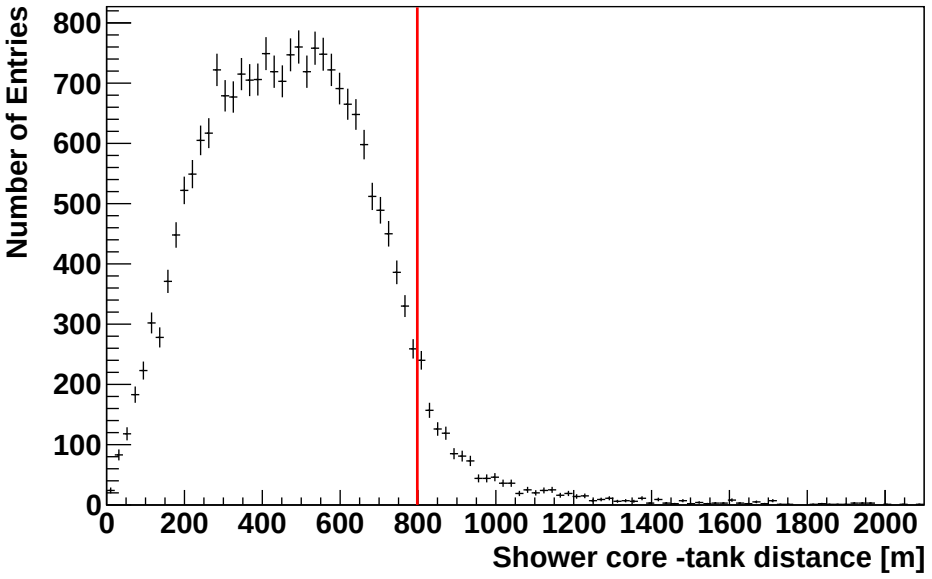

Figure 7.3: Distribution of minimal shower core - SD station distances. Only events with a core - station distance smaller than 800 meters pass. Events to the right of the red line are discarded.

changes for events with a larger zenith angle this cut is needed. The zenith angle distribution is shown in figure 7.4.(maxZenithFD 60.)

Profile Cuts

The shower maximum must be inside the detected field of view and at least 20 g/cm² distant from the field of view borders The reconstructed $X_{\max}$ of the passing events has to be in the field of view of the detector, otherwise the reconstruction is of low quality and has high systematic uncertainties. In addition the distance of the reconstructed $X_{\max}$ to the field of view borders of the detector has to be smaller than $20.0\,\mathrm{g/cm^2}$, a typical value of the $X_{\max}$ uncertainty. See figure 7.5 for the distribution.(xMaxInFOV 20.)

Possible holes without data in the profile have to be smaller than 30% of the total profile Possible holes in the measured shower profile have to be smaller than 30% of the observed profile in atmospheric depth. Two possible sources for holes in the measured profile exist: The first is the existence of a cloud between the detector and the air shower, tainting the measured light profile. The other source for holes in the measured profile are the gaps between the field of view of different telescopes (see for example figure 7.10). An event that is not contained to a single telescope field of view can fall with a part of its track into such a gap. If the fraction of the total track without data is to large, the event is discarded. The first source of holes in the profile exists only for measured data, because the simulated data does not contain any clouds. The second source for holes is possible for measured and simulated events. See figure 7.6 for the distribution of possible holes in the profile. For a discussion of this effect see chapter 7.3. (maxDepthHole 30)

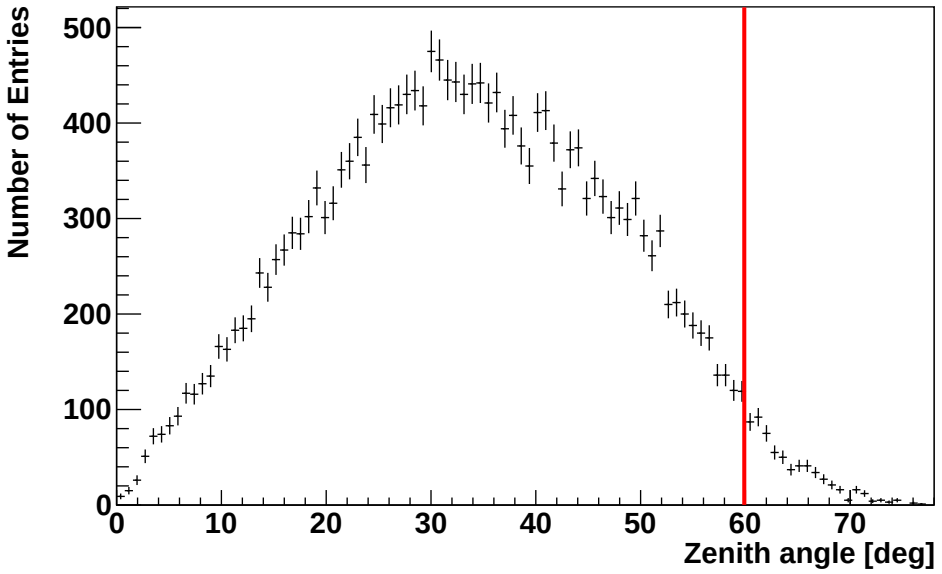

Figure 7.4: Zenith angle distribution for reconstructed events. Only events with a zenith angle smaller than 60° pass. Events to the right of the red line are discarded.

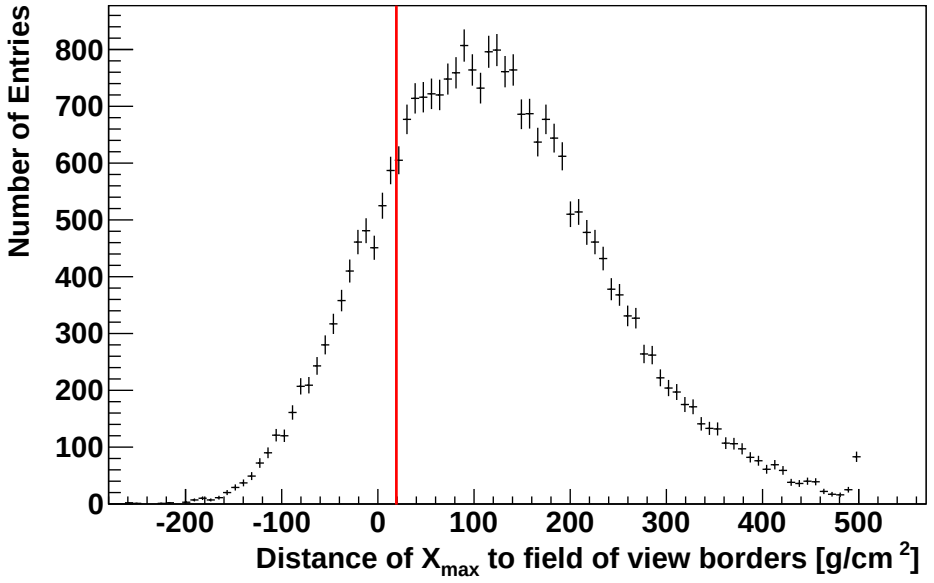

Figure 7.5: Distance of $X_{\max}$ to the detector field of view borders distribution for reconstructed events. Only events with a distance of $X_{\max}$ to the field of view borders larger than $20\,\mathrm{g/cm^2}$ pass. The field of view border of the detector is marked with the value of $0\,\mathrm{g/cm^2}$. Negative values are reconstructed shower maxima that are outside the field of view of the detector. Events to the left of the red line are discarded.

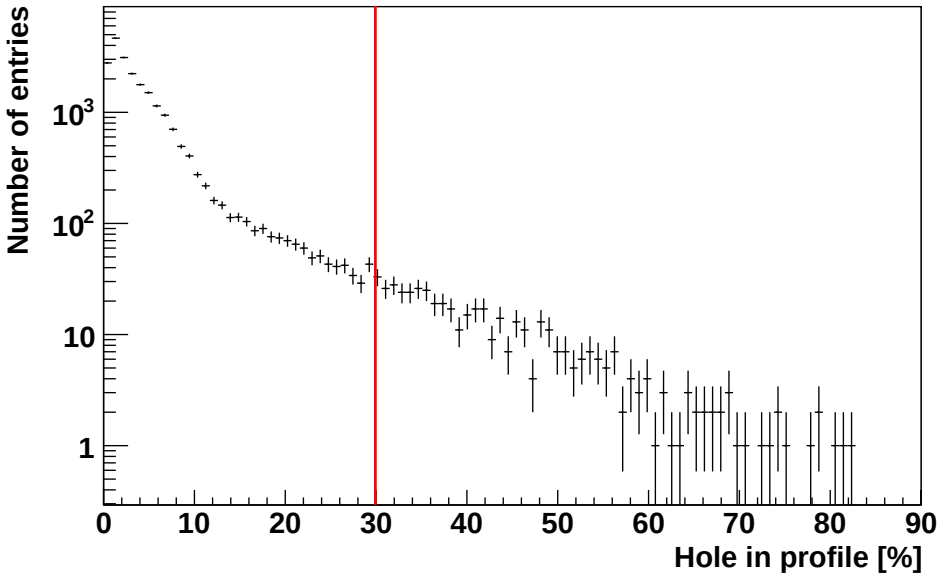

Figure 7.6: Size distribution of holes in the measured shower profile. Only events with a hole in the reconstructed profile smaller than 30% of the total profile pass. Events to the right of the red line are discarded.

The reduced χ^2/NDF of the Gaisser-Hillas fit has to be smaller than 2.5 This cut lets only events pass that have a relative high fit quality. The reduced χ^2/NDF of the Gaisser-Hillas fit of the shower profile has to be smaller than 2.5. The distribution of χ^2/NDF values is shown in figure 7.7. (profileChi2 2.5)

7.2 Selection efficiencies: Single and combined

The selection efficiencies for the cut set used consecutively on reconstructed data is shown in table 7.1. The data was produced with the standard reconstruction module chain used in this analysis from merged raw data of HEAT and Coihueco (see chapter 5). The efficiencies of the single cuts used on a preselected sample of hybrid events with a successful energy reconstruction is shown in table 7.2. The effect of the rate limiting is corrected for in the production of the raw data by the simpleMerger. This correction removes up to 30% of the events. For more details on the simpleMerger see chapter 5. A graphical representation is found in figure 7.8 for the event numbers and in figure 7.9 for the cut efficiencies.

The consecutive cut efficiencies for simulated data are given in the three tables 7.3, 7.4 and 7.5. The values show the cut efficiencies starting from hybrid events with a successful energy reconstruction. When comparing the cut efficiencies for real and simulated data, keep in mind, that the input distributions are fairly different, for example the different energy distribution and the cut-off in zenith angle distribution for simulated data have a large effect on the cut efficiencies. This explains the differences for the cut efficiencies between simulated and measured data. The applicability of every cut on measured and simulated data was cross-checked. The differences in cut efficiencies between different models and primary particles are small.

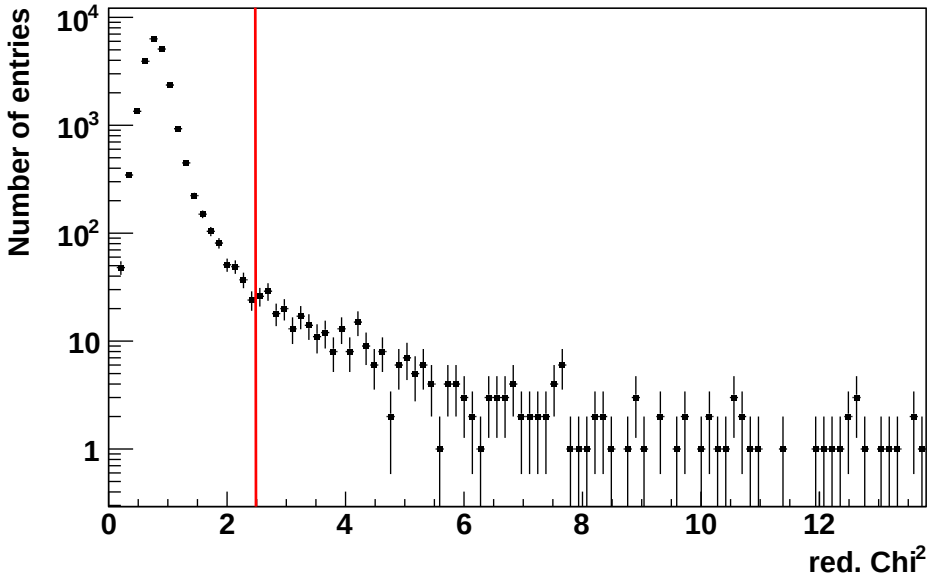

Figure 7.7: Distribution of reduced χ^2 values of the profile fit. Only events with a reduced χ^2/NDF smaller than 2.5 pass. Events to the right of the red line are discarded.

Combined efficiencies			
Cut Name	Number of Events	Efficiency	Total efficiency
Raw data	597877	-	100%
hasEnergy	123741	20.7 %	20.7%
isHybrid	123672	99.9 %	20.7%
heatOrientationUp	119680	96.8 %	20.0%
eyeCut	55012	46.0 %	9.2%
skipSaturated	54683	99.4 %	9.2%
badPixels	54683	100.0 %	9.2%
maxZenithFD	50652	92.6 %	8.5%
maxCoreTankDist	47981	94.7 %	8.0%
energyError	34116	71.1 %	5.7%
maxDirCFrac	26625	78.0 %	4.5%
xMaxInFOV	21208	79.7 %	3.6%
profileChi2	20825	98.2 %	3.5%
maxDepthHole	20152	97.9 %	3.4%

Table 7.1: Number of events and cut efficiencies when used consecutively on measured data.

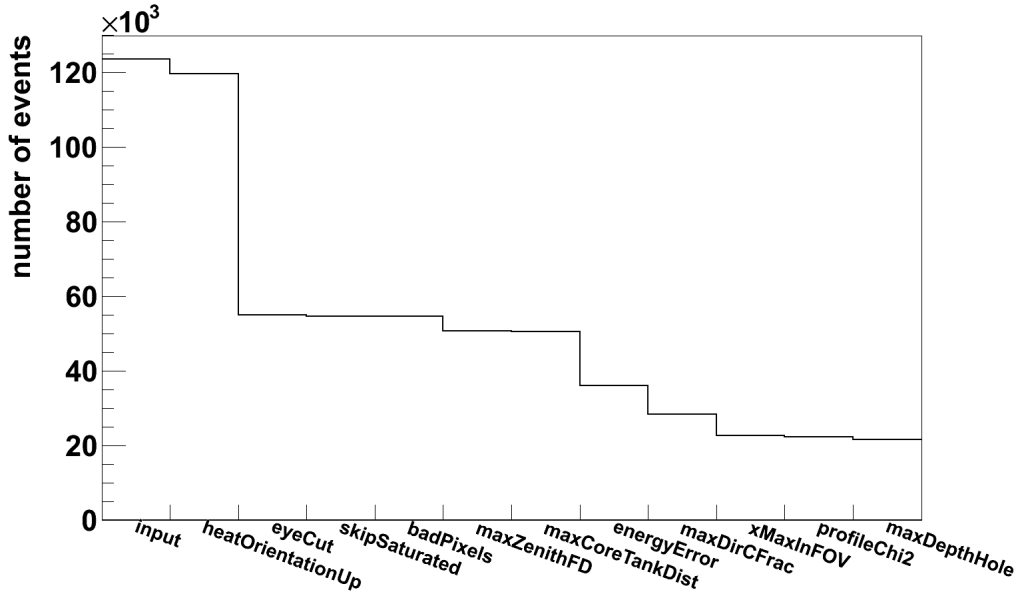

Figure 7.8: The number of events after applying the consecutive cuts on measured data, starting from hybrid events with a successful energy reconstruction.

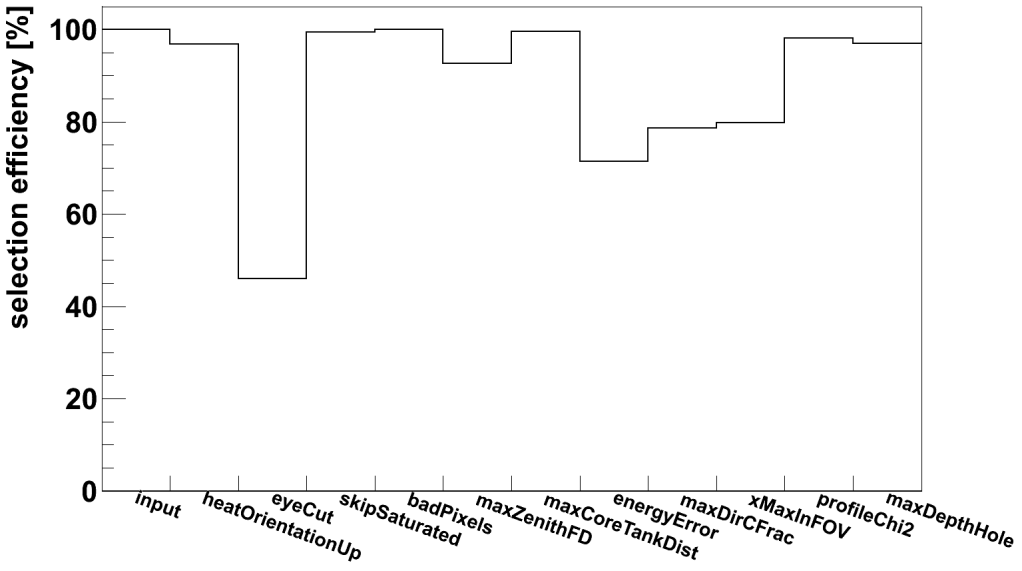

Figure 7.9: The efficiencies of the consecutive cuts on measured data, starting from hybrid events with successful energy reconstruction.

Single efficiencies		
Cut Name	Number of Events	Efficiency
hasEnergy / isHybrid	123672	-
heatOrientationUp	88491	71.6%
eyeCut	55012	44.5%
skipSaturated	123022	99.5%
badPixels	123672	100.0%
maxZenithFD	113484	91.8%
maxCoreTankDist	115007	92.9%
energyError	82633	66.8%
maxDirCFrac	86943	70.3%
xMaxInFOV	81249	65.7%
profileChi2	114865	92.9%
maxDepthHole	116556	94.2%

Table 7.2: Number of events and cut efficiencies when used without other cuts on measured data.

Cut efficiencies, Epos simulation		
Cut Name	Efficiency proton	Efficiency iron
heatOrientationUp	100.0 %	100.0%
eyeCut	37.8 %	36.8%
skipSaturated	99.5 %	99.6%
badPixels	100 %	100.0%
maxZenithFD	85.7 %	85.5%
maxCoreTankDist	84.1 %	85.7%
energyError	93.8 %	94.4%
maxDirCFrac	99.5 %	99.3%
xMaxInFOV	93.0 %	94.1%
profileChi2	99.4 %	98.4%
maxDepthHole	99.1 %	99.4%

Table 7.3: Cut efficiencies when used consecutively on simulated data with the Epos model.

Unused cuts from standard analyses

The Pierre Auger Observatory uses a quality database generated from the atmospheric monitoring and other sources for the FD events. This database contains for example information on the cloud coverage and the aerosol content of the atmosphere. As explained earlier, the generation of a part of these databases needs calibrated telescopes, so that for HEAT no information is available at this moment. It is possible to use additional cuts on basic shower parameters, but in light of the missing quality database information, the used cuts and their values are enough to guarantee an selection of high quality events with little to no bias. The inclusion of additional cuts as soon as the information is available is planned for future analyses.

Cut efficiencies, Sibyll simulation		
Cut Name	Efficiency proton	Efficiency iron
heatOrientationUp	100.0 %	100.0%
eyeCut	37.7 %	36.6%
skipSaturated	99.7 %	99.5%
badPixels	100 %	100.0%
maxZenithFD	84.8 %	85.0%
maxCoreTankDist	82.2 %	85.5%
energyError	93.4 %	94.4%
maxDirCFrac	99.6 %	99.5%
xMaxInFOV	92.8 %	93.8%
profileChi2	99.0 %	99.2%
maxDepthHole	99.1 %	99.0%

Table 7.4: Cut efficiencies when used consecutively on simulated data with the Sibyll model.

Cut efficiencies, QGSJET-II simulation		
Cut Name	Efficiency proton	Efficiency iron
heatOrientationUp	100.0 %	100.0%
eyeCut	37.9 %	36.9%
skipSaturated	99.6 %	99.5%
badPixels	100 %	100.0%
maxZenithFD	84.7 %	85.8%
maxCoreTankDist	82.3 %	85.5%
energyError	93.8 %	94.9%
maxDirCFrac	99.3 %	99.1%
xMaxInFOV	93.0 %	94.5%
profileChi2	99.0 %	99.2%
maxDepthHole	98.9 %	99.4%

Table 7.5: Cut efficiencies when used consecutively on simulated data with the QGSJET-II model.

Because this analysis works with data generated by the FD, only cuts on the FD part of the events are applied. The information from possible golden hybrid events in the dataset is not used.

7.3 Limits of the air shower simulation

One particular component that is missing from the air shower simulation is the existence of clouds or fog in the atmosphere. Clouds can block out or absorb the light from parts of the air shower profile. In the worst case, no light from an air shower reaches the detector. To guarantee a minimum effect of clouds on the data taking operations, the the cloud coverage of the detector is monitored, for example by the LIDAR and with weather satellites and cloud cameras. For periods with a

high cloud fraction or bad weather, the data taking operations are stopped, or the period is excluded from an analysis afterwards.

The effect of single clouds moving through the field of view of the detector is not accounted for in this process. Single clouds (or local bad atmospheric conditions in general) have to be identified by the atmospheric monitoring (see chapter 4.2.3). Without the quality database for HEAT, this information is missing. The same is true for the air shower simulation: The simulation contains no cloud information.

One possible way to quantify the effect of single clouds on the data is the cut on allowed holes in the detected profiles of air showers. It is mainly needed because of the inhomogeneous detector coverage of the detector COHE, which is comprised from the field of view of nine single telescopes. Because of the construction of the HEAT telescopes, gaps between the field of view of single telescopes exist, see for example figure 7.10. Depending on the geometry of single air showers, it is possible, that parts of the shower profile fall into these gaps and can not be measured. The cut on possible holes in the measured profile compares the profile to the field of view of the telescopes and discards the event if more than 30 % of the detected profile in atmospheric depth falls is not registered.

In shower simulations, the gaps between the telescopes are the only source of holes in the profile. This excludes defective pixels or telescopes, which are not included in the simulation and possible non triggered pixels in the middle of the profile, because shower profiles have a typical shape, where the light intensity is highest in the middle of the profile and smaller at the beginning and end. For real showers, clouds are an additional source of holes in the measured profile of air showers. Simulated and real showers use the identical detector configuration, in other words they have the same gaps between telescope field of view. Differences in the cut efficiencies for the hole cut and the distribution of hole sizes between real and simulated data must then stem from clouds in the real data. Figure 7.11 shows the distribution of the size of holes in the profiles of simulated showers. The plot was generated with a representative subset of the simulated dataset of air showers with proton primaries and the QGSJET-II hadronic model. The distribution is similar for all compositions and hadronic models. Comparing figure 7.11 for simulated data to figure 7.6 for data shows differences in the distributions. For real data, the distribution goes from 0% to 85%, whereas the distribution for simulated data only goes from 0% to around 60%. In addition, the shapes of the distributions is different. This can be a hint of the effect of clouds on the data taking process. The use of the quality database in a future analysis will reduce this differences.

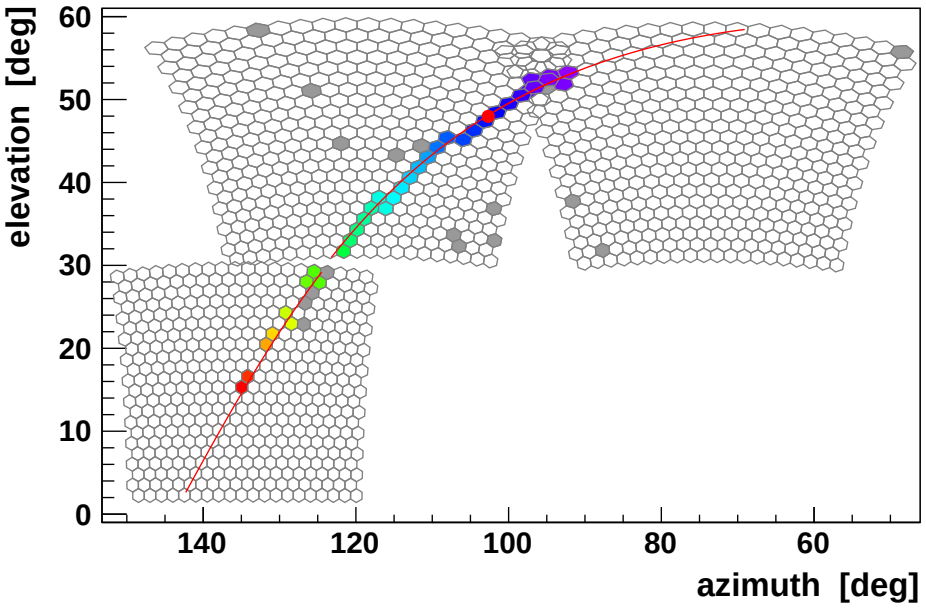

Figure 7.10: This figure shows the pixel pattern of a reconstructed COHE event with an energy of around 10^{17} eV which was recorded in 2 HEAT mirrors and one Coihueco mirror. Without HEAT, this event would not have been reconstructable. Notice the gaps between the telescope field of views.

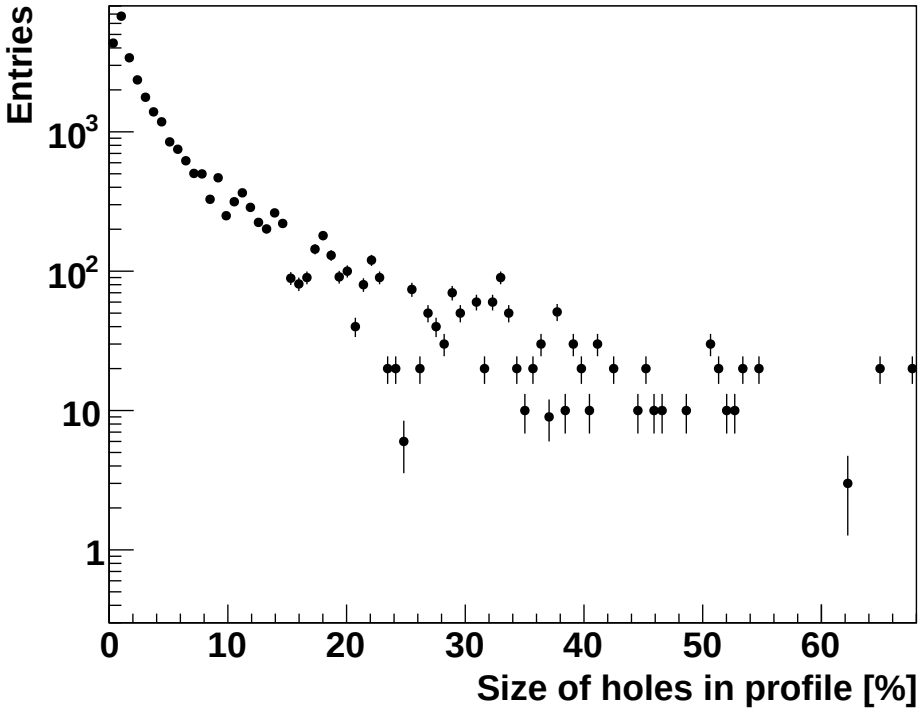

Figure 7.11: Distribution of the size of holes in the measured shower profile for simulated air showers. Data from proton air showers simulated with QGSJET-II is shown. Only a representative part of the total simulated data is shown.

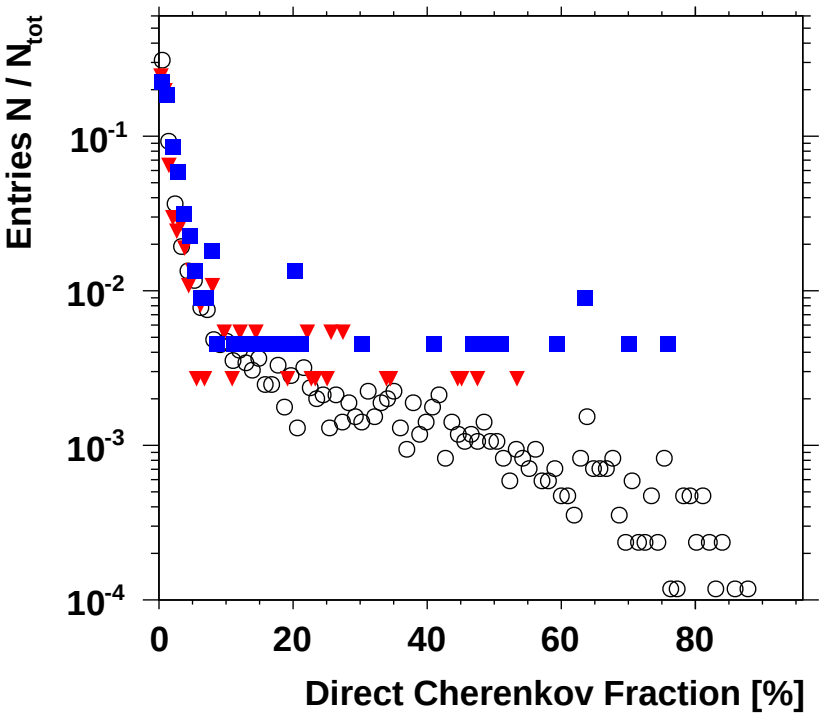

Figure 7.12: This figure shows the distribution of the reconstructed direct Cherenkov light fraction for the different models and primaries and real data in the energy bin centered at $10^{17.5}$ eV after all other cuts. Real data is shown by the open black circles, the red triangles represent data simulated with Epos and proton primaries and the blue squares represent simulated data with Epos and iron primaries.

7.4 Comparison of measured and simulated data

The use of the simulated dataset to calculate the exposure is only possible, if the simulated dataset represents the real data reasonably well. To compare real and simulated data, basic shower parameters have to be analyzed. These basic shower parameters are for example the parameters used for the data quality cuts. A comparison between the distributions of the single cut parameters for real data and simulated data of proton and iron primaries with the Epos interaction model is shown in the following section. The figures give the distribution of the shown values, after all other cuts have been used on the dataset. Only the distributions for the energy bin centered at $E = 10^{17.5} eV$ are shown. All plots are normalized to the total number of entries (Epos proton, Epos iron or real data respectively). The distributions for the other energy bins and hadronic models are comparable, with differences stemming from the differences in energy and the differences between the models.
In the figures 7.12 to 7.17 and 7.19, the open black circles give the distribution of real data, the red triangles give the distribution of data simulated with Epos and proton primaries whereas the blue squares give the distribution of data simulated with Epos and iron primaries.

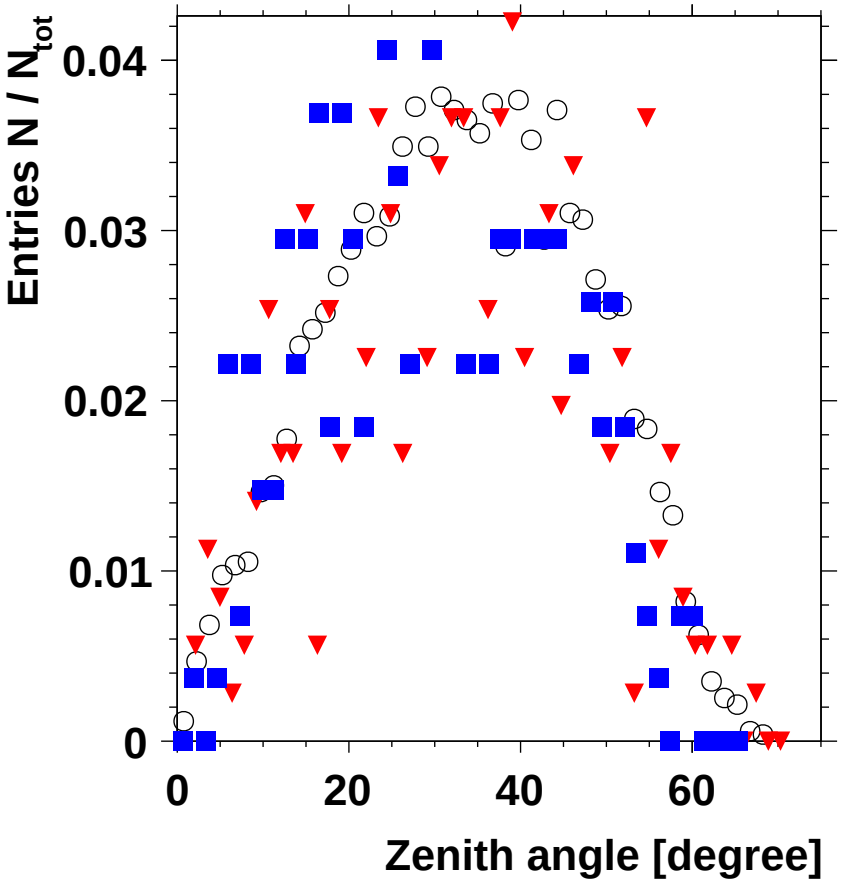

Figure 7.13: This figure shows the distribution of the reconstructed zenith angles for the different models and primaries and real data in the energy bin centered at $10^{17.5}$ eV after all other cuts. Real data is shown by the open black circles, the red triangles represent data simulated with Epos and proton primaries and the blue squares represent simulated data with Epos and iron primaries.

Figure 7.12 shows the distribution of the fraction of reconstructed direct Cherenkov light in the events. The distributions are comparable for lower Cherenkov - fractions. The differences for higher Cherenkov - fractions between simulated and real data stem from the Offline simulation and reconstruction software. It was not developed to handle low energy events with dominant Cherenkov fractions, but only to treat Cherenkov light as an additional information source. The used cut of a maximum Cherenkov fraction of 50 % is motivated by this fact.

Figure 7.13 shows the distribution of reconstructed zenith angles. The distributions agree well, the only difference between real and simulated data are visible for zenith angles larger than 60°. This difference can be explained by the limited range of simulated air showers (only showers with zenith angles smaller than 65° were simulated), whereas real data events can be detected up to 80° or even higher. The analysis uses only events with a zenith angle smaller than 60°.

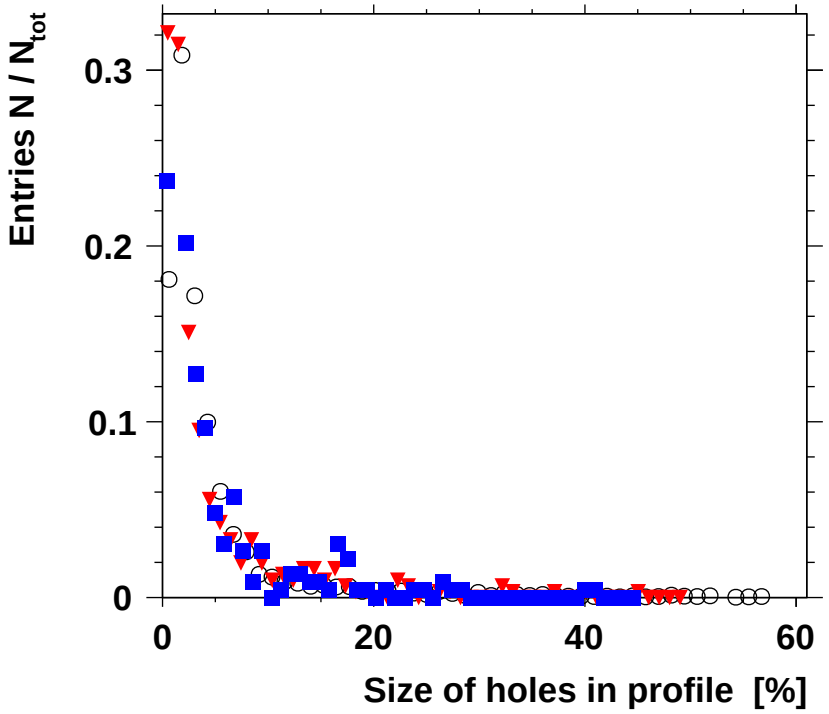

Figure 7.14: This figure shows the distribution of the size of holes in the reconstructed profile for the different models and primaries and real data in the energy bin centered at $10^{17.5}$ eV after all other cuts. Real data is shown by the open black circles, the red triangles represent data simulated with Epos and proton primaries and the blue squares represent simulated data with Epos and iron primaries.

Figure 7.14 shows the distribution of the size of holes in the reconstructed shower profiles. The distributions are comparable, small differences can be explained by the differences between data and simulation, see chapter 7.3.

The distribution of the distance from the shower core to the nearest surface detector station in figure 7.15 shows some larger differences between data and simulation, especially for larger distances. These differences can be explained by the differences between real data and simulation. For the simulated air showers, the distribution of shower cores is contained inside the surface detector array, leading to a maximum distance of roughly 750 m, half the distance between detector stations. For real data no such a priory containment exists, leading to the possibility of shower cores outside the array with higher distances. The analysis is contained inside the array by using only events with a shower core to station distance smaller than 800 m.

The distributions of the reconstructed energy error is shown in figure 7.16. All distributions agree very well, the outliers with high energy errors in real data are removed by the cut on the maximum allowed energy error of 20%.

The same is true for the distribution of the reduced chi-square value of the Gaisser-Hillas fit of the shower profile, shown in figure 7.17. All distributions agree very well

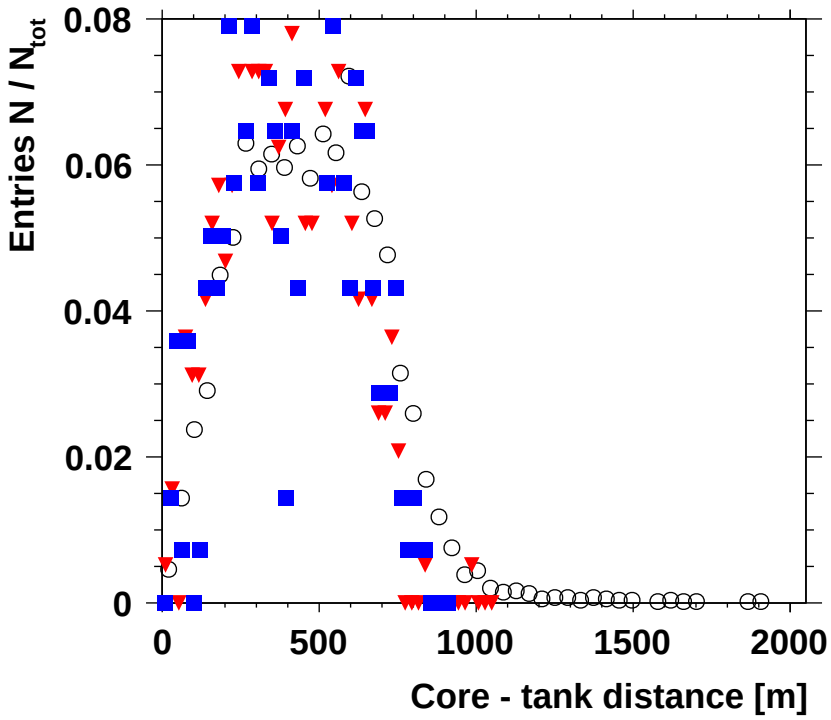

Figure 7.15: This figure shows the distribution of the distance of the reconstructed shower core to the nearest surface detector station for the different models and primaries and real data in the energy bin centered at $10^{17.5}$ eV after all other cuts. Real data is shown by the open black circles, the red triangles represent data simulated with Epos and proton primaries and the blue squares represent simulated data with Epos and iron primaries.

and found outliers in real data are removed by the cut on the allowed chi-square value.

The fact that no high values for the energy error and the reduced chi-square value of the Gaisser-Hillas fit of the shower profile are found in the simulated event as compared to real data, although outside the used datasets, has to be studied.

Whereas the last six distributions have shown a good agreement between the simulated and real data (or only differences outside the used dataset), the following distribution shows a visible difference between simulated and real data or simulated data with different primaries. These differences stem from intrinsic differences between the models, the primary particles and the real data. Best seen are these differences in the distribution of the reconstructed shower maximum X_{max}. These distributions are shown in figure 7.18 for the energy bin centered at $10^{17.5}$ eV. The values for all six combinations of primary particle and hadronic interaction model are shown. The red markers represent the proton primaries, whereas the blue markers represent iron primaries. The real data is shown with black markers.

The distributions show, that it is not possible to recreate the data distribution with the used simulations. The shape of the data distribution looks more like the proton

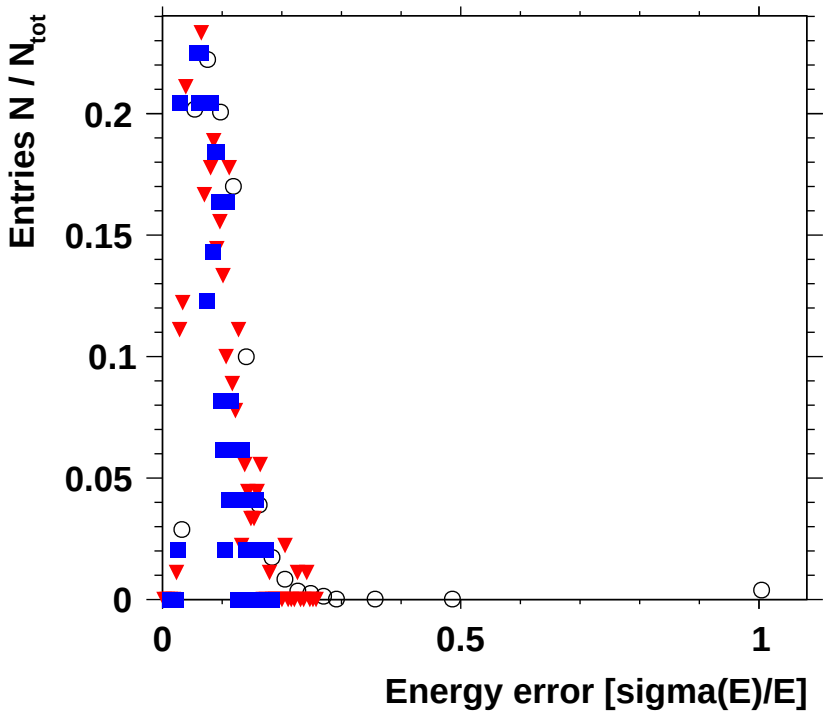

Figure 7.16: This figure shows the distribution of the reconstructed energy error for the different models and primaries and real data in the energy bin centered at $10^{17.5}$ eV after all other cuts. Real data is shown by the open black circles, the red triangles represent data simulated with Epos and proton primaries and the blue squares represent simulated data with Epos and iron primaries.

simulations and the peak of the data distribution lies between those for iron and proton simulations. Also differences between the different models are visible. For further analyses, changes in the used models could lead to a better representation of the data by the simulations. If this is not sufficient a modified primary composition has to be used for the simulation, which depends on an analysis of the primary composition in this energy range. A composition study with HEAT data can be found in "Mass composition studies with the low energy extension HEAT at the Pierre Auger Observatory"[106]. These composition analyses are ongoing. For this analysis only single particle compositions were used, with iron and proton primaries as extreme values of the expected real composition. This leads to differences in other shower parameters, as can be seen in the following:

The distribution of the distance of the reconstructed shower maximum to the field of view borders of the detector is shown in figure 7.19. This is a projection of the X_{max} distribution from figure 7.18 into the detector field of view, which leads to the visible differences.

Real data and simulated showers show a good agreement in basic shower parameters. Differences between real and simulated events can be explained by differences between in the simulation and reconstruction process that are understood and intrinsic differences between real data and the used models and primaries. The good agree-

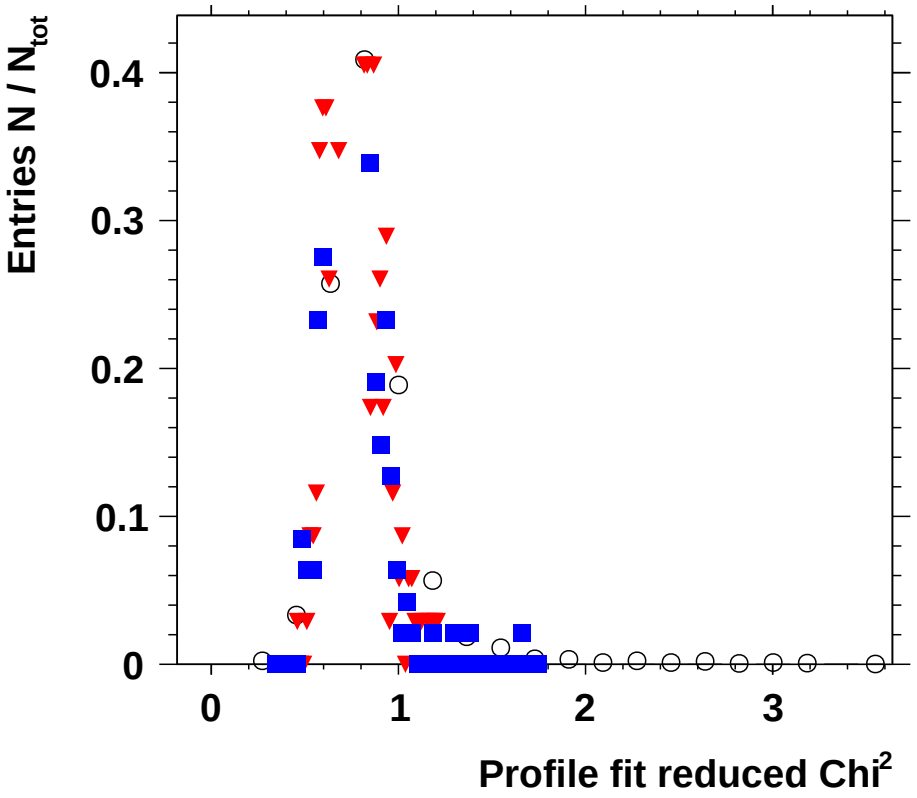

Figure 7.17: This figure shows the distribution of the $\chi^2/ndof$ values of the Gaisser-Hillas fit to the shower profile for the different models and primaries and real data in the energy bin centered at $10^{17.5}$ eV after all other cuts. Real data is shown by the open black circles, the red triangles represent data simulated with Epos and proton primaries and the blue squares represent simulated data with Epos and iron primaries.

ment allows the use of the simulated air showers for the calculation of the detector performance.

7.5 Results

This chapter described the data selection of high quality events both in measured and simulated air shower data. The data selection process, first by means of the simpleMerger, to include the effect of the HEAT rate limiting, and then by cutting low quality events, reduces the number of events from 597877 to 20152 that are used for this energy spectrum analysis. Keep in mind, that until the eyeCut is performed, the same physical event is represented two or three times in the data: First as event in the physical eye that measured the event and then a second time in the virtual eye COHE. Events, that were seen by both Coihueco and HEAT are counted as three events before the eye cut is applied: Once for Coihueco, once for HEAT and the third time in COHE.

The total selection efficiency for data is 3.4 %. The same selection process is applied to simulated data with comparable effects.

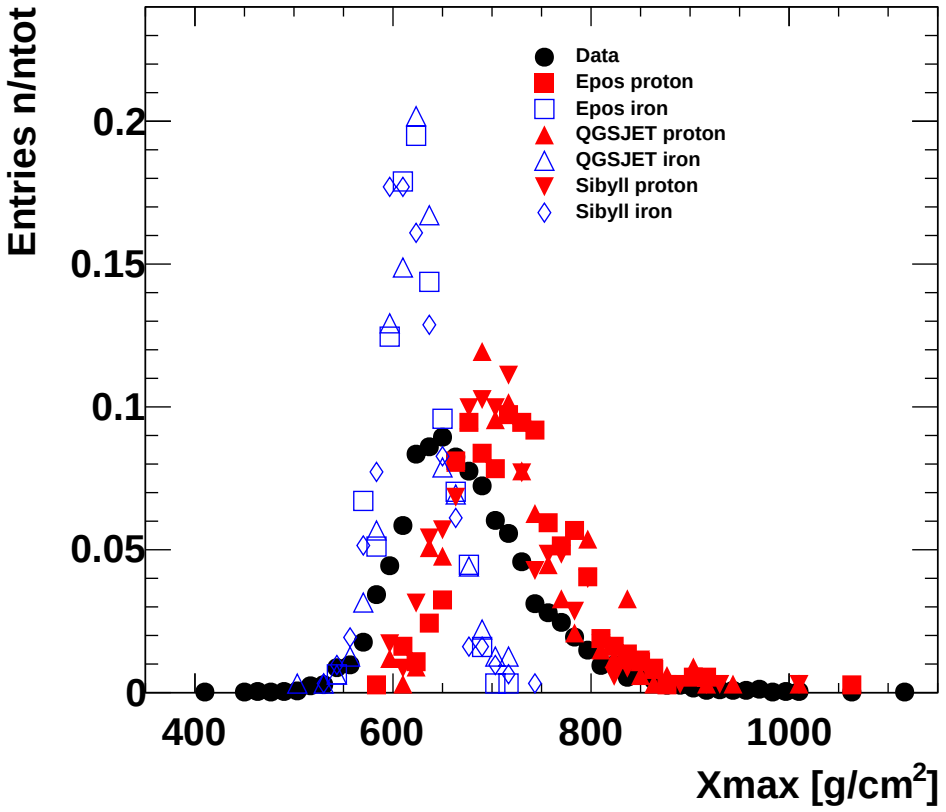

Figure 7.18: This figure shows the distribution of the X_{max} values for the different models and primaries and real data in the energy bin centered at $10^{17.5}$ eV after all cuts. See text for details.

The comparison of real and simulated data shows a good agreement for many shower parameters and understood differences in others. This allows the use of the simulated showers for the calculation of the detector exposure, shown in the next chapter.

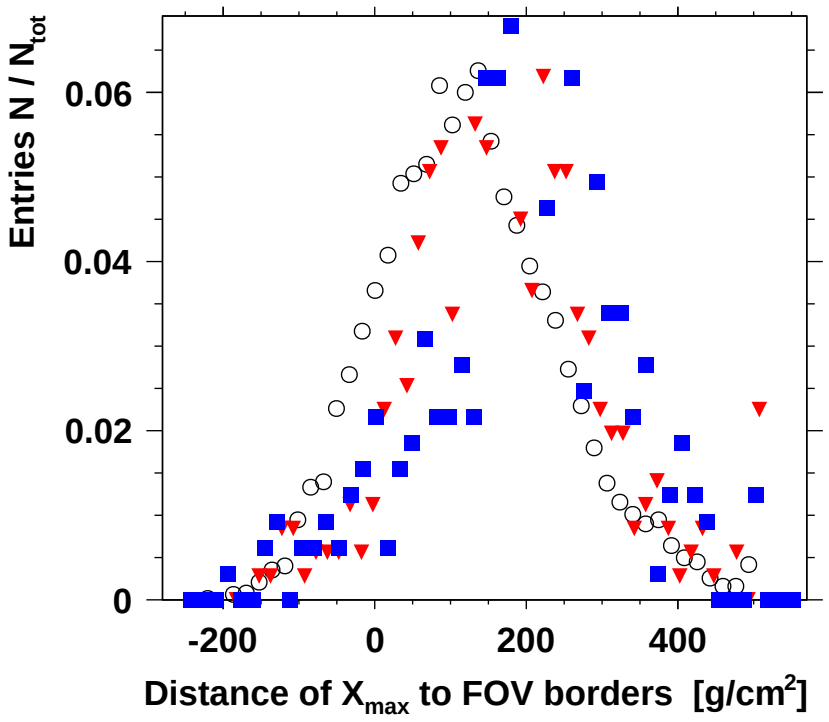

Figure 7.19: This figure shows the distribution of the distance of the shower maximum X_{max} to the field of view borders for the different models and primaries and real data in the energy bin centered at $10^{17.5}$ eV after all other cuts. Real data is shown by the open black circles, the red triangles represent data simulated with Epos and proton primaries and the blue squares represent simulated data with Epos and iron primaries.

8. Exposure Calculation

The goal of this study is the measurement of the absolute flux of cosmic rays. Assuming a time independent, isotropic flux of cosmic rays, meaning that the flux of cosmic rays is independent of time, location and observation angle, the flux of cosmic rays as a function of energy can be defined as[153]:

$$J(E) = \frac{\mathrm{d}^4 N_{\mathrm{inc}}}{\mathrm{d}E\ \mathrm{d}S\ \mathrm{d}\Omega\ \mathrm{d}t} \simeq \frac{\Delta N_{\mathrm{sel}}(E)}{\Delta E} \frac{1}{\varepsilon(E)} \tag{8.1}$$

with N_{inc} as the number of cosmic rays with energy between $E - \frac{\mathrm{d}E}{2}$ and $E + \frac{\mathrm{d}E}{2}$ that hit a surface element $\mathrm{d}S$ within the solid angle $\mathrm{d}\Omega$ and the time $\mathrm{d}t$. ΔN_{sel} is the number of detected events after selection in an energy bin centered at E and with a width of ΔE. $\varepsilon(E)$ is the energy dependent exposure of the detector, calculated with the same selection process as for the detected events.

The assumption that the flux of cosmic rays is time independent and isotropic is valid for the studied energy range of cosmic rays. For example, no deviations from isotropy in the arrival directions of cosmic rays were found by the Pierre Auger Observatory for energies above $10^{18}\,\mathrm{eV}$ [154]. Only for the highest energies, the arrival directions are not isotropic anymore (see [18]). The flux of cosmic rays is time dependent only for cosmic rays with a much lower energy [155] because it is influenced by the sun or more correctly the solar weather.

Following from this, it is clear, that the calculation of the exposure is an important part for the spectrum measurement. The following chapter describes the exposure calculation and gives the energy dependent exposure values for several hadronic interaction models and primary compositions.

8.1 The exposure

A figure to describe the observational capability of a cosmic ray detector is the instantaneous aperture $\mathcal{A}(E,t)$ which depends on the energy E and the time t. The time dependence of the aperture stems from the fact that the detector can be operated in several different configurations, each with its own aperture. The time integrated aperture is called the exposure $\varepsilon(E)$. It can be defined as[153]:

$$\varepsilon(E) = \int_T \int_\Omega \int_{S_{\mathrm{gen}}} e(E,t,\theta,\phi,x,y) \cos\theta\ \mathrm{d}S\ \mathrm{d}\Omega\ \mathrm{d}t = \int_T \mathcal{A}(E,t)\mathrm{d}t, \tag{8.2}$$

where $e(E, t, \theta, \phi, x, y)$ is the detection efficiency including all analysis steps, i.e. the trigger efficiency, the reconstruction efficiency and the selection efficiency of the quality cuts. $\mathrm{d}S = \mathrm{d}x \times \mathrm{d}y$ is the horizontal surface element at the coordinates x and y. $\mathrm{d}\Omega = \sin\theta \, \mathrm{d}\theta \, \mathrm{d}\phi$ and Ω are the differential and total solid angles, with the zenith angle θ and the azimuth angle ϕ. T is the time in which the detector was actively taking data, called uptime in the following. The generation area S_{gen} is the area which contains the active detection area of the detector. It has to be chosen large enough to make any event detection and reconstruction outside of it impossible.

The aperture $\mathcal{A}(E, t)$ can be given as[156]:

$$\mathcal{A}(E,t) = \int_{\Omega} \int_{S_{\mathrm{gen}}} e(E, t, \theta, \phi, x, y) \; \mathrm{d}S \; \cos\theta \; \mathrm{d}\Omega = \int_{\Omega} S_{\mathrm{eff}} \; \mathrm{d}\Omega \tag{8.3}$$

with $S_{\mathrm{eff}}(E, \theta)$ the effective area

$$S_{\mathrm{eff}}(E,\theta) = \int_{S_{\mathrm{gen}}} e(E, t, \theta, \phi, x, y) \; \cos\theta \; \mathrm{d}S, \tag{8.4}$$

where $\cos\theta \cdot \mathrm{d}S$ is the differential area projected onto the normal direction of the incoming shower with zenith angle θ. Note that in this form, the effective area depends on the energy and zenith angle of the air showers.

The exposure calculated in this chapter is always the exposure for the detector description COHE, that is the combination of the FD eyes Coihueco and HEAT, when all HEAT telescopes are in the upward position and all HEAT and Coihueco telescopes are actively taking data. Times with other detector configurations are not considered. This means, that only the aperture for this specific detector configuration has to be calculated.

The result of the exposure calculation shown in the last section of this chapter was done directly from the calculated efficiencies. Al partial results (for example the effective area or the aperture) were calculated separately. The values given in the tables in this and the following chapter are rounded for the sake of readability.

8.2 Aperture Calculation

The calculation of the aperture $\mathcal{A}(E, t)$ is separated into several steps that depend on each other.

8.2.1 The generation area

The generation area S_{gen} for the different energies was chosen when the shower cores for the shower simulation were generated (see chapter 6.3). The shower cores were distributed between two concentric half-circles, the inner one with a radius of 1000 meters and the outer one with a radius that gets larger with increasing energy. Both half circles were centered at the position of the FD eye Coihueco. The radius of the inner cycle was chosen to be 1000 m because non existent surface detector stations in this range make it impossible for a hybrid shower core to lie in this range. The radius of the outer half circle is derived from data (see chapter 6.3). The used radii and resulting generation areas for the different energies are shown in table 8.1. These values are the same for every model and composition.

Energy in $\log_{10}(E/\text{eV})$	Max. sim. distance [m]	Generation Area $S_{\text{gen}}[\text{km}^2]$
16.50	5,400	44.2336
16.75	7,800	93.9965
17.00	12,600	247.809
17.25	14,400	324.150
17.50	18,600	541.862
17.75	25,800	1044.01
18.00	29,200	1337.75
18.25	32,400	1647.39
18.50	35,400	1966.89

Table 8.1: Energy dependent generation area for the exposure calculation

8.2.2 Calculation of the reconstruction efficiencies

The total reconstruction efficiency $e(E, t, \theta, \phi, x, y)$ is calculated by building the fraction of the number of successfully reconstructed simulation events over the total number of simulated events for every energy bin. By using a static detector description, a flat distribution of shower cores and isotropic distributed shower angles (from 0° to 60° in zenith angles and from 0° to 360° in azimuth angles), the dependencies of the efficiency on zenith angle θ, azimuth angle ϕ and the position of the shower core (x, y) are removed.

$$e(E, t, \theta, \phi, x, y) = e(E) = \frac{N_{\text{rec}}}{N_{\text{sim}}} \tag{8.5}$$

The total efficiency contains the product of the different efficiencies from simulation, trigger and reconstruction. The upper value of the zenith angle θ of 60° was chosen, because the trigger efficiency of the SD changes for air showers with higher zenith angles and the effect of the Earth's atmosphere and the curvature of the Earth are not negligible anymore (see [124]).

The 720,000 air showers simulated in the first step were used to check the simulation procedure, mainly if the distance from the detector to the shower core of the simulated showers was really smaller than the maximum simulation distance. This was the case for all simulations. Afterwards, the reconstruction efficiency was calculated for the different energy bins, models and compositions.
Because of the very low efficiencies, especially for the low energies, the number of simulated showers was increased, until the statistical error of the efficiencies was smaller than 15%. The number of simulated showers was then set to match for all models and compositions. In total, 2,343,000 air showers were simulated for the exposure calculation.

The number of simulated input showers per energy bin is given in table 8.2. The resulting values of the efficiencies for the different hadronic interaction models and primary compositions are given in the tables 8.3 to 8.5 in percent. The uncertainty on the efficiency was calculated as statistical uncertainty on the number of successfully reconstructed showers per energy bin. This is a conservative error approximation.

Number of simulated input showers N_{sim}	
Energy in $\log_{10}(E/\text{eV})$	
16.50	120,000
16.75	77,500
17.00	53,000
17.25	33,000
17.50	27,000
17.75	25,000
18.00	20,000
18.25	18,000
18.50	17,000

Table 8.2: Number of simulated input showers per energy bin. Same for all studied combinations of composition and model.

Total efficiency $e(E)$, Epos simulation		
Energy in $\log_{10}(E/\text{eV})$	Pure proton composition	Pure iron composition
16.50	(0.048 ± 0.006) %	(0.053 ± 0.007) %
16.75	(0.390 ± 0.02) %	(0.425 ± 0.02) %
17.00	(1.20 ± 0.05) %	(1.33 ± 0.05) %
17.25	(4.60 ± 0.12) %	(5.02 ± 0.12) %
17.50	(8.51 ± 0.18) %	(9.52 ± 0.19) %
17.75	(10.0 ± 0.2) %	(10.9 ± 0.2) %
18.00	(23.7 ± 0.3) %	(26.2 ± 0.4) %
18.25	(37.9 ± 0.5) %	(40.7 ± 0.5) %
18.50	(43.3 ± 0.5) %	(46.9 ± 0.5) %

Table 8.3: Total efficiency for air showers simulated with Epos. The shown error is the statistical uncertainty.

The resulting efficiency is by no means a "true" efficiency of the detector at these energies but depends explicitly on the chosen generation area.

8.2.3 The effective area

The effective area $S_{\text{eff}}(E, \theta)$ contains information on the total efficiencies and the active area of the detector. The active area describes the area which contains shower cores after reconstruction and selection for this specific simulation. For the aperture calculation, the mean effective area $\overline{S_{\text{eff}}}(E)$ is calculated. The mean effective area is the effective area averaged over the solid angle. The mean effective area is calculated as the fraction of successfully reconstructed simulated showers N_{rec} over the total number of simulated showers N_{sim}, which is the efficiency (which is not depending on the zenith angle), times the generation area for this specific energy bin, model and composition.

$$\overline{S_{\text{eff}}}(E) = \frac{N_{\text{rec}}}{N_{\text{sim}}} \cdot S_{\text{gen}}(E) = e(E) \cdot S_{\text{gen}}(E) \tag{8.6}$$

Total Efficiency $e(E)$, QGSJET-II simulation		
Energy in $\log_{10}(E/\text{eV})$	Pure proton composition	Pure iron composition
16.50	(0.044 ± 0.006) %	(0.047 ± 0.006) %
16.75	(0.345 ± 0.02) %	(0.365 ± 0.02) %
17.00	(1.098 ± 0.05) %	(1.155 ± 0.05) %
17.25	(4.03 ± 0.11) %	(4.33 ± 0.12) %
17.50	(7.29 ± 0.16) %	(8.16 ± 0.17) %
17.75	(8.89 ± 0.19) %	(9.48 ± 0.20) %
18.00	(21.1 ± 0.3) %	(22.9 ± 0.3) %
18.25	(30.4 ± 0.4) %	(37.8 ± 0.5) %
18.50	(38.5 ± 0.5) %	(42.3 ± 0.5) %

Table 8.4: Total efficiency for air showers simulated with QGSJET-II. The shown error is the statistical uncertainty.

Total Efficiency $e(E)$, Sibyll simulation		
Energy in $\log_{10}(E/\text{eV})$	Pure proton composition	Pure iron composition
16.50	(0.038 ± 0.006) %	(0.043 ± 0.006) %
16.75	(0.311 ± 0.02) %	(0.338 ± 0.02) %
17.00	(0.949 ± 0.04) %	(1.032 ± 0.04) %
17.25	(3.56 ± 0.10) %	(3.90 ± 0.11) %
17.50	(6.49 ± 0.16) %	(7.18 ± 0.16) %
17.75	(8.02 ± 0.18) %	(8.88 ± 0.19) %
18.00	(18.2 ± 0.3) %	(20.9 ± 0.3) %
18.25	(26.7 ± 0.4) %	(30.1 ± 0.4) %
18.50	(35.3 ± 0.5) %	(38.4 ± 0.5) %

Table 8.5: Total efficiency for air showers simulated with Sibyll. The shown error is the statistical uncertainty.

The tables 8.6, 8.7 and 8.8 give the values for the mean effective area per energy bin for the Epos, QGSJET-II and Sibyll calculations.

8.2.4 Calculation of the space angle dependence

To finish the calculation of the aperture $\mathcal{A}(E)$, we have to integrate the effective area over the whole detection solid angle. We get

$$\mathcal{A}(E) = \int_{\Omega} \int_{S_{\text{gen}}} e(E)\ \mathrm{d}S \cos\theta\ \mathrm{d}\Omega = \int_{\Omega} \overline{\mathrm{S_{eff}}}(\mathrm{E})\ \mathrm{d}\Omega \tag{8.7}$$

with the differential solid angle $\mathrm{d}\Omega = \sin\theta\ \mathrm{d}\theta\ \mathrm{d}\phi$ and the total solid angle Ω. The effective area $S_{\text{eff}}(E,\theta)$ was replaced with the mean effective area $\overline{S_{\text{eff}}}(E)$ (averaged over solid angle). This removes also the $\cos\theta$ term from the first part of the equation. The azimuth angle ϕ has a range from 0 to 2π and the zenith angle θ has a range from 0 to the maximum accepted zenith angle θ_{max}. We get

$$\mathcal{A}(E) = \pi(1 - \cos^2\theta_{\text{max}})\overline{S_{\text{eff}}}(E) \tag{8.8}$$

Mean effective area $S_{\text{eff}}[\text{km}^2]$, Epos simulation		
Energy in $\log_{10}(E/\text{eV})$	Proton primaries	Iron primaries
16.50	0.021 ± 0.003	0.023 ± 0.003
16.75	0.366 ± 0.02	0.399 ± 0.02
17.00	2.978 ± 0.12	3.282 ± 0.12
17.25	14.91 ± 0.38	16.28 ± 0.40
17.50	46.12 ± 0.96	51.58 ± 1.02
17.75	104.4 ± 2.1	113.3 ± 2.2
18.00	316.7 ± 4.6	350.4 ± 4.8
18.25	624.7 ± 7.6	669.7 ± 7.8
18.50	851.4 ± 9.9	921.4 ± 10.3

Table 8.6: Energy dependent mean effective area (averaged over solid angle) for air showers simulated with Epos. The shown error is the statistical uncertainty.

Mean effective area $S_{\text{eff}}[\text{km}^2]$, QGSJET-II simulation		
Energy in $\log_{10}(E/\text{eV})$	Proton primaries	Iron primaries
16.50	0.020 ± 0.003	0.021 ± 0.003
16.75	0.324 ± 0.02	0.343 ± 0.02
17.00	2.721 ± 0.11	2.861 ± 0.12
17.25	13.02 ± 0.36	14.04 ± 0.37
17.50	39.50 ± 0.90	44.23 ± 0.94
17.75	92.83 ± 1.97	99.01 ± 2.03
18.00	281.9 ± 4.3	306.6 ± 4.5
18.25	500.9 ± 6.8	623.4 ± 7.6
18.50	757.8 ± 9.4	832.2 ± 9.8

Table 8.7: Energy dependent mean effective area (averaged over solid angle) for air showers simulated with QGSJET-II. The shown error is the statistical uncertainty.

Mean effective area $S_{\text{eff}}[\text{km}^2]$, Sibyll simulation		
Energy in $\log_{10}(E/\text{eV})$	Proton primaries	Iron primaries
16.50	0.017 ± 0.003	0.019 ± 0.003
16.75	0.292 ± 0.02	0.318 ± 0.02
17.00	2.352 ± 0.11	2.558 ± 0.11
17.25	11.52 ± 0.34	12.63 ± 0.35
17.50	35.16 ± 0.84	38.91 ± 0.88
17.75	83.77 ± 1.87	92.71 ± 1.97
18.00	242.0 ± 4.0	279.3 ± 4.3
18.25	440.3 ± 6.4	495.4 ± 6.7
18.50	694.4 ± 9.0	756.0 ± 9.4

Table 8.8: Energy dependent mean effective area (averaged over solid angle) for air showers simulated with Sibyll. The shown error is the statistical uncertainty.

Aperture $\mathcal{A}(E)$[km^2 sr], Epos simulation		
Energy in $\log_{10}(E/\text{eV})$	Proton primaries	Iron primaries
16.50	0.050 ± 0.007	0.055 ± 0.007
16.75	0.863 ± 0.050	0.940 ± 0.052
17.00	7.02 ± 0.28	7.73 ± 0.29
17.25	35.13 ± 0.90	38.35 ± 0.94
17.50	108.7 ± 2.4	121.5 ± 2.4
17.75	246.1 ± 4.9	267.0 ± 5.1
18.00	746.1 ± 10.8	825.5 ± 11.4
18.25	1472 ± 18	1578 ± 19
18.50	2006 ± 23	2171 ± 24

Table 8.9: Energy dependent aperture for air showers simulated with Epos. The shown error is the statistical uncertainty.

Aperture $\mathcal{A}(E)$[km^2 sr], QGSJET-II simulation		
Energy in $\log_{10}(E/\text{eV})$	Proton primaries	Iron primaries
16.50	0.046 ± 0.006	0.049 ± 0.006
16.75	0.763 ± 0.047	0.809 ± 0.048
17.00	6.41 ± 0.27	6.74 ± 0.27
17.25	30.67 ± 0.84	33.07 ± 0.88
17.50	93.06 ± 2.10	104.22 ± 2.22
17.75	218.7 ± 4.6	233.3 ± 4.8
18.00	664.3 ± 10.2	722.4 ± 10.7
18.25	1180 ± 16	1469 ± 18
18.50	1786 ± 22	1961 ± 23

Table 8.10: Energy dependent aperture for air showers simulated with QGSJET-II. The shown error is the statistical uncertainty.

For $\theta_{\text{max}} = 60°$ one gets

$$\pi(1 - \cos^2\theta_{\text{max}}) = \frac{3}{4}\pi \,\text{sr} \tag{8.9}$$

and

$$\mathcal{A}(E) = \frac{3}{4}\pi \,\text{sr} \cdot \overline{S_{\text{eff}}}(E) \tag{8.10}$$

8.2.5 Results of the aperture calculation

Combining the space angle factor and the effective area leads to the aperture values for this specific detector configuration. The obtained values are found in the tables 8.9, 8.10 and 8.11 for the simulations with Epos, QGSJET-II and Sibyll.

Aperture $\mathcal{A}(E)$[km^2 sr], Sibyll simulation		
Energy in $\log_{10}(E/\text{eV})$	Proton primaries	Iron primaries
16.50	0.040 ± 0.006	0.044 ± 0.006
16.75	0.689 ± 0.044	0.749 ± 0.046
17.00	5.54 ± 0.25	6.03 ± 0.26
17.25	27.15 ± 0.79	29.76 ± 0.83
17.50	82.85 ± 1.98	91.68 ± 2.08
17.75	197.4 ± 4.4	218.4 ± 4.6
18.00	570.2 ± 9.5	658.0 ± 10.2
18.25	1038 ± 15	1167 ± 16
18.50	1636 ± 21	1781 ± 22

Table 8.11: Energy dependent aperture for air showers simulated with Sibyll. The shown error is the statistical uncertainty.

8.3 Uptime calculation

The uptime is the time that the detector is able to take data with a defined configuration. The uptime is a part of the exposure, that is not dependent on the energy but the same for all energies, models and primaries used in this analysis.

The status of every component of the detector is monitored and stored in a database with a time binning of 10 minutes. The most severe limits on the possible uptime come from astronomical constraints: Data taking operations are only possible when the sun is below the horizon and the illuminated moon is not in the field of view of a telescope. This gives the maximum possible uptime of the detector, shown with the black curve in figure 8.1. Data taking operations are also limited to periods of good weather (no rainfall or snowfall at the site of the detector) and times with a low cloud fraction (otherwise, the showers are not visible). Data taking operations are also stopped, when a light sensor at the telescopes or the telescopes themselves detect a light flux that could possibly damage the PMTs. In this case the shutter of the telescope is closed. Possible sources for this light can be agricultural fires in the pampa, far away lightning storms or artificial lights that shine into the telescopes. The calculation of the uptime includes the possible deadtimes introduced by DAQ vetoes and the atmospheric monitoring.

For this analysis, the uptime was further limited to times when all telescopes (all six telescopes of Coihueco and all three of HEAT) were actively taking data and all three HEAT telescopes where in the upward position. The resulting integral uptime as function of time is shown in figure 8.1. The red curve is the integrated uptime of the Coihueco and HEAT telescopes, the black curve gives the theoretical uptime, that could be achieved when only astronomical constraints are considered. The uptime for Coihueco and HEAT is the same, because only times when both eyes were taking data together are considered. The difference to the black maximum curve is caused by the effects listed in the last paragraph.

The structure of times with rising uptime and constant uptime shown in figure 8.1 is caused by the moon cycles; times around the full moon are times without data

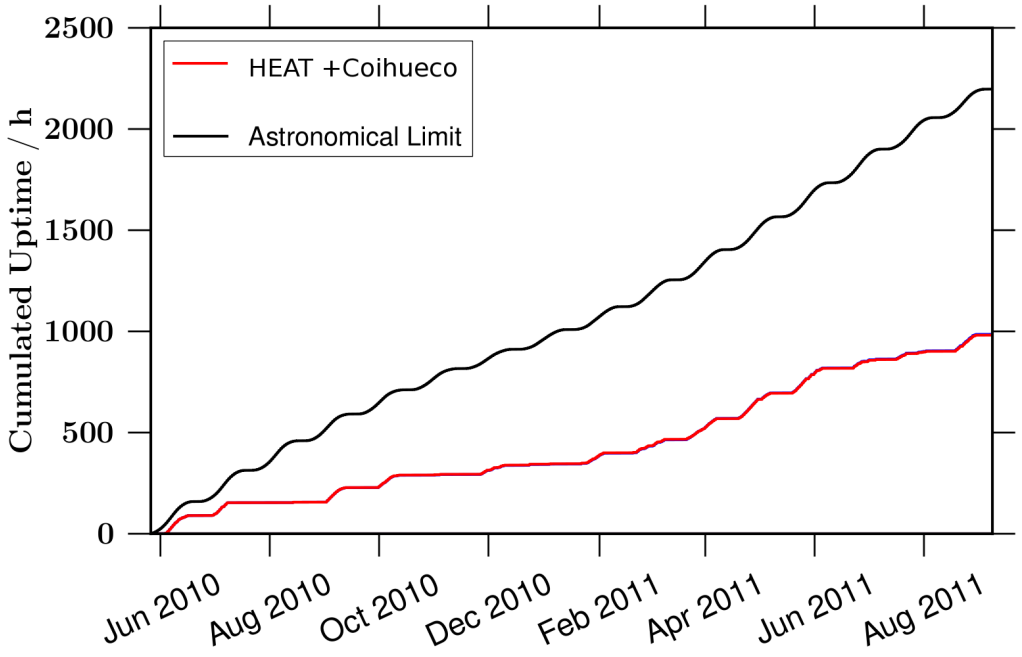

Figure 8.1: Shown is the integrated uptime together for Coihueco and HEAT in red in hours for the time period from June 2010 to September 2011. For HEAT and Coihueco curves lie on top of each other, because only time periods when HEAT and Coihueco were active together are counted. Shown in black is the maximum possible uptime, when only astronomical constraints are considered. The visible structure is generated by the moon cycles and other periods of downtime. See text for further details.

taking operations. Other sources of a constant uptime exist. A phase without data taking in the upward position around July 2010, for example, was caused by a failure in the tilting hydraulic system of HEAT: The very low temperatures led to ice formation in the hydraulic system, so that two telescopes could not be tilted. These telescopes were operated in downward mode. Other periods without increasing uptime values are planned downward operations of the HEAT telescopes for calibration or alignment studies.

The effect of the rate limiting, described in chapter 4.4.1.2, on the uptime of the HEAT telescopes can be seen in figure 8.2. It shows again the integrated uptime, but this time with the effect of he rate limiting included. The blue curve for HEAT is now always below the red curve for Coihueco, as is to be expected. The structure of the curve stays the same compared to the curve without rate limiting. Figure 8.3 shows the ratios of the different uptimes. One sees, that the rate limiting reduces the uptime of HEAT to around 75% of the Coihueco uptime. The relatively low value of the uptimes compared to the astronomically possible uptime (around 40% and 25% respectively) can be explained by the strict conditions set on the detector status. If even one telescope of the nine considered has to be removed from the DAQ,

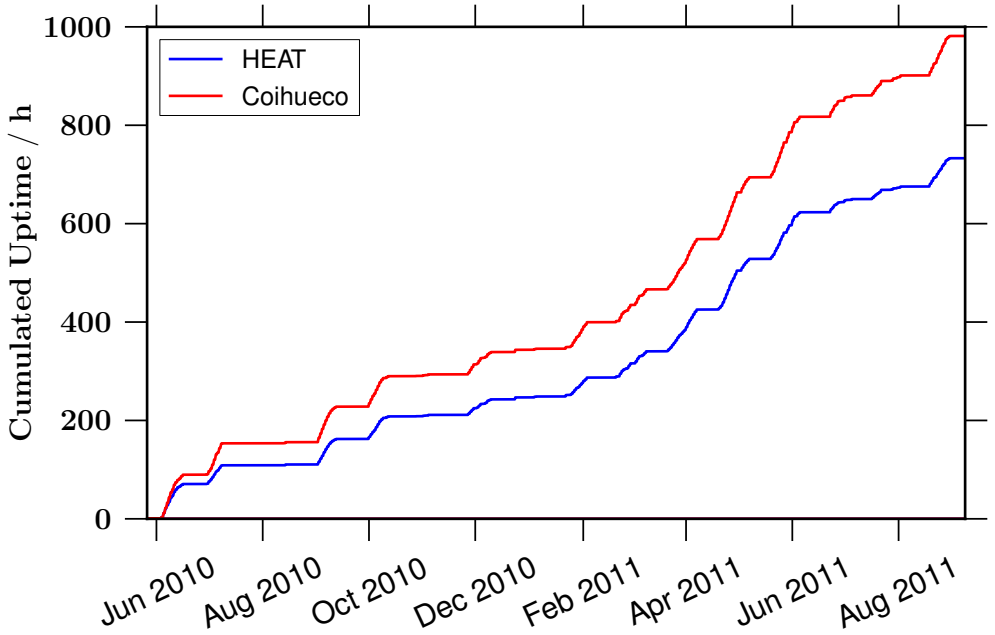

Figure 8.2: Shown is the integrated uptime for Coihueco in red and HEAT in blue in hours for the time period from June 2010 to September 2011. The effect of the T3 rate limiting is considered. The rate limiting only effects the uptime of HEAT and leads to a smaller uptime for HEAT compared to Coihueco.

these times are not considered for the uptime but still for the astronomical limit. The probability that one (or more) telescope has to be removed from the DAQ is relatively high, for example because of man made light pollution, problems with the hardware or high light levels from the moon. The total operation time of the FD detector (with a changing number of telescopes) is much closer to the astronomical limit and reaches values of up to 80%.

For the period from June 2010 (2010-05-31 23:09:58 UT[1]) to the end of the August 2011 FD shift (2011-09-13 12:49:58 UT) we get an integrated uptime for the eye Coihueco of 3530000 ± 50000 seconds and for the eye HEAT in upward mode under consideration of the T3 rate limiting we get an uptime of 2640000 ± 40000 seconds. The error on the uptime is given as the counting error of ten minute time bins, which is a very conservative approximation. As described in the explanation of the rate limiting (see chapter 4.4.1.2) and the merging process for data (see chapter 5.3), the rate limiting would lead to a non-static detector field of view: Normally, the COHE field of view would consist of the field of view of HEAT and Coihueco (the configuration used for the analysis). If HEAT is blocked by the rate limit the COHE field of view consists only of the Coihueco field of view. This would than lead to a bias towards Coihueco events. To correct for this, Coihueco events that were recorded when HEAT was rate limited were also removed from the data. Because of this method, the uptime that has to be used for the exposure calculation is that of

[1]Universal Time

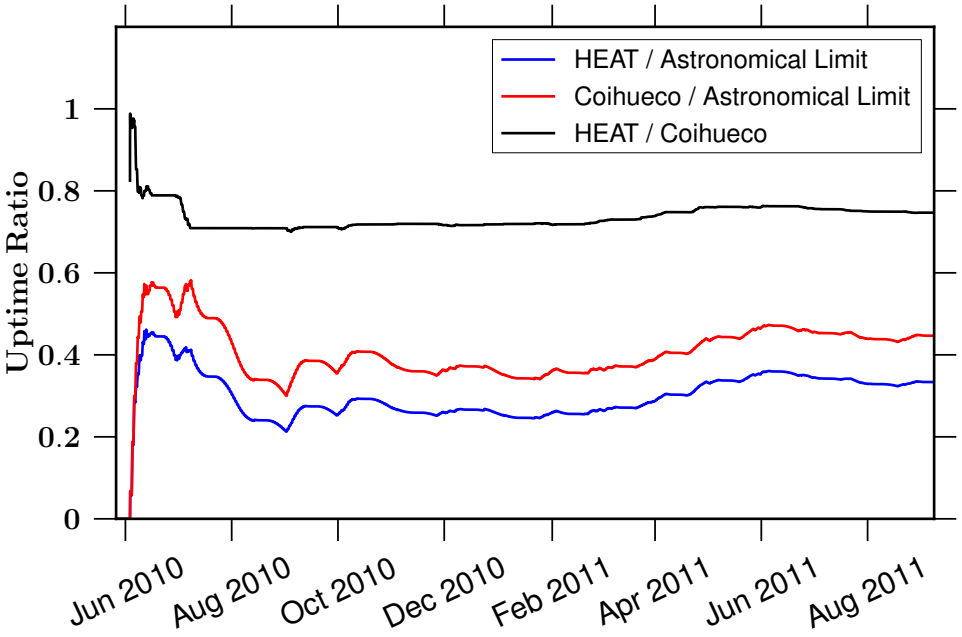

Figure 8.3: Shown are the ratios of the different uptimes. The blue curve shows the ratio of the integrated uptime of HEAT versus the astronomical limit, red shows the ratio of the Coihueco uptime versus the astronomical limit and the black curve shows the ratio of the HEAT versus the Coihueco uptime. The effect of the rate limiting is considered for HEAT.

the rate limited HEAT telescopes, because only events from times when HEAT was not rate limited were accepted in the data.

Following that, the uptime used for the exposure calculation is that of the rate limited HEAT telescopes: 2640000 ± 40000 seconds.

8.4 Calculation of the exposure

The exposure $\varepsilon(E)$ is now calculated by integrating the aperture over the uptime. The results in units of [km^2 sr yr] are shown in table 8.12, 8.13 and 8.14. A graph comparing the different exposure values is shown in figure 8.4.

The uncertainties on the exposure values were calculated by using the statistical uncertainties on the uptime and the number of successfully reconstructed simulated showers. All other parts of the exposure calculation are expected to have no statistical uncertainties.

The mean values for the exposure are calculated as arithmetic mean from the six calculated values for the combinations of composition and hadronic model. To calculate a (conservative) systematic error because of the unknown composition and the choice of the hadronic model, the maximum deviation from the mean to a single value and its statistical error is calculated and used as systematic error. The upper error is calculated as $\sigma_{syst,+}(E) = max_i((\varepsilon_i(E) + \sigma_i(E)) - \overline{\varepsilon}(E))$ and the lower error

Exposure $\varepsilon(E)$[km^2 sr yr], Epos simulation		
Energy in $\log_{10}(E/\text{eV})$	Proton primaries	Iron primaries
16.50	0.004 ± 0.001	0.005 ± 0.001
16.75	0.072 ± 0.004	0.079 ± 0.005
17.00	0.587 ± 0.025	0.647 ± 0.026
17.25	2.941 ± 0.088	3.210 ± 0.093
17.50	9.097 ± 0.235	10.17 ± 0.25
17.75	20.60 ± 0.52	22.35 ± 0.55
18.00	62.46 ± 1.31	69.11 ± 1.42
18.25	123.2 ± 2.4	132.1 ± 2.5
18.50	167.9 ± 3.2	181.8 ± 3.4

Table 8.12: Exposure values for air showers simulated with Epos. The error shown is the statistical uncertainty.

Exposure $\varepsilon(E)$[km^2 sr yr], QGSJET-II simulation		
Energy in $\log_{10}(E/\text{eV})$	Proton primaries	Iron primaries
16.50	0.004 ± 0.001	0.004 ± 0.001
16.75	0.064 ± 0.004	0.068 ± 0.004
17.00	0.537 ± 0.024	0.564 ± 0.024
17.25	2.567 ± 0.081	2.769 ± 0.084
17.50	7.790 ± 0.212	8.725 ± 0.228
17.75	18.31 ± 0.48	19.53 ± 0.50
18.00	55.61 ± 1.20	60.48 ± 1.28
18.25	98.80 ± 2.01	122.95 ± 2.39
18.50	149.5 ± 2.9	164.2 ± 3.2

Table 8.13: Exposure values for air showers simulated with QGSJET-II. The error shown is the statistical uncertainty.

Exposure $\varepsilon(E)$[km^2 sr yr], Sibyll simulation		
Energy in $\log_{10}(E/\text{eV})$	Proton primaries	Iron primaries
16.50	0.003 ± 0.001	0.004 ± 0.001
16.75	0.058 ± 0.004	0.063 ± 0.004
17.00	0.464 ± 0.022	0.504 ± 0.023
17.25	2.273 ± 0.075	2.492 ± 0.079
17.50	6.935 ± 0.196	7.676 ± 0.210
17.75	16.52 ± 0.45	18.29 ± 0.48
18.00	47.73 ± 1.07	55.08 ± 1.19
18.25	86.85 ± 1.82	97.72 ± 1.99
18.50	137.0 ± 2.7	149.1 ± 2.9

Table 8.14: Exposure values for air showers simulated with Sibyll. The error shown is the statistical uncertainty.

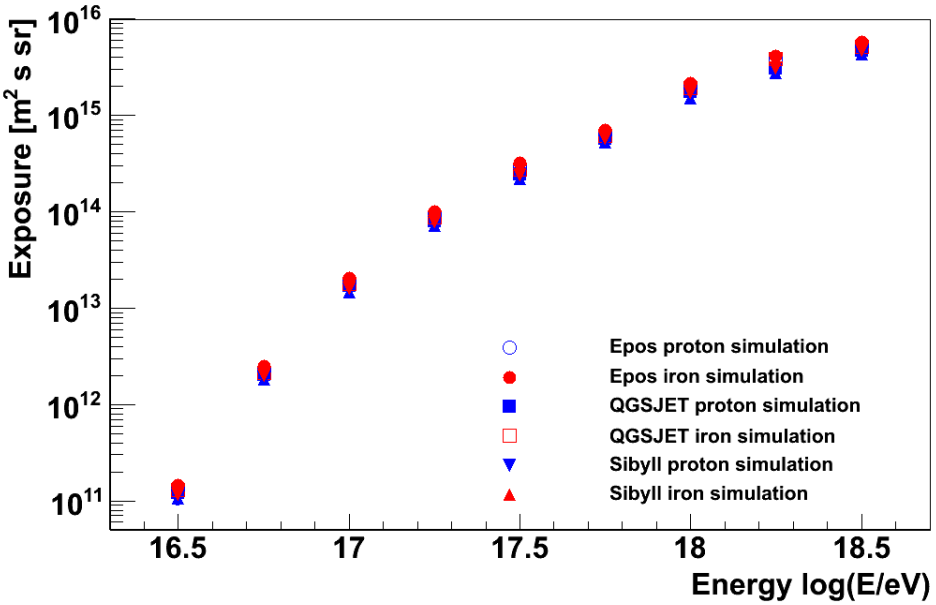

Figure 8.4: Energy dependence of exposure calculated for proton and iron primaries simulated with Epos, QGSJET-II and Sibyll.

Exposure $\varepsilon(E)$[km^2 sr yr]			
Energy in $\log_{10}(E/\text{eV})$	Mean value	Lower uncertainty boundary	Upper uncertainty boundary
16.50	0.004	0.001	0.001
16.75	0.067	0.013	0.016
17.00	0.551	0.109	0.123
17.25	2.709	0.511	0.594
17.50	8.399	1.660	2.027
17.75	19.27	3.19	3.63
18.00	58.41	11.75	12.11
18.25	110.3	25.2	24.3
18.50	158.2	24.0	27.0

Table 8.15: Mean exposure values from all primaries and models. Shown is the systematic uncertainty from the unknown composition and choice of hadronic model.

is calculated as $\sigma_{syst,-}(E) = min_i((\varepsilon_i(E) - \sigma_i(E)) - \overline{\varepsilon}(E))$, with i a specific combination of composition and hadronic model, $\varepsilon_i(E)$ one of the six exposure values and its uncertainty $\sigma_i(E)$. $\overline{\varepsilon}(E)$ is the mean exposure value of the energy bin. The resulting mean values and (asymmetric) systematic errors are shown in table 8.15 and figure 8.5.

8.5 Discussion

The calculated exposure for the specific detector configuration studied in this analysis gets rapidly larger for rising energies. This behavior is to be expected from

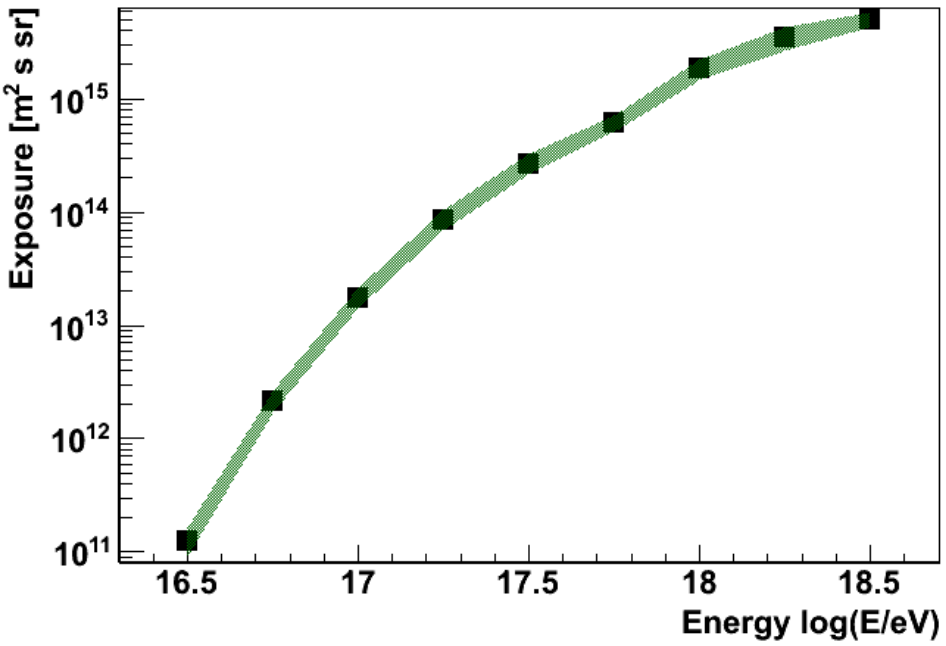

Figure 8.5: Mean value of the exposure, calculated from all combinations of hadronic models compositions shown in figure 8.4. The green band gives the maximum deviation of a single value and its error from the mean per bin and is used as a systematic uncertainty on the exposure from the choice of model and primary. This is a conservative calculation.

the small probability for low energy showers to trigger even a single SD station and the low amount of light low energy showers produce, which makes it very difficult to detect low energy showers. For air showers with higher energies, the amount of fluorescence light and the footprint of the shower and respectively the probability to trigger SD stations is larger in general, leading to a larger exposure for higher energy showers.

At an energy of $10^{17}\,\mathrm{eV}$, a mean exposure of

$$\varepsilon(10^{17}\,\mathrm{eV}) = 0.551^{+0.123}_{-0.109}\ [\mathrm{km}^2\ \mathrm{sr\ yr}]$$

was obtained. The given uncertainty is the systematic uncertainty from the choice of primary composition and hadronic model. All studied models and primary compositions show the same energy dependence and the differences between different models and compositions are small but existent.

With the exposure calculation complete, the calculation of the absolute flux of cosmic rays is possible. This is done in the next chapter.

9. Energy spectrum of cosmic rays detected with HEAT

This chapter gives the absolute energy spectrum of cosmic rays measured with the HEAT telescopes of the Pierre Auger Observatory. The used dataset consists of hybrid events taken over a span of 15 months. The spectrum is calculated for three hadronic interaction models and two primary compositions. An unfolding of the detector resolution on the mean spectrum is calculated. A fit of the spectral index of the cosmic ray flux is performed and a comparison to other measurements of the cosmic ray flux is presented.

The spectrum of cosmic rays is the flux of cosmic rays in dependence of the energy. The flux of cosmic rays is defined as:

$$j(E) = \frac{N(E)}{\Delta E} \frac{1}{\epsilon(E)} \tag{9.1}$$

with $N(E)$ the number of detected events in an energy bin E with a width ΔE and $\epsilon(E)$ the exposure for that energy bin. The exposure was calculated in the last chapter and the values are given in chapter 8.4.

9.1 Energy distribution in data

The distribution of the number of reconstructed events versus energy is shown in figure 9.1. The number of events per energy bin is given in table 9.1. The total number of events in the energy range from $10^{16.375}$ eV to $10^{18.625}$ eV is 20152.

9.2 Results

In the tables 9.2, 9.3 and 9.4 the values for the flux of cosmic rays measured with the HEAT extension together with the fluorescence detector of the Pierre Auger Observatory are shown. The values were calculated with three different hadronic interaction models and two compositions, a pure proton composition and a pure iron composition. The shown errors are the statistical uncertainties.

A comparison of the different measured flux values calculated for the different primaries and models is shown in figure 9.2. In figure 9.4 the ratio of the flux values per energy bin to the value calculated for protons with QGSJET-II as hadronic model is shown. The differences between the models and primaries are nearly independent

Reconstructed events per energy bin	
Energy in $\log_{10}(E/\mathrm{eV})$	Number of reconstructed events
16.50	204
16.75	1064
17.00	2847
17.25	4810
17.50	5046
17.75	3430
18.00	1737
18.25	733
18.50	281

Table 9.1: Number of reconstructed events from data per energy bin of size 0.25 in $log_{10}(E/\mathrm{eV})$.

Cosmic ray flux [eV^{-1} m^{-2} s^{-1} sr^{-1}], Epos simulation		
Energy $\log_{10}(E/\mathrm{eV})$	Proton primaries	Iron primaries
16.50	$(9.14 \pm 1.37) \times 10^{-26}$	$(8.42 \pm 1.22) \times 10^{-26}$
16.75	$(1.57 \pm 0.11) \times 10^{-26}$	$(1.44 \pm 0.09) \times 10^{-26}$
17.00	$(2.90 \pm 0.13) \times 10^{-27}$	$(2.63 \pm 0.12) \times 10^{-27}$
17.25	$(5.50 \pm 0.18) \times 10^{-28}$	$(5.04 \pm 0.16) \times 10^{-28}$
17.50	$(1.05 \pm 0.03) \times 10^{-28}$	$(9.37 \pm 0.27) \times 10^{-29}$
17.75	$(1.77 \pm 0.05) \times 10^{-29}$	$(1.63 \pm 0.05) \times 10^{-29}$
18.00	$(1.66 \pm 0.05) \times 10^{-30}$	$(1.50 \pm 0.05) \times 10^{-30}$
18.25	$(2.00 \pm 0.08) \times 10^{-31}$	$(1.87 \pm 0.08) \times 10^{-31}$
18.50	$(3.16 \pm 0.20) \times 10^{-32}$	$(2.92 \pm 0.18) \times 10^{-32}$

Table 9.2: Absolute flux of cosmic rays calculated with Epos simulations for proton and iron primaries. The shown errors are the statistical uncertainties of the values.

Cosmic ray flux [eV^{-1} m^{-2} s^{-1} sr^{-1}], QGSJET-II simulation		
Energy $\log_{10}(E/\mathrm{eV})$	Proton primaries	Iron primaries
16.50	$(1.00 \pm 0.16) \times 10^{-25}$	$(9.47 \pm 1.44) \times 10^{-26}$
16.75	$(1.77 \pm 0.12) \times 10^{-26}$	$(1.67 \pm 0.12) \times 10^{-26}$
17.00	$(3.17 \pm 0.15) \times 10^{-27}$	$(3.01 \pm 0.14) \times 10^{-27}$
17.25	$(6.30 \pm 0.22) \times 10^{-28}$	$(5.84 \pm 0.20) \times 10^{-28}$
17.50	$(1.22 \pm 0.04) \times 10^{-28}$	$(1.09 \pm 0.03) \times 10^{-28}$
17.75	$(1.99 \pm 0.06) \times 10^{-29}$	$(1.87 \pm 0.06) \times 10^{-29}$
18.00	$(1.87 \pm 0.06) \times 10^{-30}$	$(1.72 \pm 0.06) \times 10^{-30}$
18.25	$(2.49 \pm 0.11) \times 10^{-31}$	$(2.00 \pm 0.08) \times 10^{-31}$
18.50	$(3.55 \pm 0.22) \times 10^{-32}$	$(3.24 \pm 0.20) \times 10^{-32}$

Table 9.3: Absolute flux of cosmic rays calculated with QGSJET-II simulations for proton and iron primaries. The shown errors are the statistical uncertainties of the values.

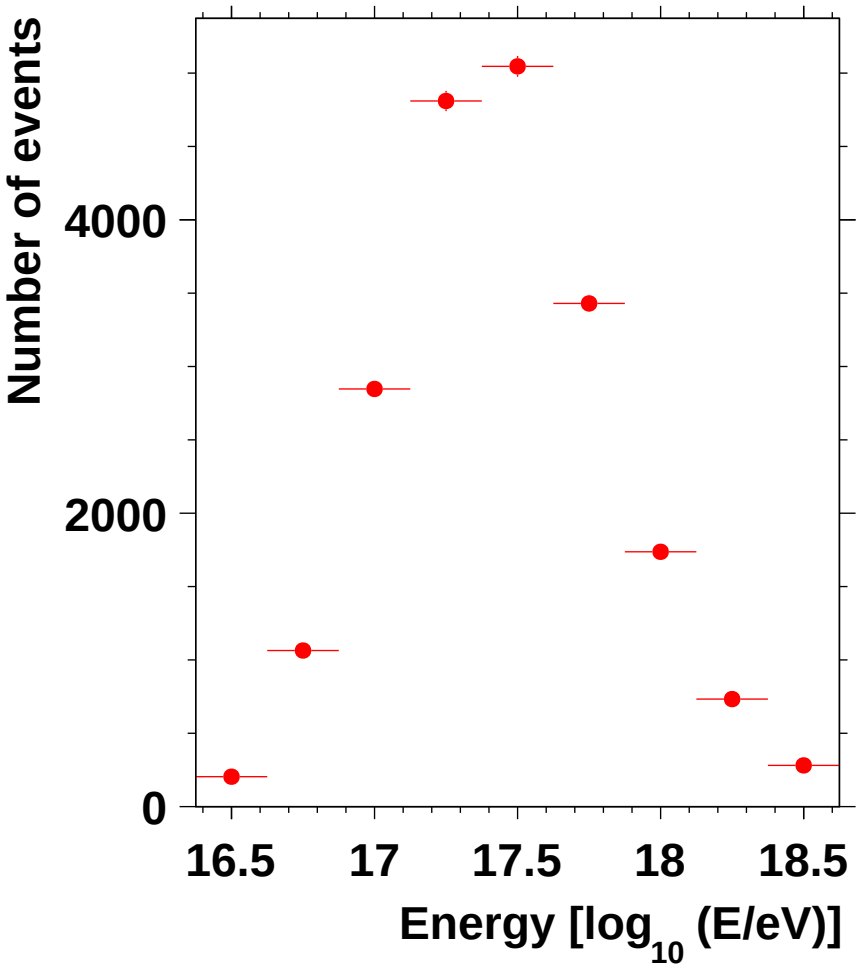

Figure 9.1: This figure shows the energy distribution of the data in the bins used for the spectrum analysis. The data selection process is explained in chapter 7. The horizontal error bars show the bin width, the vertical error bars show the Poisson error on the number of entries. These errors are very small and only visible for the two highest bins.

of the shower energy. The maximum deviation occurs for iron primaries simulated with Epos and proton primaries simulated with Sibyll and is of the order of 30%.

To classify the effect of the a priori unknown primary composition and the effect of the different hadronic interaction models, a mean spectrum is generated from the the spectra of the six combinations of primary particle and model. To quantify a systematic uncertainty stemming from the model or primary choice, a conservative systematic uncertainty is calculated, by using the maximum deviation from the mean to a single value and its statistical error as systematic error. The used method is the same as that used for the calculation of the systematic uncertainty of the exposure in chapter 8.4. A table of the mean flux values and the systematic uncertainty from composition and model is shown in table 9.5. A graphical representation is found in figure 9.3.

Cosmic ray flux [$\mathrm{eV}^{-1}\ \mathrm{m}^{-2}\ \mathrm{s}^{-1}\ \mathrm{sr}^{-1}$], Sibyll simulation		
Energy $\log_{10}(E/\mathrm{eV})$	Proton primaries	Iron primaries
16.50	$(1.15 \pm 0.19) \times 10^{-25}$	$(1.04 \pm 0.16) \times 10^{-26}$
16.75	$(1.96 \pm 0.14) \times 10^{-26}$	$(1.80 \pm 0.13) \times 10^{-27}$
17.00	$(3.67 \pm 0.19) \times 10^{-27}$	$(3.37 \pm 0.17) \times 10^{-28}$
17.25	$(7.11 \pm 0.26) \times 10^{-28}$	$(6.49 \pm 0.23) \times 10^{-29}$
17.50	$(1.38 \pm 0.04) \times 10^{-28}$	$(1.24 \pm 0.04) \times 10^{-30}$
17.75	$(2.21 \pm 0.07) \times 10^{-29}$	$(1.99 \pm 0.06) \times 10^{-31}$
18.00	$(2.17 \pm 0.07) \times 10^{-30}$	$(1.88 \pm 0.06) \times 10^{-32}$
18.25	$(2.84 \pm 0.12) \times 10^{-31}$	$(2.52 \pm 0.10) \times 10^{-32}$
18.50	$(3.88 \pm 0.24) \times 10^{-32}$	$(3.56 \pm 0.22) \times 10^{-33}$

Table 9.4: Absolute flux of cosmic rays calculated with Sibyll simulations for proton and iron primaries. The shown errors are the statistical uncertainties of the values.

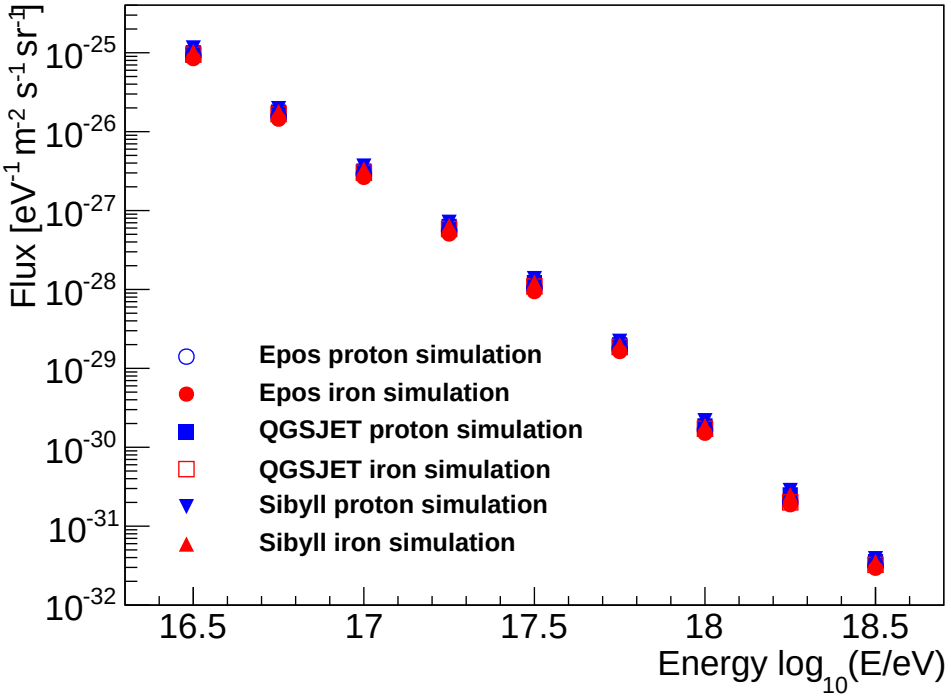

Figure 9.2: This figure shows the cosmic ray flux values for the different models and primaries measured with the HEAT extension and the fluorescence detector of the Pierre Auger Observatory. The statistical uncertainties are given as y-axis error bars but are are smaller than the markers for all bins.

E in $\log_{10} E/\mathrm{eV}$	Flux [$\mathrm{m}^{-2}\ \mathrm{sr}^{-1}\ \mathrm{s}^{-1}$]	Lower uncertainty boundary	Upper uncertainty boundary
16.50	9.83×10^{-26}	2.63×10^{-26}	3.59×10^{-26}
16.75	1.70×10^{-26}	0.36×10^{-26}	0.40×10^{-26}
17.00	3.13×10^{-27}	0.62×10^{-27}	0.73×10^{-27}
17.25	6.04×10^{-28}	1.17×10^{-28}	1.32×10^{-28}
17.50	1.15×10^{-28}	0.24×10^{-28}	0.27×10^{-28}
17.75	1.91×10^{-29}	0.33×10^{-29}	0.37×10^{-29}
18.00	1.80×10^{-30}	0.35×10^{-30}	0.45×10^{-30}
18.25	2.29×10^{-31}	0.50×10^{-31}	0.67×10^{-31}
18.50	3.39×10^{-32}	0.65×10^{-32}	0.74×10^{-32}

Table 9.5: Mean cosmic ray flux given in units of [$\mathrm{eV}^{-1}\mathrm{m}^{-2}\ \mathrm{sr}^{-1}\ \mathrm{s}^{-1}$] calculated from all model and primary combinations and systematic uncertainty with a lower and upper bound in the same units. The shown systematic uncertainty is a conservative calculation from the unknown real composition and choice of hadronic interaction model.

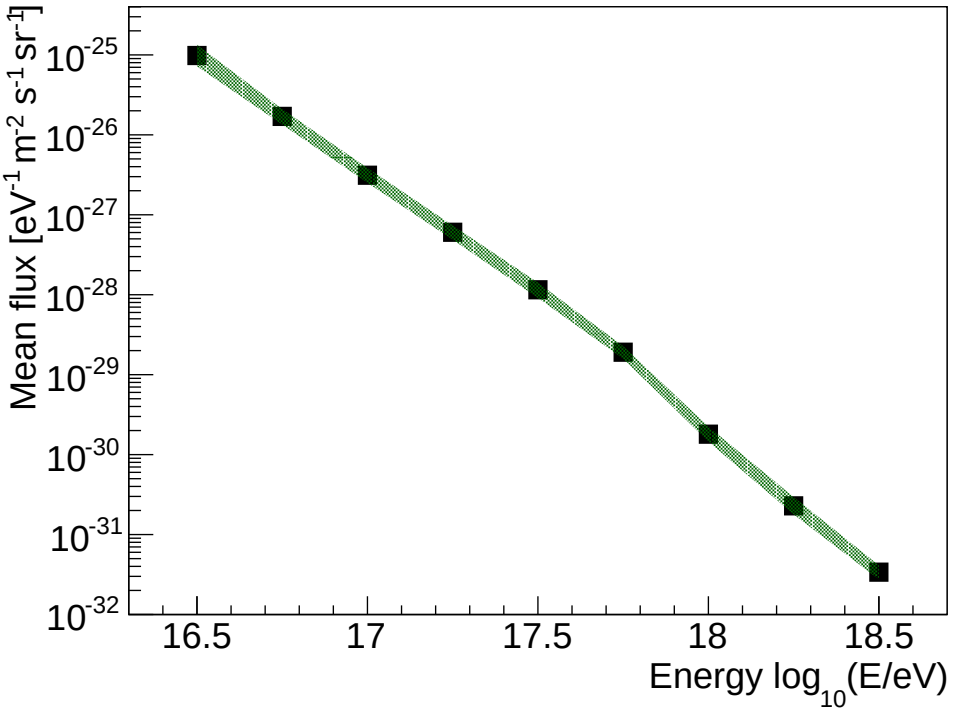

Figure 9.3: This figure shows the mean of the cosmic ray flux values for the different models and primaries measured with the HEAT extension and the fluorescence detector of the Pierre Auger Observatory. The error band gives the systematic uncertainty stemming from the model and primary choice.

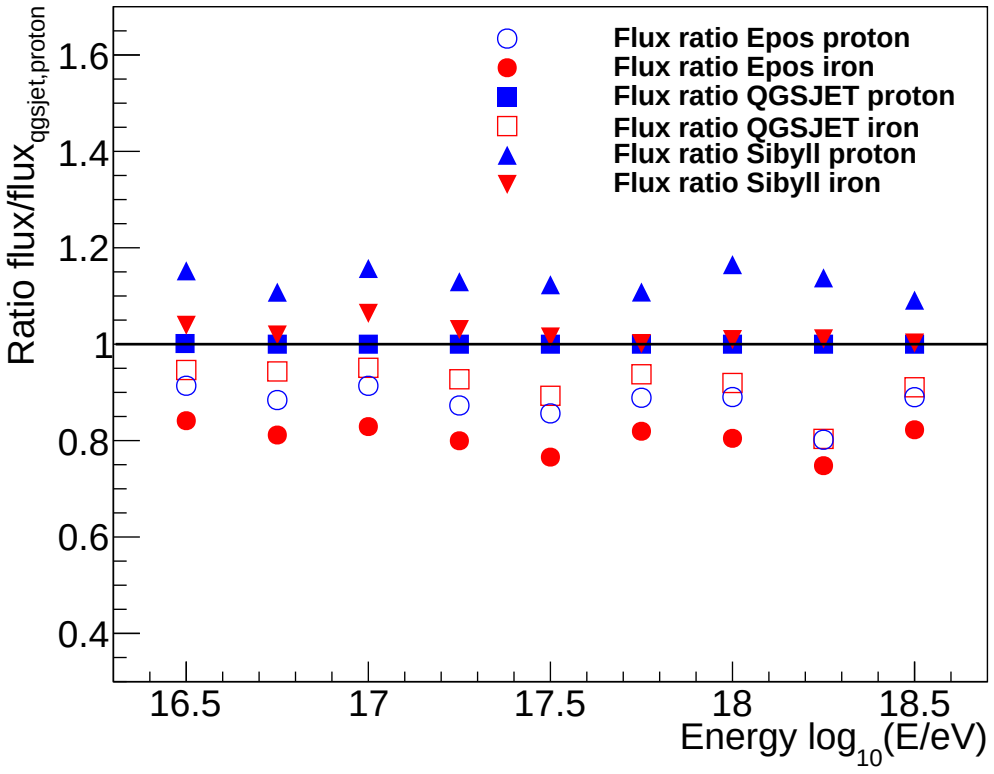

Figure 9.4: This figure shows the ratio of the flux values of the combinations of primary composition and interaction model compared to the flux value calculated with QGSJET and protons. To guide the eye, a line at a ratio of one, that is the QGSJET proton value, is drawn.

9.2.1 Spectral index fit

The fit of a power law to the data is possible. This is done by fitting a first order polynomial to the data in a double logarithmic representation to the mean spectrum calculated previously. The slope of the fitted function is the spectral index γ of the energy spectrum. A spectral index of

$$\gamma = -3.25 \pm 0.05$$

is found when including all nine data points in the fit. The $\chi^2/ndof$ for the fit is 14.3/7.

9.2.2 Unfolding of the detector resolution on the calculated spectrum

The calculated flux values presented here are of course convoluted with the finite resolution of the detector. This leads to the problem, that the "measured" values are not the "true" values, especially for a function that changes as rapidly as the cosmic ray flux, which could, for example, lead to an overflow of events from the lower energy bins to higher energy bins. A possible solution to this problem is the

E_{sim} in $\log_{10} E/\text{eV}$	E_{rec}	$\sigma(E_{\text{rec}})$
16.50	16.44	0.143
16.75	16.70	0.128
17.00	16.97	0.100
17.25	17.21	0.079
17.50	17.46	0.086
17.75	17.71	0.063
18.00	17.96	0.053
18.25	18.23	0.059
18.50	18.47	0.045

Table 9.6: Shown is the mean and σ of a Gaussian fit to the reconstructed energy distribution as a function of simulated energy.

unfolding of the measured values. Unfolding aims at reducing or removing the effect of the finite resolution.

To address this problem, the energy resolution is calculated by using the simulated air showers of the exposure calculation. The distribution of the reconstructed energies for every energy bin is plotted. For every energy bin, this distribution shows a Gaussian distribution in the center and additional non Gaussian tails. A fit of a Gaussian to the distributions is performed, and the resulting mean and σ is shown in table 9.6.

For the energy bin of $10^{18.5}\,\text{eV}$ the distribution of reconstructed shower energies and a Gaussian fit to the distribution is shown in figure 9.5.

The effect of a constant energy resolution of a Gaussian shape and a σ of 10 % on a power law spectrum (for example the cosmic ray spectrum) can be calculated[157]. Assume that events with the true energy E' are reconstructed with energy E with the probability

$$P(E, E') = N \exp\left(\frac{-(\mathrm{E} - \mathrm{E}')^2}{2\sigma^2}\right) \tag{9.2}$$

with a constant σ.

For the power law spectrum $\phi = AE^{-\gamma}$ the effect of the resolution can be given as the convolution of ϕ with the probability function.

$$\widetilde{\phi}(E) = \int_0^\infty \mathrm{dE'P(E, E')}\phi(\mathrm{E}') \tag{9.3}$$

For high energy values E this integral can be solved and expanded to

$$\widetilde{\phi}(E) = AE^{-\gamma}\left(1 + \gamma(\gamma - 1)\frac{\sigma^2}{2E^2} + \ldots\right) \tag{9.4}$$

The resulting effect for a spectrum with a spectral index of $\gamma = -3$ and a constant σ of 10 % is of the order of three percent [158].

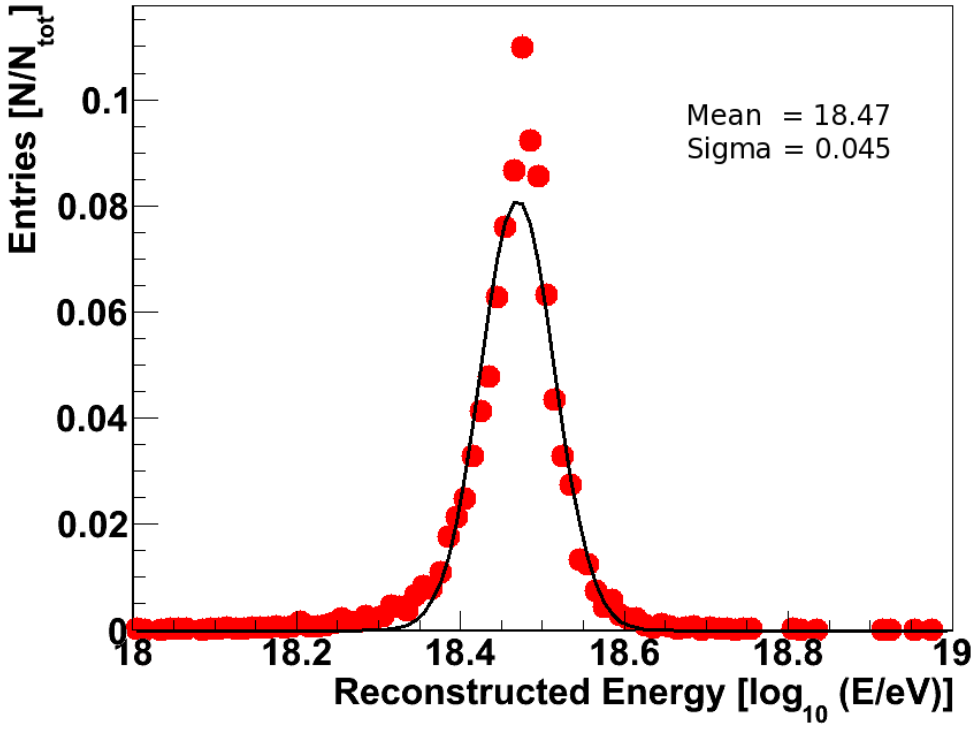

Figure 9.5: This figure shows the distribution of the reconstructed energy for the energy bin of $10^{18.5}$ eV. Notice the Gaussian peak in the middle and the non Gaussian tails.

For the case that the resolution is not of Gaussian shape and constant for all energies, as is the case for this analysis, a global multiplicative correction is not possible. Instead a bin-by-bin unfolding by calculating bin-by-bin correction factors C is used. For a description of the unfolding technique see the book "Statistical Data Analysis"[159].

The correction factors C are calculated as the fraction of the number of simulated events, that were successfully reconstructed and selected in the "right" energy bin to the total number of simulated events that were successfully reconstructed and selected. The resulting correction factors are of the order of 10 % and get smaller with energy, as is to be expected from the size of the energy bins and the energy resolution. The values for the resulting bin-by-bin unfolded mean spectrum can be found in table 9.8.

Figure 9.6 shows the resulting unfolded mean spectrum together with the systematic uncertainty from the choice of composition and hadronic model.

9.2.3 Spectral index fit on unfolded spectrum

A spectral index fit on the unfolded spectrum gives a value of

$$\gamma = -3.23 \pm 0.05$$

E_{sim} in $\log_{10} E/\text{eV}$	Correction factor C
16.50	1.174
16.75	1.150
17.00	1.147
17.25	1.337
17.50	1.114
17.75	1.102
18.00	1.092
18.25	1.086
18.50	1.077

Table 9.7: Shown are correction factors for the bin-by-bin unfolding of the detector resolution on the mean flux values.

E in $\log_{10} E/\text{eV}$	Flux [m^{-2} sr^{-1} s^{-1}]	Lower uncertainty boundary	Upper uncertainty boundary
16.50	1.15×10^{-25}	0.31×10^{-25}	0.42×10^{-25}
16.75	1.96×10^{-26}	0.41×10^{-26}	0.46×10^{-26}
17.00	3.59×10^{-27}	0.71×10^{-27}	0.84×10^{-27}
17.25	8.08×10^{-28}	1.56×10^{-28}	1.77×10^{-28}
17.50	1.28×10^{-28}	0.27×10^{-28}	0.30×10^{-28}
17.75	2.11×10^{-29}	0.36×10^{-29}	0.41×10^{-29}
18.00	1.97×10^{-30}	0.38×10^{-30}	0.49×10^{-30}
18.25	2.49×10^{-31}	0.54×10^{-31}	0.73×10^{-31}
18.50	3.65×10^{-32}	0.70×10^{-32}	0.80×10^{-32}

Table 9.8: Mean cosmic ray flux given in units of m^{-2} sr^{-1} s^{-1} after bin-by-bin unfolding of the detector resolution. The given errors are the systematic uncertainty because of primary and model choice.

with a $\chi^2/ndof$ of the fit of 14.2/7. Comparing that to spectral indices measured by other experiments gives a very good agreement, for example a single power law fit to data from the Kascade-Grande Collaboration for energies above 10^{17} eV gives a value of the slope of $\gamma = -3.24 \pm 0.08$ [160]. Looking at the energy weighted representation of the cosmic ray flux in figure 9.7 a possible change in the spectral index of the spectrum seems to occur at an energy of $10^{17.75}$ eV. A fit on only the last 5 data points gives a value of $\gamma = -3.57 \pm 0.12$ with a $\chi^2/ndof$ of 1.7/3. A fit to the first five data points gives a spectral index of $\gamma = -2.9 \pm 0.14$ with a $\chi^2/ndof$ of 0.86/3. This seems to be a hint that the spectral index is changing, but this has to be checked with a finer energy binning and higher statistics. It is also possible, that this effect stems from a change in the differences between the different primaries and models.

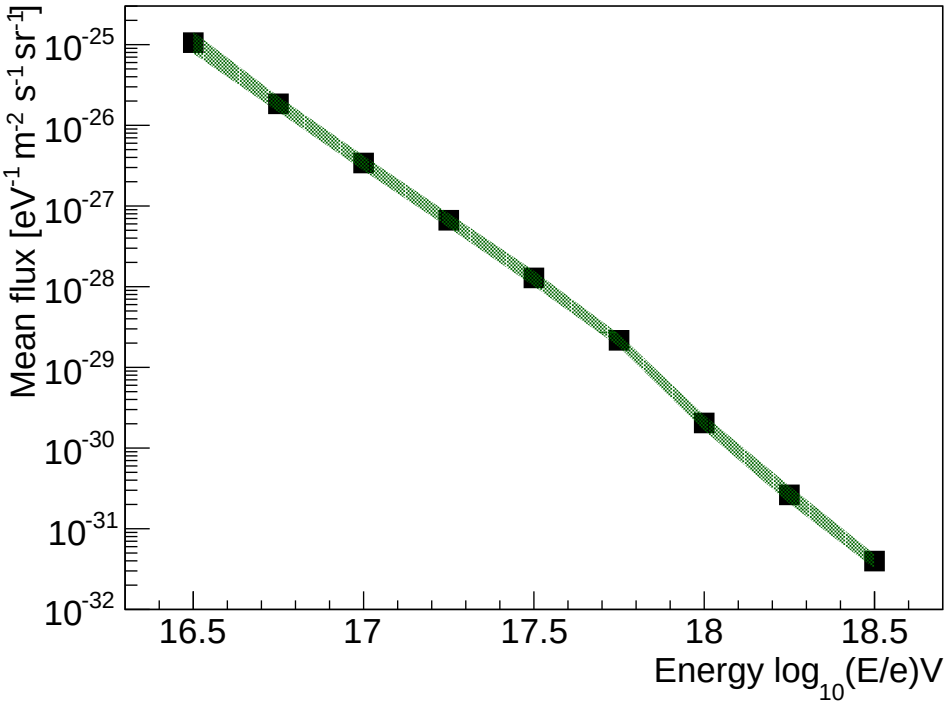

Figure 9.6: Mean cosmic ray flux after bin-by-bin unfolding of the detector resolution for cosmic rays detected with the HEAT extension and the fluorescence detector of the Pierre Auger Observatory. The shown errors are the systematic uncertainty because of primary and model choice.

9.3 Comparison to other published cosmic ray energy spectra

Figure 9.7 shows a comparison of the unfolded mean flux values and systematic uncertainties to published flux values from several experiments. A good agreement between the data of this study and the other experiments is shown. Note that the systematic uncertainty on the energy scale was not studied in this analysis (see chapter 4.2.2). A good assumption for the energy scale uncertainty of this analysis is the use of the energy scale uncertainty of the standard fluorescence detector of the Pierre Auger Observatory, which is in the order off 22 %. The use of this uncertainty is possible, because of the cross calibration for the HEAT telescopes used in this analysis (see chapter 5.4.2). The uncertainty of the energy scale is the largest single systematic uncertainty. Because of the steeply falling spectrum, the uncertainty of 22 % leads to an uncertainty on the flux measurement of 71 %, following from $\frac{dN}{N} = \gamma \cdot \frac{dE}{E} = 3.23 * 22\% = 71\%$. For the other shown experiments, the energy scale uncertainty is of the same order. The Pierre Auger Collaboration is expected to publish an updated energy scale with a smaller systematic uncertainty in 2013, which should reduce this value.

The single flux values and the mean flux value are in good agreement with flux values measured at other experiments.

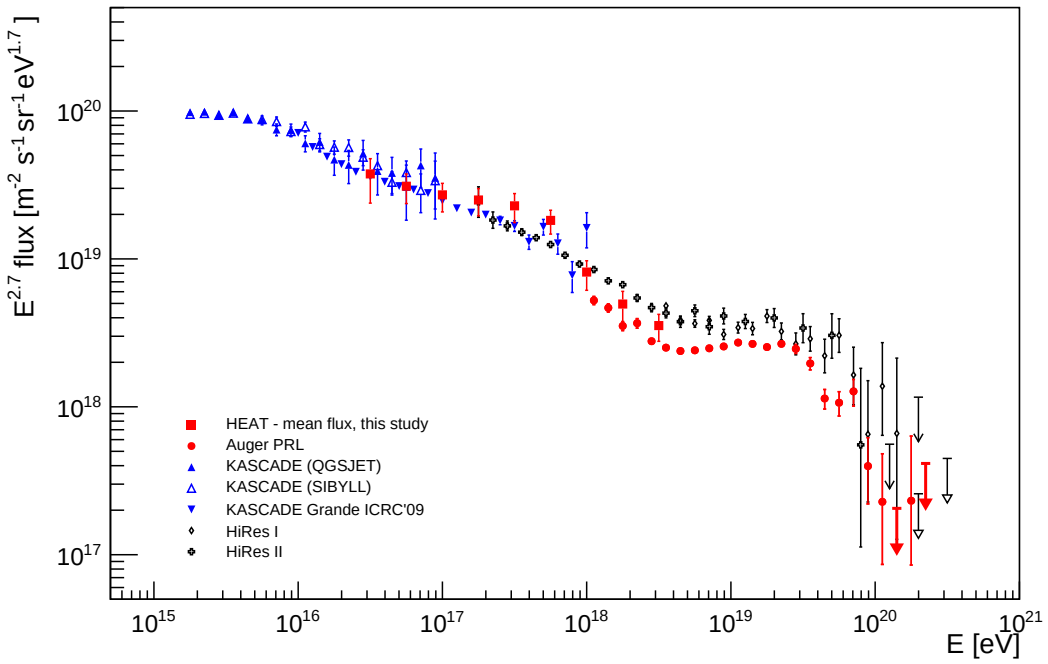

Figure 9.7: The figure shows the spectrum of cosmic rays weighted with the energy to the power of 2.7. The unfolded data points from this analysis shown are the mean of all flux values together with the systematic uncertainty from model and composition choice. For comparison with this analysis, data points from several experiments are included: Auger[161], Kascasde[25], Kascade-Grande[162] and Hires[31].

Of particular interest is the comparison of the energy spectrum of cosmic rays measured with HEAT, the low energy extension to the FD of the Pierre Auger Observatory to that measured with the infill, the low energy extension to the SD. First comparisons show a good agreement (see internal notes of the Pierre Auger Observatory on the infill spectrum), a complete analysis and comparison of the hybrid FD and SD spectrum will be published in a future analysis of the cosmic ray flux over the hole energy range of the Pierre Auger Observatory.

9.4 Discussion

The comparison of the flux values calculated in this analysis to other measurements of the absolute cosmic ray flux show a good agreement. A bin-by-bin unfolding of the detector resolution changes the flux values by 17 % for the lowest energy bin to 8 % for the highest energy bin. The differences between different choices of hadronic model and primary are small but existent and have a maximum value of 30%. The calculated spectral index of $\gamma = -3.23 \pm 0.05$ is in good agreement to those measured by other experiments.

10. Conclusions

10.1 Summary

This study presents a measurement of the absolute flux of cosmic rays as a function of the primary energy in a new energy range for the Pierre Auger Observatory. The measurement was done in the energy interval from $10^{16.5}$ eV to $10^{18.5}$ eV using hybrid data from the standard fluorescence telescopes and the HEAT telescopes, the new low energy extension of the fluorescence detector system of the Pierre Auger Observatory. A first result of this analysis is, that the HEAT extension of the Pierre Auger Observatory is working very well and is measuring air showers with a high quality and high statistics in its design energy range and even beyond that.

The measured flux is consistent with flux measurements from other experiments (independent of detection mechanism) and is in good agreement with published flux measurements of the Pierre Auger Observatory. A single power law fit to the flux data gives a spectral index of

$$\gamma = -3.23 \pm 0.05$$

which is in good agreement with other measurements, for example a single power law fit to data from the Kascade-Grande Collaboration for energies above 10^{17} eV gives a value of the slope of $\gamma = -3.24 \pm 0.08$ [160].

The effect of different hadronic interaction models and different primary particles on the spectrum calculation was studied and used to calculate a model- and primary dependent systematic uncertainty an the measured flux data. All studied models and compositions show the same slope of the spectrum and the maximum differences between different models and compositions is of the order of 30 %. A bin-by-bin unfolding of the detector resolution was performed on the mean flux, which changed the values between 17 % and 8 %.

This study consists of several parts: The first part is the reconstruction of 15 months of measured air showers from raw data for this new detector configuration. A large part of this study was the production of a library of simulated and reconstructed air showers. For that, a library of Conex air shower simulations with several hadronic interaction models was produced. These Conex showers were used as an input for the simulation of the detector response and afterwards a reconstruction similar to that used for real data. The reconstructed simulated air showers were then used to calculate the reconstruction efficiency, the effective area, the aperture and the

exposure for this new detector configuration using a static detector description. In addition, the calculation of the detector uptime from monitoring data with the inclusion of the effect of the rate limiting was also part of this study. The same simulated air showers were used to study the energy resolution of this detector configuration and calculate bin-by-bin correction factors for the flux values.

10.2 Outlook

Future improvements to the study of the cosmic ray flux in this new energy range for the Pierre Auger Observatory are the inclusion of information not available at the time of this analysis and the use of additional techniques that are possible with these information.

The greatest caveat to this analysis, the missing calibration for all photomultipliers of the HEAT telescopes, will be removed in 2013. The inclusion of the absolute calibration should not change the mean of the energy distribution of the measured showers, but could lead to changes in single events. With calibrated telescopes it will be possible to use information of the quality databases to exclude low quality showers from the analysis.

The use of shower simulations produced with the full air shower simulation software CORSIKA with high statistics instead of CONEX will reduce possible systematic uncertainties introduced by the simplifications used for the speed-up in CONEX. In addition a check on the trigger probability of the single SD stations for very low energy showers is needed when a future spectrum calculation includes effects of the inhomogeneous array in front of HEAT in a time dependent Monte Carlo simulation (so called RealMC). The inclusion of the HEATLET stations will increase the number of low energy showers and reduce statistical uncertainties for the lowest detectable energies.

The reduction of the uncertainties of the absolute fluorescence yield will lead to smaller systematic uncertainties on the energy measurement. The use of LHC data for a new generation of hadronic interaction models will lead to smaller systematic uncertainties when simulating air showers at these energies. The inclusion of the uptime calculation for the surface detector, that was neglected for this analysis, will be included in the next version of the spectrum analysis with HEAT data. A spectrum calculation, that uses a measured cosmic ray primary composition from data of the Pierre Auger Observatory instead of arbitrary compositions as input data will be able to reduce the systematic uncertainties even further.

In addition, HEAT and the Pierre Auger Observatory in total, are continuing to take data, reducing the statistical uncertainties of all measurements. Together with the standard detectors and other extensions of the Pierre Auger Observatory (already taking data or under construction) HEAT will lead to a complete measurement of the cosmic ray flux over the whole energy range of $10^{16.5}\,\mathrm{eV}$ to $10^{20}\,\mathrm{eV}$. Together with the measurement of the mass composition of comic rays in this energy range, the spectrum measurement will help answer some questions of the mystery of cosmic rays.

A. Appendix

A.1 List of abbreviations

ADC	Analogue to Digital Converter
ADST	Advanced Data Summary Tree
AERA	Auger Engineering Radio Array
AIRES	AIRshower Extended Simulations
AMIGA	Auger Muon-detectors and Infill for the Ground Array
CDAS	Central Data Acquisition System
CORSIKA	COsmic Ray SImulation for KAskade
FADC	Flash Analogue Digital Converter
FDAS	Fluorescence detector Data Acquisition System
FD	Fluorescence Detector
FLT	First Level Trigger
FLUKA	FLUktuierende KAskade
GDAS	Global Data Assimilation System
GPS	Global Positioning System
GZK-cutoff	Greisen-Zatsepin-Kuzmin-cutoff
HEAT	High Elevation Auger Telescopes
LDF	Lateral Distribution Function
LHC	Large Hadron Collider
MD	Muon Detector
NKG-function	Nishimura-Kamata-Greisen function
PMT	Photomultiplier Tube
QGSJET	Quark-Gluon-String model with Jets
SD	Surface Detector
SDP	Shower-Detector Plane
SLT	Second Level Trigger
T3	Hybrid Trigger
TLT	Third Level Trigger
UHECR	Ultra-High Energy Cosmic Ray
VEM	Vertical Equivalent Muon

A.2 List of conventions

Downward One of two tilting positions for the HEAT telescopes. In downward mode the field of view has an elevation range from 0° to 30°, similar to the standard FD telescopes.
Upward One of two tilting positions for the HEAT telescopes. In upward mode the field of view has an elevation range from 30° to 60°.
COHE Detector configuration that is the combination of Coihueco and HEAT. The data contains events that were seen by the two detectors coincidently and events that were seen only by Coihueco or only HEAT.
Electron The term electron refers, unless otherwise noted, to both electrons and positrons.
Standard FD Standard FD describes the entirety of the 24 FD telescopes without HEAT.
Standard telescope A standard telescope is part of the Standard FD.
Eye An eye stands for the six telescopes that are located in the same physical building (Los Leones, Los Morados, Loma Amarilla and Coihueco) or for the three HEAT telescopes.
Virtual Eye A virtual eye consists of telescopes of different physical eyes. A virtual eye exists only in the Offline software framework. The virtual eye COHE as combination of the six Coihueco telescopes and the three HEAT telescopes is used in this analysis.
Offline Offline is the analysis software framework of the Pierre Auger Observatory.
FD mono Reconstruction method where only information from one eye is used.
FD stereo Reconstruction method where information from two eyes that detected the same shower is used for the geometry reconstruction.
Hybrid Reconstruction method that uses information from one FD eye and timing information from one SD station for the geometry reconstruction. Showers that are reconstructed with this method are called (brass) hybrid showers.
Golden hybrid Class of showers that have a complete reconstruction in hybrid and SD mode. Used for the cross calibration of both detectors.

A.3 Offline Module sequences

A.3.1 Air shower simulation - Offline Module sequence

ModuleSequence.xml for the air shower simulation.

```
<sequenceFile>

<enableTiming/>
<moduleControl>

     <loop numTimes="unbounded" pushEventToStack="yes">

     <module> EventFileReaderOG            </module>
     <module> MCShowerCheckerOG            </module>
     <module> EventGeneratorOG             </module>

     <module> FdSimEventCheckerOG          </module>
     <module> ShowerLightSimulatorKG       </module>
     <module> LightAtDiaphragmSimulatorKG  </module>
     <module> ShowerPhotonGeneratorOG      </module>
     <module> TelescopeSimulatorKG         </module>
     <module> FdBackgroundSimulatorOG      </module>
     <module> FdElectronicsSimulatorOG     </module>
     <module> FdTriggerSimulatorOG         </module>

     <module> SdSimpleSimKG                </module>

     <module> CentralTriggerSimulatorXb    </module>
     <module> CentralTriggerEventBuilderOG </module>
     <module> EventBuilderOG               </module>

     <module> EventFileExporterOG          </module>

     </loop>

</moduleControl>

</sequenceFile>
```

A.3.2 Air shower reconstruction - Offline Module sequence

ModuleSequence.xml for the air shower reconstruction, used for real and simulated data.

```
<sequenceFile>

<enableTiming/>
<moduleControl>

<loop numTimes="unbounded" pushEventToStack="yes">

<module> EventFileReaderOG       </module>
<module> EventCheckerOG          </module>

<try>
<module> FdCalibratorOG          </module>
<module> FdEyeMergerKG           </module>
<module> FdPulseFinderOG         </module>
<module> FdSDPFinderOG           </module>
<module> FdAxisFinderOG          </module>
<module> HybridGeometryFinderOG  </module>
<module> HybridGeometryFinderWG  </module>
<module> FdApertureLightKG       </module>
<module> FdEnergyDepositFinderKG </module>
</try>

<module> RecDataWriterNG         </module>

</loop>

</moduleControl>

</sequenceFile>
```

A.4 Shower selection - Cut steering files

Cut steering file for event selection. Only FD cuts are used.

```
ADST cuts version: 1.0

hasEnergy               # bolean cut:succesfull energy reconstruction
isHybrid                # bolean cut:Event is a hybrid event
eyeCut           100000 # Only eye 6 (COHE) allowed
maxZenithFD         60. # maximum zenith angle
maxCoreTankDist    800. # maximum distance core-hybrid-tank in m
energyError         0.2 # max error on energy (relative)
maxDirCFrac         50. # max direct Cherenkov fraction in %
xMaxInFOV          20.0 # max distance of xMax to borders
profileChi2         2.5 # max reduced GH chi2
maxDepthHole        30. # maximum hole in profile in %
skipSaturated           # bolean cut:Events with saturated pixels removed
!badPixels            1 # bolean cut:Events with bad pixels removed
```

A.5 Energy bin borders

The lower and upper bounds for the used energy bins are given in the following. For the calculation, the value of the lower boundary E_{lb} is not included in the bin centered on E_{center}, but the value of the upper boundary E_{ub} is.

$$E(E_{\mathrm{center}}) = \{E | E_{\mathrm{lb}}(E) < E \leq E_{\mathrm{ub}}(E)\} \tag{A.1}$$

Energies in $\log_{10}$ E/eV		
Bin center $E(E_{\mathrm{center}})$	Lower border $E_{\mathrm{lb}}(E)$	Upper border $E_{\mathrm{ub}}(E)$
16.50	16.375	16.625
16.75	16.625	16.875
17.00	16.875	17.125
17.25	17.125	17.375
17.50	17.375	17.625
17.75	17.625	17.875
18.00	17.875	18.125
18.25	18.125	18.375
18.50	18.375	18.625

Table A.1: Lower and upper bounds for the used energy bins. The lower boundary is not included in the bin, the upper boundary is.

References

[1] V. F. Hess, *Beobachtungen der durchdringenden Strahlung bei sieben Freiballonfahrten*, Phys. Z., 13 (1912), p. 1084.

[2] C. D. Anderson, *The positive electron*, Phys. Rev., 43 (1933), pp. 491–494.

[3] C. D. Anderson and S. H. Neddermeyer, *Cloud chamber observations of cosmic rays at 4300 meters elevation and near sea-level*, Phys. Rev., 50 (1936), pp. 263–271.

[4] C. M. G. Lattes, H. Muirhead, G. P. S. Occhialini, and C. F. Powell, *Processes Involving Charged Mesons*, Nature, 159 (1947), pp. 694–697.

[5] P. Auger *et al.*, *Extensive Cosmic-Ray Showers*, Rev. Mod. Phys., 11 (1939), pp. 288–291.

[6] J. Linsley, *Evidence for a Primary Cosmic-Ray Particle with Energy* 10^{20} *eV*, Phys. Rev. Lett., 10 (1963), pp. 146–148.

[7] Lyndon Evans and Philip Bryant (editors), *LHC Machine*, J. Instrum., 3 (2008), p. S08001.

[8] R. M. Baltrusaitis *et al.*, *The Utah Fly's Eye detector*, Nucl. Instrum. Meth., A240 (1985), pp. 410–428.

[9] J. Hörandel, Astropart. Phys., 19 (2003), pp. 193–220.

[10] A. Hillas, J. Phys., G 31 (2005), pp. R95–R131.

[11] T. Wibig and A. Wolfendale, J. Phys. G: Nucl. Part. Phys., 31 (2005), p. 255.

[12] V. Berezinsky, S. Grigorieva, and B. Hnatyk, Astropart. Phys., 21 (2004), pp. 617–625.

[13] V. Berezinsky, A. Gazizov, and S. Grigorieva, Phys. Lett. B, 612 (2005), pp. 147–153.

[14] J. Blümer, R. Engel, and J. R. Hörandel, *Cosmic rays from the knee to the highest energies*, Progress in Particle and Nuclear Physics, 63 (2009), pp. 293–338.

[15] The Pierre Auger Collaboration, *Observation of the Suppression of the Flux of Cosmic Rays above* $4x10^{19}$ *eV*, Physical Review Letters, 101 (2008), p. 061101.

[16] The Pierre Auger Collaboration, *Measurement of the energy spectrum of cosmic rays above* 10^{18} *eV using the Pierre Auger Observatory*, Physics Letters B, 685 (2009), pp. 239–246.

[17] The Pierre Auger Collaboration, *Measurement of the depth of maximum of extensive air showers above* 10^{18} *ev*, Physical Review Letters, 104 (2010), p. 091101.

[18] The Pierre Auger Collaboration, *Correlation of the highest-energy cosmic rays with nearby extragalactic objects*, Science, 318 (2007), p. 938.

[19] The Pierre Auger Collaboration, *Correlation of the highest-energy cosmic rays with the positions of nearby active galactic nuclei*, Astroparticle Physics, 29 (2008), pp. 188–204.

[20] M. Nagano and A. A. Watson, *Observations and implications of the ultrahigh-energy cosmic rays*, Rev. Mod. Phys., 72 (2000), pp. 689–732.

[21] H. S. Ahn *et al.*, (ATIC-2 Collab.), Proc. of 28th Int. Cosmic Ray Conf., Tsukuba, (2003), p. 1853.

[22] N. L. Grigorov *et al.*, Yad. Fiz., 11 (1970), p. 1058.

[23] V. Derbina *et al.*, Astrophys. J., 628 (2005), p. L41.

[24] M. Amenomori *et al.*, (Tibet ASγ Collab.), Astrophys. J., 678 (2008), pp. 1165–1179.

[25] T. Antoni *et al.*, (KASKADE Collab.), Astropart. Phys., 24 (2005), pp. 1–25.

[26] J. C. Arteaga-Velazques *et al.*, (KASKADE-Grande Collab.), Proc. of 15th Int. Symposium on Very High-Energy Cosmic Ray Interactions, Paris, (2008).

[27] M. Nagano *et al.*, J. Phys., G10 (1984), p. 1295.

[28] M. Nagano *et al.*, J. Phys., G18 (1992), pp. 423–442.

[29] T. Abu-Zyayyad *et al.*, (HiRes-MIA Collab.), Astrphys. J., 557 (2001), pp. 686–699.

[30] T. Abu-Zyayyad *et al.*, (HiRes-MIA Collab.), Phys. Rev. Lett., 84 (2000), p. 4276.

[31] R. U. Abbasi *et al.*, (HiRes Collab.), Phys. Rev. Lett., 100 (2008), p. 101101.

[32] J. Abraham *et al.*, (The Pierre Auger Collab.), Phys. Rev. Lett., 101 (2008), p. 061101.

[33] K. Nakamura *et al.*, (Particle Data Group), J. Phys. G, 37 (2010), p. 075021.

[34] V. Berezinsky, M. Kachelriess, and A. Vilenkin, Phys. Rev. Lett., 79 (1997), pp. 4302–4305.

[35] J. R. Ellis, V. E. Mayes, and D. V. Nanopoulos, Phys. Rev., D74 (2006), p. 115003.

[36] C. T. Hill, Nucl. Phys., B224 (1983), p. 469.

[37] J. Abraham *et al.*, (Pierre Auger Collab.), *Limit on the diffuse flux of ultrahigh energy tau neutrinos with the surface detector of the Pierre Auger Observatory*, PHYSICAL REVIEW D, 79 (2009), p. 102001.

[38] J. Abraham *et al.*, (Pierre Auger Collab.), *Upper limit on the cosmic-ray photon fraction at EeV energies from the Pierre Auger Observatory*, Astoparticle Physics, 31 (2009), pp. 399–406.

[39] J. Abraham *et al.*, (Pierre Auger Collab.), *Search for ultrahigh energy neutrinos in highly inclined events at the Pierre Auger Observatory*, PHYSICAL REVIEW D, 84 (2010), p. 122005.

[40] E. Fermi, Phys. Rev., 75 (1949), p. 1169.

[41] W. Axford *et al.*, Proc. of 15th Int. Cosmic Ray Conf., Plovdiv, 11 (1977), p. 132.

[42] P. Lagage and C. Cersarsky, Astron. Astroph., 125 (1983), p. 249.

[43] E. Berezhko, Astropart. Phys., 5 (1996), p. 367.

[44] S. G. Lucek and A. R. Bell, Mon. Not. R. Astron. Soc., 314 (2000), pp. 65–74.

[45] A. M. Hillas, Ann. Rev. Astron. Astrophys., 22 (1984), pp. 425–444.

[46] R. J. Protheroe and A. P. Szabo, Phys. Rev. Lett., 69 (1992), pp. 2885–2888.

[47] E. G. Berezhko, Astroph, 684 (2008), pp. L69–L71.

[48] P. L. Biermann *et al.*, *Active galactic nuclei: Sources for ultra high energy cosmic rays?*, Nucl. Phys. B (Proc. Suppl.) and [astro-ph]0811.1848v3, 190 (2009), pp. 61–78.

[49] J. P. Rachen and P. L. Biermann, Astron. Astrophys., 272 (1993), pp. 161–175.

[50] M. J. Hardcastle, C. C. Cheung, I. J. Feain, and L. Stawarz, [astro-ph] 0808.1593, (2008).

[51] E. Waxman, Phys. Rev. Lett., 75 (1995), pp. 386–389.

[52] D. F. Torres and L. A. Anchordoqui, Rept. Prog. Phys., 67 (2004), pp. 1663–1730.

[53] N. Yanasak *et al.*, Astrophys. J., 563 (2001), p. 768.

[54] K. Greisen, Phys. Rev. Lett., 16 (1966), pp. 748–750.

[55] G. T. Zatsepin and V. A. Kuzmin, Pis'ma Zh. Eksp. Theor. Fiz., 4 (1966), p. 114.

[56] C. T. Hill and D. N. Schramm, Phys. Rev., D31 (1985), p. 564.

[57] F. W. Stecker and M. H. Salamon, Astrophys. J., 512 (1999), pp. 521–526.

[58] T. Stanev, Astrophys, 479 (1997), p. 290.

[59] P. P. Kronberg, Rep. Prog. Phys., 57 (1994), p. 325.

[60] T. K. Gaisser, *Cosmic rays and particle physics*, Cambridge Univ. Press, 1990.

[61] W. Heitler, *Quantum Theory of Radiation*, Oxford University Press Oxford, 1944 2nd edition.

[62] B. Rossi and K. Greisen, Rev. Mod.Phys., 13 (1941), p. 240.

[63] K. Kamata and J. Nishimura, Prog. Theo. Phys., 93 (1958), p. 6.

[64] T. K. Gaisser and A. M. Hillas, Proc. 15th Int. Cosmic Ray Conf. Plovdiv, Bulgaria, (1977), p. 358.

[65] K. Greisen, Ann.- Rev Nucl. Sci., 10 (1960), p. 63.

[66] J. Matthews, Astropart. Phys., 22 (2005), pp. 387–397.

[67] M. Risse, Acta Phys. Polon., B35 (2004), pp. 1787–1797.

[68] T. Pierog, R. Engel, and D. Heck, Czech. J. Phys., 56 (2006), pp. A161–A172.

[69] J. Hörandel, Mod. Phys. Lett. A, 22 (2007), p. 1533.

[70] C. Meurer *et al.*, Czech. J. Phys., 56 (2006), p. A211.

[71] J. Engel, T. K. Gaisser, P. Lipari, and T. Stanev, *Nucleus-nucleus collisions and interpretation of cosmic-ray cascades*, Phys. Rev. D, 46 (1992), pp. 5013–5025.

[72] D. Heck *et al.*, *A monte carlo code to simulate extensive air showers*, Wissenschaftliche Berichte FZKA, 6019 (1998), pp. 1–90.

[73] P. A. Cherenkov, *Visible emmission of clean liquids by action of γ radiation*, Doklady Akademii Nauk SSSR, 2 (1934), p. 451.

[74] J. Fowler *et al.*, (BLANCA Collab.), *A measurement of the cosmic ray spectrum and composition at the knee*, Astroparticle Physics, 15 (2001), pp. 49 – 64.

[75] F. Arqueros *et al.*, (HEGRA Collab.), *Energy spectrum and chemical composition of cosmic rays between 0.3 and 10 pev determined from the cherenkov-light and charged-particle distributions in air showers*, Astron. Astrophys., 359 (2000), pp. 682–694.

[76] J. Hinton, *The Status of the H.E.S.S. project*, New Astron.Rev., 48 (2004), pp. 331–337.

[77] D. Ferenc, *The magic gamma-ray observatory*, Nuclear Instruments and Methods in Physics Research Section A: Accelerators, Spectrometers, Detectors and Associated Equipment, 553 (2005), pp. 274 – 281.

[78] T. Weekes *et al.*, *Veritas: the very energetic radiation imaging telescope array system*, Astroparticle Physics, 17 (2002), pp. 221 – 243.

[79] F. Arciprette *et al.*, Nucl. Phys. Proc. Suppl., 150 (2006), pp. 186–189.

[80] M. Ave *et al.*, AIRFLY Collab., Nucl. Instr. and Meth. A, 597 (2008), p. 41.

[81] B. Keilhauer, J. Blümer, R. Engel, and H. O. Klages, Astropart. Phys., 25 (2006), pp. 259–268.

[82] F. Arqueros and J. Hörandel and B. Keilhauer (eds.), Nucl. Instr. and Meth. A, 597 (2008), pp. 1–120.

[83] M. Nagano, K. Kobayakawa, N. Sakaki, and K. Ando, Astropart. Phys., 20 (2003), pp. 293–309.

[84] M. Unger *et al.*, Nucl. Instr. and Meth. A, 588 (2008), pp. 433–441.

[85] M. Giller *et al.*, J. Phys., G31 (2005), pp. 947–958.

[86] F. Nerling, J. Blümer, R. Engel, and M. Risse, Astropart. Phys., 24 (2006), pp. 421–437.

[87] M. Giller and G. Wieczorek, Astropart. Phys., 31 (2009), pp. 212–219.

[88] D. Kuempel, K. H. Kampert, and M. Risse, Astropart. Phys., 30 (2008), pp. 167–174.

[89] R. U. Abbasi *et al.*, (HiRes Collab.), Astropart. Phys., 27 (2007), pp. 512–520.

[90] B. Fick *et al.*, (The Pierre Auger Collab.), 28th Int. Cosmic Ray Conf. Tsukuba, (2003), p. 449.

[91] C. Bonifazi *et al.*, (The Pierre Auger Collab.), *The angular resolution of the Pierre Auger Observatory*, Proc. of Cosmic Ray Int Seminar (CRIS 2008), astro-ph:0901.3138 and Nuclear Physics B Proceedings Supplements, 190 (2009), pp. 20–25.

[92] R. U. Abbasi *et al.*, (HiRes Collab.), Astropart. Phys., 25 (2006), pp. 74–83.

[93] S. Y. BenZvi *et al.*, Nucl. Instr. and Meth. A, 574 (2007), pp. 171–184.

[94] J. Abraham, (The Pierre Auger Collab.), Nucl. Instr. and Meth. A, 523 (2004), pp. 50–95.

[95] G. Askaryan, JETP, 48 (1965), p. 988.

[96] T. Huege and H. Falke, Astron. Astrophys., 412 (2003), pp. 19–34.

[97] A. F. Nelles, *Search for anomalies in cosmic air showers measured with the surface detector of the Pierre Auger Observatory*, master's thesis, RWTH Aachen University, 2010.

[98] J. Abraham *et al.*, (Pierre Auger Collab.), *Trigger and aperture of the surface detector array of the Pierre Auger Observatory*, Nucl. Instr. and Meth. A, 613 (2010), pp. 29–39.

[99] The Pierre Auger Collaboration, *The fluorescence detector of the Pierre Auger Observatory*, Nuclear Instruments and Methods in Physics Research Section A: Accelerators, Spectrometers, Detectors and Associated Equipment, 620 (2010), pp. 227–251.

[100] Schott, (http://www.schott.com).

[101] Photonis, (http://www.photonis.com).

[102] R. Knapik *et al.*, (Pierre Auger Collab.), *The absolute, relative and multi-wavelength calibration of the Pierre Auger Observatory fluorescence detectors*, Proceedings of the 30th International Cosmic Ray Conference, 4 (2007), pp. 343–346.

[103] C. Di Giulio *et al.*, (Pierre Auger Collab.), *Energy calibration of data recorded with the surface detectors of the Pierre Auger Observatory*, in Proceedings of the 31st International Cosmic Ray Conference (Lodz, Poland), 2009.

[104] B. R. Dawson *et al.*, *Hybrid Performance of the Pierre Auger Observatory*, in International Cosmic Ray Conference, vol. 4 of International Cosmic Ray Conference, 2008, pp. 425–428.

[105] A. Tripathi *et al.* Internal GAP Note, 2004. GAP-2004-39.

[106] M. Straub, *Mass composition studies with the low energy extension HEAT at the Pierre Auger Observatory*, master's thesis, RWTH Aachen University, 2012.

[107] GDAS, http://ready.arl.noaa.gov/gdas1.php.

[108] B. Keilhauer and M. Will, *Data from the global data assimilation system (gdas) for the Pierre Auger Observatory.* Internal GAP-Note, 2011. GAP-2011-015.

[109] M. Will and B. Keilhauer, *Monthly average profiles for corsika and off line based on data from the global data assimilation system (gdas).* Internal GAP-Note, 2011. GAP-2011-133.

[110] J. Abraham *et al.*, (Pierre Auger Collab.), *A Study of the Effect of Molecular and Aerosol Conditions in the Atmosphere on Air Fluorescence Measurements at the Pierre Auger Observatory*, Astropart.Phys., 33 (2010), pp. 108–129.

[111] C. Meurer and N. Scharf, The Pierre Auger Collaboration, *HEAT - a low energy enhancement of the Pierre Auger Observatory*, Astrophys. Space Sci. Trans., 7 (2011), pp. 183–186.

[112] The Pierre Auger Collab., (The Pierre Auger Collab.), *Enhancement of the PAO fluorescence detector by additional telescopes with elevated field of view*, (2006). Internal Proposal to the CB of the Pierre Auger Collaboration.

[113] J. Calvo de Nó, *Monitoring of camera positions for auger fluorescence telescopes.* Diploma Thesis, 2008.

[114] S. Falk *et al.*, *A First look at HEAT data.* Internal GAP note, 2010. GAP 2010-123.

[115] D. Kruppke-Hansen and J. Rautenberg, *Investigation of HEAT's high trigger rate.* Internal GAP Note, 2011. GAP-2011-121.

[116] T. Münzing, H. J. Mathes, M. Unger, and R. Engel, *T4 trigger tests for HEAT.* Internal Auger Collab. Meeting, March 2012.

[117] Disynet, (www.sensoren.info).

[118] S. Schulte, *Autocorrelation Studies of the Arrival Directions of UHECRs measured by the Surface Detector of the Pierre Auger Observatory*, PhD thesis, RWTH Aachen University, 2011.

[119] J. Calvo de Nó, N. Scharf, and S. Schulte, *The tilt monitoring for the HEAT telescopes of the Pierre Auger Observatory.* Internal GAP Note, To be published.

[120] J. Kelley, The Pierre Auger Collaboration, *Aera: the auger engineering radio array*, Proc. 32nd Int. Cosm. Ray Conf., (2011).

[121] B. Fuchs *et al.*, (The Pierre Auger Collab.), *The auger engineering radio array*, Nucl. Instr. and Meth. A, 692 (2012), pp. 93 – 97.

[122] B. Revenu, The Pierre Auger Collaboration, *Autonomous detection and analysis of radio emission from air showers at the Pierre Auger Observatory*, Proc. 32nd Int. Cosm. Ray Conf., (2011).

[123] P. S. Allison, The Pierre Auger Collab., *Microwave detection of cosmic ray showers at the Pierre Auger Observatory*, Proc. 32nd Int. Cosm. Ray Conf., (2011).

[124] H. P. Dembinski, *Measurement of the flux of ultra high energy cosmic rays using data from very inclined air showers at the Pierre Auger Observatory*, PhD thesis, RWTH Aachen University, 2010.

[125] P. Sommers *et al.*, (Pierre Auger Collab.), *First Estimate of the Primary Cosmic Ray Energy Spectrum above 3 EeV from the Pierre Auger Observatory*, in International Cosmic Ray Conference, vol. 7 of International Cosmic Ray Conference, 2005, p. 387.

[126] D. Kümpel, *Geometry reconstruction of fluorescence detectors revisited*, master's thesis, Bergische Universität Wuppertal, 2007.

[127] M. Mostafá *et al.*, (The Pierre Auger Collab.), *The hybrid activities of the Pierre Auger Observatory*, Nucl.Phys.Proc.Suppl., 165 (2007), pp. 50–58.

[128] S. Argiro *et al.*, *The offline framework of the Pierre Auger Observatory*, Nucl. Instr. and Meth., A580 (2007), pp. 1485–1496.

[129] R. Brun and F. Rademakers, *Root - an object oriented data analysis framework*, Nuclear Instruments and Methods in Physics Research Section A: Accelerators, Spectrometers, Detectors and Associated Equipment, 389 (1997), pp. 81–86.

[130] I. C. Mariş, F. Schüssler, R. Ulrich, and M. Unger, *Adst and event-browser reference manual - data summary trees and shower visualization for reconstructed auger events.* Internal GAP Note, 2006. GAP-2006-081.

[131] K. Daumiller, H. Klages, and S. Müller, *Relative Calibration of HEAT in tilted mode.* Internal GAP note, 2010. GAP 2010-43.

[132] S. Falk, R. Engel, R. Ullrich, and M. Unger, *Telescope alignment studies.* Internal GAP note, 2011. GAP-2011-123.

[133] T. Bergmann *et al.*, *One-dimensional hybrid approach to extensive air shower simulation*, Astropart. Phys., 26 (2007), pp. 420–432.

[134] D. Heck and J. Knapp, *Upgrade of the monte carlo code corsika to simulate extensive air showers with energies >= 10^{20} ev*, Wissenschaftliche Berichte FZKA, (1998).

[135] K. Werner, *The hadronic interaction modell epos*, Nuclear Physics B - Proceedings Suplements, 175-176 (2008), pp. 81–87.

[136] R. S. Fletcher, T. K. Gaisser, P. Lipari, and T. Stanev, *sibyll: An event generator for simulation of high energy cosmic ray cascades*, Phys. Rev. D, 50 (1994), pp. 5710–5731.

[137] S. Ostapchenko, *Nonlinear screening effects in high energy hadronic interactions*, Phys. Rev. D, 74 (2006), p. 014026.

[138] S. Ostapchenko, *On the re-summation of enhanced pomeron diagrams*, Physics Letters B, 636 (2006), pp. 40–45.

[139] Rechenzentrum der RWTH Aachen, *http://www.rz.rwth-aachen.de/aw/cms/rz/themen/ mem/hochleistungsrechnen/?lang=de*.

[140] P. Assis *et al.*, *Offline reference manual - fd simulation*. Internal GAP Note, 2008. GAP 2008-014.

[141] M. Prouza *et al.*, *Star tracking using background data of fd telescopes - whole star track optimization method*. Internal GAP note, 2005. GAP-2005-041.

[142] C. De Donato, *Using star tracks to determine the absolute pointing of the fluorescence detector telescopes*. Internal GAP note, 2005. GAP-2005-008.

[143] D. V. Camin, V. Grassi, F. Sánchez, and V. Scherini, (Pierre Auger Collab.), *Tracking stars with the fuorescence detector of the Pierre Auger Observatory*, Nuclear Instruments and Methods in Physics Research Section A, 518 (2003), pp. 177–179.

[144] R. Ulrich *et al.*, *Ultra-fast hybrid simulations with sdsimplesim*. Internal GAP Note, 2008. GAP 2008-061.

[145] L. Cazon, R. Vazquez, A. A. Watson, and E. Zas, astro-ph/0211223 and Astropart. Phys., 21 (2004), pp. 71–86.

[146] L. Cazon, R. A. Vazquez, and E. Zas, astro-ph/0412338 and Astropart. Phys., 23 (2005), pp. 393–409.

[147] K. Kamata and J. Nishimura, Prog. Theoret. Phys. Suppl., 6 (1958), p. 93.

[148] K. Greissen, *Progress in Cosmic Ray Physiscs Vol III*, Amsterdam:North-Holland, 1956.

[149] T. Antoni *et al.*, KASCADE Collaboration, astro-ph/0004233 and Astropart. Phys., 14 (2001), pp. 145–260.

[150] D. Barnhill *et al.*, The Pierre Auger Collab., astro-ph/0507590 and Proc. of 29^{th} Int. Cosmic Ray Conf.,Pune, India, (2005).

[151] I. C. Mariş *et al.*, *Adst-analysis manual - utilities for adst-analysis.* Internal GAP Note, 2009. GAP-2009-012.

[152] I. Bekman, *Measurement of Cherenkov light with the HEAT telescopes at the Pierre Auger Observatory*, master's thesis, RWTH Aachen University, 2012.

[153] P. Abreu *et al.*, (Pierre Auger Collab.), *The exposure of the hybrid detector of the Pierre Auger Observatory*, Astroparticle Physics, 34 (2011), pp. 368 – 381.

[154] The Pierre Auger Collaboration, *Constraints on the origin of cosmic rays above* 10^{18} *ev from large scale anisotropy searches in data of the Pierre Auger Observatory*, The Astrophysical Journal Letters, 762 (2013), p. L13.

[155] P. Morrison, *Solar origin of cosmic-ray time variations*, Phys. Rev., 101 (1956), pp. 1397–1404.

[156] F. Salamida and S. Petrera, *An end-to-end calculation of the auger hybrid exposure.* Internal GAP-Note, 2007. GAP-2007-002.

[157] C. O. Escobar, L. G. dos Santos, and R. A. Vazquez, *The effect of non gaussian errors on the determination of steeply falling spectra*, ArXiv e-prints astro-ph/0202172, (2002).

[158] F. Schüssler, *Measurement of the Energy Spectrum of Ultra-High Energy Cosmic Rays using Hybrid Data of the Pierre Auger Observatory*, PhD thesis, Universität Karlsruhe, 2008.

[159] G. Cowan, *Statistical Data Analysis*, Oxford University Press, 1998.

[160] W. D. Apel *et al.*, *Ankle-like feature in the energy spectrum of light elements of cosmic rays observed with kascade-grande*, Phys. Rev. D, 87 (2013), p. 081101.

[161] F. Schüssler *et al.*, (Pierre Auger Collab.), Proc. 31st Int. Cosm. Ray Conf., (2009).

[162] M. Bertaina *et al.*, (Kascade-Grande Collab.), Proc. 31st Int. Cosm. Ray Conf., (2009).

Acknowledgements - Danksagung

Für die Unterstützung während meiner Promotion danke ich meiner Familie und ganz besonders meinem Vater. Professor Hebbeker danke ich für die Betreuung meiner Promotion und die Möglichkeit ein interessantes Thema an einem großartigen Projekt zu bearbeiten und für die Möglichkeit das Observatorium mehrmals zu besuchen.
Für die gute Zusammenarbeit bei Aufbau und Inbetriebname des Tiltmonitorings danke ich Stephan Schulte. Für die Unterstützung bei dem Aufbau und der Inbetriebnahme des Tiltmonitorings bedanke ich mich bei der elektrischen und mechanischen Werkstatt des 3. Physikalischen Instituts der RWTH Aachen und ganz besonders bei Herrn Lampe und Herrn Szczesny. Hans Dembinski danke ich für manche Hilfe beim Einarbeiten in Offline und eine angenehme Zeit als Bürokollege. Für technische Hilfe mit Offline bedanke ich mich bei Daniel Kruppke-Hansen, Herman-Josef Matthes, Steffen Müller und Michael Unger. Für viele anregende Diskussionen und eine angenehme Atmosphäre im Büro bedanke ich mich bei Ilya Bekman, Maurice Stephan, Markus Lauscher, Marius Grigat und Stephan Schulte. Für technische Unterstützung, anregende Diskussionen und gute Zusammenarbeit danke ich Marcel Straub. Für das Lesen und Kritisieren einzelner Kapitel dieser Arbeit bedanke ich mich bei Maurice Stephan, Markus Lauscher, Ilya Bekman, Matthias Plum und Marcel Straub und außerdem bei Sebastian, Christian und Sabine. Für die Betreuung während eines Teils der Promotion bedanke ich mich bei Dr. Christine Meurer. Für eine immer angenehme Arbeitsatmosphäre bedanke ich mich bei der gesamten Auger-Gruppe am 3. Physikalischen Institut der RWTH Aachen.